

379
N81d
No. 4508

SULFUR-INDUCED CORROSION AT METAL AND OXIDE
SURFACES AND INTERFACES

DISSERTATION

Presented to the Graduate Council of the
University of North Texas in Partial
Fulfillment of the Requirements

For the Degree of

DOCTOR OF PHILOSOPHY

By

Hyacinth Cabibil, B.S.

Denton, Texas

August, 1997

Cabibil, Hyacinth, Sulfur-induced Corrosion at Metal and Oxide Surfaces and Interfaces, Doctor of Philosophy (Analytical Chemistry), August, 1997, 142 pages, 2 tables, 62 figures, reference list, 44 titles.

Sulfur adsorbed on metallic and oxide surfaces, whether originating from gaseous environments or segregating as an impurity to metallic interfaces, is linked to the deterioration of alloy performance. This research dealt with investigations on the interactions between sulfur and iron or iron alloy metallic and oxide surfaces under ultra-high vacuum conditions. Sulfur was either intentionally dosed from a H₂S source on an atomically clean metal surface, or segregated out as an impurity from the bulk to the metal surface by annealing at elevated temperatures.

It was found, based on temperature programmed desorption (TPD) and Auger electron spectroscopy (AES) measurements, that sulfur located at the iron-oxide interface reacts with the oxide to form SO₂ destroying interfacial bonds. This interfacial reaction suggests a microscopic mechanism for the instability of the oxide. X-ray photoelectron spectroscopy (XPS) measurements showed that on a Fe-Cr-Ni surface, the presence of interfacial sulfur retards the growth of an oxide but does not prevent the segregation of chromium at elevated temperatures. Moreover, while interfacial sulfur adversely affects the thermal stability of the iron oxide, the chromium oxide phase of the alloy remains stable. Ultra-high vacuum scanning tunneling microscopy (UHV-STM) and low energy electron diffraction (LEED) studies on Fe(111) revealed that the segregation of varying

coverages of sulfur causes faceting transformations and reactivity changes on the Fe(111) surface. The Fe(111) surface was found to exhibit an unusual triangular pitting upon the segregation of a high coverage of S. This high-S coverage surface is extremely inert towards oxidation near 300 K. In addition, the effects of N segregation on the reactivity of a Fe-Cr(100) surface was examined. It was found that co-segregation of Cr and N results in the formation of a CrN overlayer which retards oxidation of the surface at 300 K.

This research has potential implications to industrial processes such as electric power generation, petrochemistry and coal gasification, where alloy components are exposed to chemically aggressive environments at elevated temperatures.

379
N81d
No. 4508

SULFUR-INDUCED CORROSION AT METAL AND OXIDE
SURFACES AND INTERFACES

DISSERTATION

Presented to the Graduate Council of the
University of North Texas in Partial
Fulfillment of the Requirements

For the Degree of

DOCTOR OF PHILOSOPHY

By

Hyacinth Cabibil, B.S.

Denton, Texas

August, 1997

ACKNOWLEDGEMENT

This work was funded by the United States Department of Energy, Basic Energy Sciences, under Grant No. DE-FG03-93ER45497, and is gratefully acknowledged.

TABLE OF CONTENTS

	Page
LIST OF TABLES	vi
LIST OF FIGURES.....	vii
Chapter	
1. INTRODUCTION.....	1
Oxidation of a Metal: Oxide Formation	1
Sulfur and the Degradation of Alloys.....	6
Experimental Aspects.....	9
Chapter References	21
2. TPD AND AES STUDIES: SULFUR ON IRON METAL, OXIDE SURFACES AND INTERFACES.....	24
Introduction	24
Experimental.....	24
Results.....	27
Discussion.....	50
Summary and Conclusions.....	57
Chapter References	58
3. XPS STUDIES: EFFECTS OF SULFUR ON Fe AND Cr OXIDE THERMAL STABILITY IN 304 STAINLESS STEEL.....	61
Introduction.....	61
Experimental.....	61
Results.....	65
Discussion.....	77
Summary and Conclusions.....	78
Chapter References	78

4. UHV-STM, LEED AND AES STUDIES: SULFUR EFFECTS ON Fe(111)	80
Introduction	80
Introduction	116
Experimental Experimental.....	81
Results	84
Discussion.....	103
Summary and Conclusions.....	111
Chapter References	112
5. UHV-STM, LEED AND AES STUDIES: CrN OVERLAYER ON Fe _{0.8} Cr _{0.2} (100).....	116
.....	116
Results	118
Discussion.....	131
Summary and Conclusions.....	134
Chapter References	135
REFERENCE LIST.....	137

LIST OF TABLES

	page
Table 3.1. Analysis of the stainless steel (304) sample: bulk and surface composition.....	64
Table 3.2 A comparison of the binding energies (eV) obtained from the XPS experiments and published values in the literature.....	75

LIST OF FIGURES

	page
Figure 1.1. Schematic of oxide film/scale formation on a metal surface in an O ₂ environment	2
Figure 1.2. Illustration of S-induced degradation processes.....	7
Figure 1.3. Schematic of low-Miller index surfaces of a bcc crystal.....	10
Figure 1.4. Schematic of the photoemission process.....	12
Figure 1.5. Schematic of a concentric hemispherical analyzer (CHA).....	13
Figure 1.6. Full scan XPS spectrum of clean Fe showing XPS and Auger peaks.....	13
Figure 1.7. Schematic of the Auger process.....	14
Figure 1.8. Schematic of a cylindrical mirror analyzer (CMA).....	16
Figure 1.9. Schematic of a LEED experimental set-up.....	17
Figure 1.10 Schematic of a TPD process. Inset: a desorption spectrum.....	20
Figure 1.11. Schematic of a scanning tunneling microscope (STM).....	21
Figure 2.1. Schematic of the UHV system equipped with temperature programmed desorption (TPD) and Auger electron spectroscopy (AES) capabilities.....	25
Figure 2.2. Variations in the S _{(152)/Fe₍₆₅₁₎ Auger peak-to-peak intensity ratios as a function of H₂S exposure on a clean Fe(poly) surface: (a) adsorption at 80 K (b) adsorption at 80 K with subsequent annealing to 300 K or 500 K and adsorption at 316 K.}	28
Figure 2.3. (a) H ₂ and (b) H ₂ O desorption from a cleaned Fe(poly) surface exposed to 6L H ₂ S at 80 K. Curves are for successive TPD measurements without additional gas exposures. Each TPD measurement annealed the sample to 900 K.	30

Figure 2.4. (a) TPD spectra obtained from a clean Fe(poly) surface following adsorption of 6 L of H ₂ S at 85 K. H ₂ , H ₂ S and H ₂ O desorption are observed. (b) TPD spectra obtained from a clean Fe(poly) surface following adsorption of 7.5 L of H ₂ S at 316 K. No H ₂ , H ₂ S nor H ₂ O desorption are observed.....	31
Figure 2.5. S(LMM) Auger lineshape as a function of varying H ₂ S dosing conditions on clean Fe(poly) surface: (a) adsorption of 6 L of H ₂ S at 85 K (b) adsorption of 6 L of H ₂ S at 85 K with subsequent annealing to 500 K (c) adsorption of 6 L of H ₂ S at 316 K (no annealing). The spectra have been normalized to the same scale for clarity.	33
Figure 2.6. AES spectra of an Fe(poly) surface: (a) after exposure to 6 L H ₂ S at 80 K and annealing to 500 K; (b) after subsequent exposure to 1258 L O ₂ at 300 K and (c) after heating the oxidized sample to 900 K during TPD.....	36
Figure 2.7. Cracking pattern analysis of a surface exposed to 6 L of H ₂ S (80 K, 500 K anneal) followed by 1258 L of O ₂ at 300 K.....	36
Figure 2.8. Dependence of SO ₂ TPD yield on O ₂ exposure at 300 K. Each curve was taken from a cleaned Fe(poly) surface exposed to 6 L H ₂ S (80 K, 500 K anneal), and varying O ₂ exposure at 300 K.	38
Figure 2.9. (a) SO ₂ desorption peak area and S(LMM)/O(KLL) AES intensity ratios as a function of O ₂ exposure (L) following pre-exposure of Fe(poly) surface to H ₂ S at 80 K and subsequent annealing to 500 K.	39
Figure 2.10. TPD spectra of H ₂ O: (a) obtained from a S-free Fe oxide prepared by exposure of a clean Fe surface to 900 L of O ₂ at 300 K (b) obtained from a Fe-S-oxide surface prepared by exposure of a clean Fe surface to 6 L of H ₂ S at 316 K, followed by exposure to 900 L of O ₂ at 300 K. The H ₂ O desorption in both cases is attributed to a hydroxylated oxide surface.....	40
Figure 2.11. TPD and Auger data obtained from a Fe-S-oxide surface: (a) SO ₂ desorption after first anneal to 625 K (top trace) and repeated anneal to 720 K (bottom trace) (b) corresponding Auger spectra after first anneal (top trace) and second anneal (bottom trace). The sample was prepared by exposure of clean Fe to 6 L of H ₂ S (85 K, 500 K anneal), followed by exposure to 900 L of O ₂ at 300 K.	41
Figure 2.12. Variations in S(LMM)/O(KLL) Auger peak-to-peak intensity ratios as a function of H ₂ S exposure on a Fe oxide (900 L O ₂ , 300 K) surface: (a) adsorption at 85 K with and without subsequent annealing to 500 K (b) adsorption at 316 K with and without subsequent annealing to 500 K.....	43

Figure 2.13. (a) TPD profiles of SO ₂ obtained from a Fe oxide surface (900 L O ₂ , 300 K) following adsorption of H ₂ S at 316 K (no cooldown). SO ₂ desorption is observed only at high exposures. (b) Corresponding TPD spectra of the H ₂ O desorption.	44
Figure 2.14. Auger spectra of Fe oxide (900 L O ₂ , 300 K). Top trace: following adsorption of H ₂ S at 316 K (no cooldown). Middle trace: after first anneal of the surface to 720 K in UHV. Bottom trace: after second anneal to 720 K in UHV. Note the enhancement of the bifurcated S lineshape upon thermal cycling of the sample.	47
Figure 2.15. TPD spectra obtained from a Fe oxide surface (900 L O ₂ , 300 K) following adsorption of 1.2 L of H ₂ S (a) at 85 K and (b) at 316 K (no cooldown). SO ₂ desorption is observed only when H ₂ S and H ₂ O are coadsorbed on the oxide surface....	48
Figure 2.16. (a) TPD profiles of SO ₂ obtained from a Fe oxide surface exposed to 1.2 L of H ₂ S at 316 K with subsequent cooldown to 85 K. The spectra were taken at varying periods of waiting time at 85 K before TPD. The cooldown to 85 K allows the physisorption of H ₂ O from the chamber ambient. (b) TPD profiles of SO ₂ obtained from a Fe oxide surface exposed to 1.2 L of H ₂ S at 316 K (no cooldown). The measurements were carried out in UHV (top trace), in an overpressure of 10 ⁻⁸ Torr O ₂ (middle trace), and in an overpressure of 10 ⁻⁸ Torr H ₂ O (bottom trace).	50
Figure 2.17. Schematic representation of results obtained from the experiments.	51
Figure 3.1. Ultra-high vacuum (UHV) system for XPS studies.....	62
Figure 3.2. Variations in the relative Fe, Cr and Ni XPS intensities for a clean 304 stainless steel sample as a function of oxidation temperature. The sample was dosed successively with 60 L O ₂ exposure (10 ⁻⁷ torr, 600 s) from 325 - 825 K.....	66
Figure 3.3. Variations in the relative Fe, Cr and Ni XPS intensities for a clean 304 stainless steel sample as a function of oxidation temperature. The sample was dosed successively with 60 L O ₂ exposure (10 ⁻⁷ torr, 600 s) from 325 - 825 K.....	67
Figure 3.4. XPS spectra of S(2p) obtained following the adsorption of H ₂ S at 318 K on a clean 304 stainless steel sample. (a) low H ₂ S coverage (0.5 L) showing one S(2p) peak at 161.1 eV due to S ₂ , (b) high H ₂ S coverage (150 L) showing 2 peaks at 161.1 eV due to S ₂ and at 163.1 eV due to SH ₂ , (c) after subsequent anneal of (b) to 500 K....	69
Figure 3.5. XPS peak intensity ratio (S/Fe + Cr + Ni) as a function of H ₂ S exposures at 318 K. The data are not corrected for atomic sensitivity factors.	70

Figure 3.6. XPS spectra of Fe (2p), Cr (2p) and Ni (2p) for a sulfided (1 ML) 304 stainless steel surface before and after successive 60 L O ₂ exposures (10 ⁻⁷ Torr, 600 s) from 325 - 825 K. Only spectra taken from oxidation at 325 K, 625 K and 825 K are shown.	71
Figure 3.7. Variations in Fe, Cr and Ni XPS intensities for a sulfided (1 ML) 304 stainless steel as a function of oxidation temperature. The sample was successively dosed with 60 L O ₂ exposures (10 ⁻⁷ Torr, 600 s) from 325 - 825 K.	73
Figure 3.8. XPS spectra of Fe (2p), Cr (2p) and Ni (2p) for a sulfided (less than 1 ML) 304 stainless steel surface before and after successive 60 L O ₂ exposures (10 ⁻⁷ torr, 600 s) from 325 - 825 K. Only spectra taken from oxidation at 325 K, 625 K and 825 K are shown.	74
Figure 3.9. XPS spectra of Fe (2p _{3/2}) of an oxidized 304 stainless steel before and after momentary annealing to 900 K in UHV. (a) S-free sample (b) sample is predosed with less than a monolayer of S (c) sample is predosed with 1 monolayer of S. For simplicity, we did not attempt to deconvolute the Fe ²⁺ and Fe ³⁺ components of the oxide peak.	76
Figure 4.1. The ultra-high vacuum (UHV) system equipped with STM, LEED, AES and mass spectrometry capabilities.	82
Figure 4.2. (a) "Clock" LEED pattern obtained from a less-than-clean Fe(111) surface. Beam energy = 47 eV. (b) A typical Auger spectrum corresponding to the "clock" structure showing low coverages of S, N and O.	85
Figure 4.3. STM topographs of the "clock" surface. (a) An atomically resolved 10 nm x 10 nm area scan. Measurement parameters: sample bias = +0.01V, feedback set = 3.00 nA, scan speed = 100 nm/s. (b) A 400 nm x 400 nm area scan. Measurement parameters: sample bias = -0.100 V, feedback set = 1.00 nA, scan speed = 1495.33 nm/s.	87
Figure 4.4. (a) LEED pattern obtained from the Fe(111)-(1x1)-S. Beam energy = 47 eV. (b) A typical Auger spectrum of the (1x1)-S surface.	89
Figure 4.5. STM topographs of the Fe(111)-(1x1)-S surface. (a) 5 nm x 5 nm scan area. Measurement parameters: sample bias = +0.01 V, feedback set = 2.0 nA, scan speed = 50 nm/s. (b) A 300 nm x 300 nm scan area. Measurement parameters: sample bias = +0.10 V, feedback set = 1.00 nA, scan speed = 1500 nm/s.	90

Figure 4.6. A 50 nm x 50 nm STM topograph of the Fe(111)-(1x1)-S surface. Nanoscopic triangular pits are present which are 1 atom deep. STM measurement parameters: sample bias = +0.10 V, feedback set = 2.0 nA, scan speed = 500 nm/s.	92
Figure 4.7. (a) A 10 nm x 10 nm STM topograph showing the equilateral triangular pit. The edges of the pit are 11 atoms long. (b) A 3-dimensional representation of the pit in (a). STM measurement parameters: sample bias = +0.10 V, feedback set = 2.00 nA, scan speed = 100 nm/s.	93
Figure 4.8. (a) LEED pattern obtained from the Fe(111)-(2√3x1)R30°-S. Beam energy = 126 eV. (b) A typical Auger spectrum of the (2√3x1)R30°-S surface.	94
Figure 4.9. (a) A 400 nm x 400 nm STM topograph of the Fe(111)-(2√3x1)R30°-S surface. Measurement parameters: sample bias = +0.10 V, feedback set = 1.00 nA, scan speed = 1495.33 nm/s. (b) An edge-enhanced 50 nm x 50 nm STM topograph of the triangular pitting. A Roberts edge-enhancement procedure was used (see ref. (21)). Measurement parameters: sample bias = +0.05 V, feedback set = 1.00 nA, scan speed = 298.51 nm/s.	96
Figure 4.10. (a) A 25 nm x 25 nm STM topograph of the (2√3x1)R30°-S surface along with a line profile. The preferential formation of a 14 Å terrace width is observed. (b) A 10 nm x 10 nm scan area showing an atomically resolved image of "pits within a pit"	97
Figure 4.11. An atomically resolved (5 nm x 5 nm) surface buckling of the (2√3 x 1)R30° phase. Measurement parameters: sample bias = +0.01 V, feedback set = 5 nA, scan speed = 50 nm/s. Also shown is a schematic of the bcc(111) surface and the unit cells of the substrate (1 x 1) and the superstructure (2√3 x 1)R30°	99
Figure 4.12. Atomically resolved surface buckling obtained from flat areas near the triangular pits. Measurement parameters: sample bias = +0.01 V, feedback set = 5 nA, scan speed = 50 nm/s. This is a one of the packing arrangements of the atomically resolved images obtained between large pits of the (2√3x1)R30°-S surface.	101
Figure 4.13. Auger peak-to-peak O ₍₅₀₃₎ /Fe ₍₆₅₁₎ intensity ratios as a function of O ₂ on the Fe(111) surface with varying precoverages of S. The oxygen uptake curves are measured at room temperature. "clean" Fe and Fe with submonolayer S have an initial trace impurity of oxygen (8 % atomic conc.). The partial pressure of O ₂ used in obtaining these plots is 10 ⁻⁷ Torr.	102
Figure 4.14. (a) Top view of the bcc(111) surface showing the first, second and third atomic layers marked 1, 2 and 3 respectively; <i>on-top</i> and <i>subsurface</i> 3-fold hollow sites	

correspond to positions located on top of substrate atoms 2 and 3 respectively; a_0 is the side of the unit cell. (b) A bcc(111) surface with overlayer atoms located at *on-top* 3-fold hollows covering the second atomic layer of the substrate. (c) A bcc(111) surface with overlayer atoms located at both *on-top* and *subsurface* 3-fold hollows covering the second and third atomic layers of the substrate..... 105

Figure 4.15. A plot showing the relationship between annealing temperature and the surface phase observed. The horizontal axis is the S/Fe Auger peak-to-peak intensity ratio. The vertical axis represents the annealing temperature (K) at which the corresponding LEED pattern was observed..... 110

Figure 5.1. The Auger spectrum of the $\text{Fe}_{0.8}\text{Cr}_{0.2}(100)$ crystal after a 30-minute anneal at 833 K in UHV. The spectrum shows that the surface is enriched with cosegregated Cr and N..... 119

Figure 5.2. Variations in the $\text{Cr}_{(489)}/\text{Fe}_{(651)}$ and $\text{N}_{(379)}/\text{Fe}_{(651)}$ Auger peak-to-peak intensity ratios of the $\text{Fe}_{0.8}\text{Cr}_{0.2}(100)$ sample as a function of annealing time at 833 K in UHV. The data show that Cr and N saturation coverages are achieved very quickly. ... 120

Figure 5.3. STM topographic data (50 nm \times 50 nm) and line profile of the clean CrN surface. The CrN surface shows a step-terrace structure. 121

Figure 5.4. Variations in the low-energy Auger spectra of Fe and Cr for the CrN enriched- $\text{Fe}_{0.8}\text{Cr}_{0.2}(100)$ surface as a function of O_2 exposures at room temperature. The data indicate that at saturation oxygen coverage (15 L O_2), Cr is oxidized while Fe remains metallic..... 123

Figure 5.5. Changes in the Auger peak-to-peak intensity ratios of the CrN surface as a function of O_2 exposure: (a) $\text{N}_{(379)}/\text{Cr}_{(489)}$ and (b) $\text{N}_{(379)}/\text{O}_{(503)}$ 124

Figure 5.6. Variations in the topography across the CrN surface after exposure to 18 L of O_2 . Three types of topographical features are observed: (a) small terraces with 2-dimensional “islands” (b) large terraces with 2-dimensional “islands” (c) 3-dimensional islands..... 126

Figure 5.7. Changes in the characteristics of I - V curves as a function of O_2 exposure for the CrN surface. Also shown adjacent to the curves are the corresponding STM images which indicate the surface area where the I - V measurements were taken..... 127

Figure 5.8. Auger spectrum of the N-depleted $\text{Fe}_{0.8}\text{Cr}_{0.2}(100)$ surface. The sample was annealed at 833 K for 30 min. Relatively smaller amounts of N and Cr are segregated to the surface..... 129

Figure 5.9. Variations in the Auger spectra of the N-depleted $\text{Fe}_{0.8}\text{Cr}_{0.2}(100)$ surface as a function of O_2 exposure. The spectra show that both Fe and Cr are oxidized upon exposure to O_2 130

Figure 5.10. Changes in the absolute O(KLL) Auger peak-to-peak intensity as a function of O_2 exposure for CrN-enriched and N-depleted $\text{Fe}_{0.8}\text{Cr}_{0.2}(100)$ surfaces..... 134

CHAPTER 1

INTRODUCTION

This research dealt with investigations using surface sensitive techniques on the corrosion chemistry of S at metal, alloy and oxide surfaces under ultra-high vacuum (UHV) conditions. The goal of this work was to gain insights, at the fundamental level, on the deleterious effects of S on alloy performance. This research is particularly relevant to the applications of alloys for high-temperature service such as in electric power generation, petroleum refining and coal gasification. In these industrial environments, alloy components are exposed to chemically hostile conditions containing significant concentrations of S species. S is also a persistent impurity of steels which tends to segregate to metallic interfaces at elevated temperatures. The presence of S near or at the metal-oxide interface has been associated with the spallation of protective oxide scales (1-12) that can lead to massive corrosion. S located at the grain boundaries of metals and alloys is linked to the problem of grain embrittlement leading to the intergranular fracture of materials (13-15).

This chapter is devoted to a discussion of the following:

(i) basic concepts on oxide formation (ii) the detrimental effect of S on alloys (oxide spallation and grain boundary embrittlement) and (iii) the experimental aspects of this research.

Oxidation of a Metal: Oxide Formation

The initial stage of oxidation begins with the adsorption and subsequent dissociation of

the O_2 molecule on the metal surface. The dissociation of the O_2 molecule into atoms is accompanied by the gain of electrons by each O atom and the corresponding loss of electrons by the metal. The redox reaction is followed by nucleation and lateral growth of the oxide into a continuous film (16). Oxidation of a metal can also occur by reaction with either water vapor or carbon dioxide (16). Oxide formation on a metal in an O_2 atmosphere is schematically depicted in Fig. 1.1.

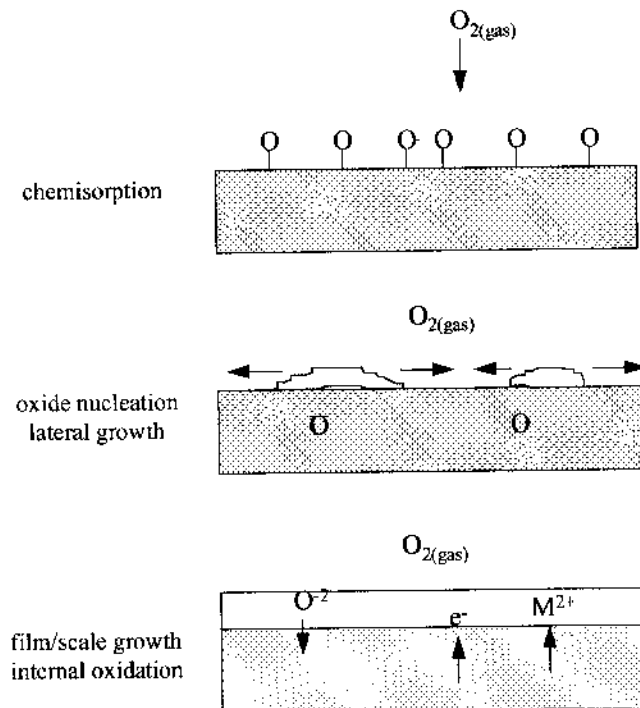


Figure 1.1. Schematic of oxide film/scale formation on a metal surface.

The oxide continues to grow until a certain thickness is attained which prevents further access of one reactant to another. The oxide film or scale serves as a “skin” and protects the metal from further reacting with oxidizing species. When the existing oxide is broken it exposes a bare metal surface to the environment. An oxide can rapidly reform on the

bare surface (17). In chemically aggressive atmospheres, corrosive agents can react with the exposed metal to form products that are porous and non-protective. Such reactions may lead to catastrophic corrosion.

The oxidation of a metal is characterized by a change in the free energy, ΔG , of the system which is equal to the work done or adsorbed during the process (16, 17). For the oxidation to proceed spontaneously, the change in the free energy of the system must be negative. The formation of almost all metal oxides involves a negative standard free energy change (ΔG°) (16, 17). In oxygen atmospheres, metal oxides are more thermodynamically stable than pure metals (16, 17). Thus, it is not a surprise that most metals are found in nature in their oxidized state.

The equilibrium constant, K , of a reaction is related to the free E change (17). For the oxidation described by the equation



K is equal to $[MO_{2(s)}]/[M_{(s)}][O_{2(g)}]$. By convention, the active masses of the solids are taken as unity. Under equilibrium conditions, the new equilibrium constant (K_p) is therefore equal to $1/p_{O_2}$ (partial pressure of O_2 in atmospheres). The relationship between the standard free E change and K_p is

$$\Delta G^\circ = -RT \ln K_p \text{ or } -RT \ln 1/p_{O_2} \quad (1.2)$$

where R is the gas constant and T is the absolute temperature (16, 17). From the last equation, one can calculate for the characteristic equilibrium pressure for the dissociation of an oxide given the temperature and ΔG° of formation for the pure oxide (MO_2) on the base metal, M .

Under non-equilibrium conditions, the following relationship applies (17):

$$\Delta G = \Delta G^\circ + RT \ln Q \quad (1.3)$$

where ΔG is the free energy at the specified temperature and Q is the ratio of the partial pressures of gaseous product(s) versus reactant(s).

A relationship also exists between the standard change in free energy, ΔG° , the standard heat or enthalpy of the reaction, ΔH° , the standard change in entropy, ΔS° , and absolute temperature (17). This is expressed by the following equation:

$$\Delta G^\circ = \Delta H^\circ - T\Delta S^\circ \quad (1.4)$$

The free energy change for oxidation reactions increases (become more positive) with increasing temperature (17). This is because the oxidation process is accompanied by a negative entropy change (from gaseous oxygen to solid oxide).

The oxidation of a metal is a result of an interplay of thermodynamic and kinetic factors. While oxide formation is a thermodynamically spontaneous process, the metal is usually not consumed completely to form the oxide. The oxidation decreases or stops at a certain point due to kinetic restraints, i.e., the reactants can no longer access each other.

Oxidation rates are determined by measuring the change in the oxide thickness, y , vs. time, t , often using weight gain measurements (17). There are several kinetic laws that can describe oxidation behavior. The three more commonly followed kinetic laws are parabolic, linear, and logarithmic (17). Logarithmic kinetics is described by the equation

$$dy/dt = k/t \quad (1.5)$$

where the oxidation rate is inversely proportional to time, t . This type of oxidation behavior is

usually obeyed for relatively thin films at low temperatures (16, 17) . High-temperature oxidation follows the parabolic law described by

$$y^2 = kt \quad (1.6)$$

where k is the parabolic rate constant (16, 17). The relationship indicates a rapid oxide growth (square of film thickness is proportional with time). A parabolic oxidation may transform to linear non-protective kinetics characterized by high oxidation rates (16). This occurs when the oxide being formed is so porous that oxidizing species can still diffuse and oxidize the underlying metal (16). A high oxidation rate may result in a breakaway oxidation such as the burning of Mg in air. It is obvious that a high oxidation rate cannot afford protection to the underlying metal. In order to form a protective oxide, a slow growth dominated by the transport of oxygen anions to the substrate is desirable (8, 18). Oxides grown this way are generally more dense and more adherent to the metal thus providing a barrier to the oxidizing environment.

Pure metals are of little practical importance because their corrosion resistance and metallurgical properties are usually not suitable for most technical applications. Certain alloys (solid mixtures of metals) have desirable mechanical as well as oxidation-resistant properties. The development of oxidation resistance in alloys is based upon the phenomenon of selective oxidation of one component of the alloy (8, 9, 16, 17). This alloy component is usually chromium, aluminum or silicon (8, 9). Each of these solutes have a greater affinity for oxygen than the solvent metal and will thus oxidize selectively to produce a protective surface oxide. Most Fe alloys designed for high-temperature oxidation resistance contain chromium (stainless

stainless steel (16, 17).

The mode of failure for alloy performance at high temperatures is typically via fracture and spallation of the protective oxide scales (8, 9, 19). This degradation mechanism is especially enhanced under thermal cycling conditions, i.e., when there is periodic heating and cooling of the equipment (9, 19). The inherent source of the stress is due to the different thermal expansion coefficients between the oxide and the metal (thermal stresses). In addition, there are growth stresses associated with the formation of the oxide. The volume of oxide formed is invariably different from the volume of the metal consumed (16). This difference is expressed by the Pilling-Bedworth ratio (PBR) which is given by the following ratio:

$$\text{PB ratio} = Wd/nDw \quad (1.7)$$

where W and D are the molecular weight and density of the oxide, d and w the atomic weight of the pure metal, and n is the number of metal atoms in the oxide molecule (16).

Sulfur and the Degradation of Alloys

It is well-known that the presence of S at or near the metal oxide interface enhances the spallation of oxide scales and the degradation of alloys. For high-temperature alloys (usually Fe or Ni based-alloys with Cr and Al contents), the incorporation of S to the oxide scale or near the alloy-oxide interface can originate from two sources (Fig. 1.2). One is a gaseous environment where a significant concentration of S-containing species are present. This gaseous condition can be found in the surroundings of power-generating plants, coal gasifier

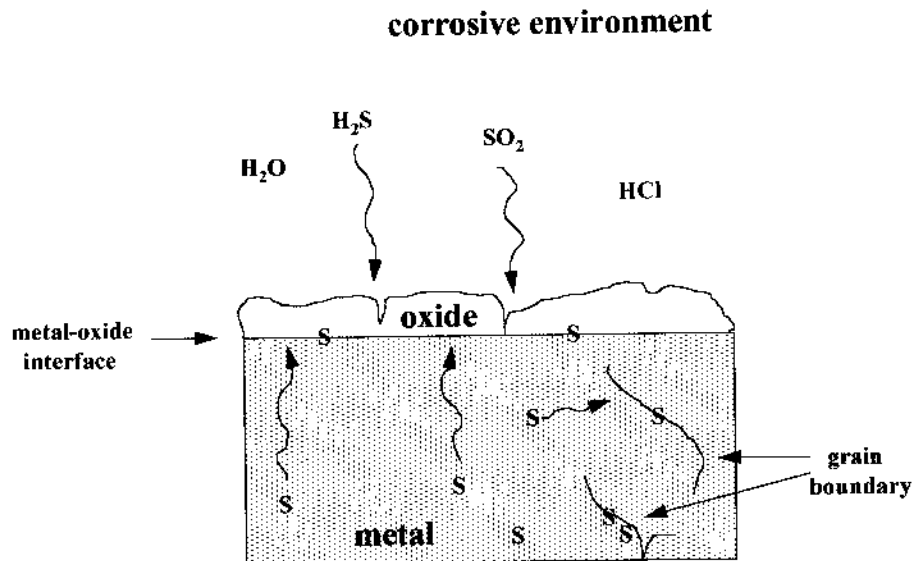


Figure 1.2. S-induced degradation processes.

and petrochemical refineries. The other source of S is the metal itself since S is a persistent impurity of most metal and alloys. At elevated temperatures, the S impurity can segregate to the grain boundaries and other internal interfaces of the oxide-metal system.

In the case where the environment contains S species, the deterioration of alloy performance is attributed to the formation of sulfides, in addition to oxides on the scale (1, 2). The formation of sulfides is initiated at sites of scale fracture (19). Sulfides are not protective because they are usually porous and highly defective and therefore transport of matter through the sulfide scale can be quite high (10). A sulfidation reaction may proceed at a linear rate in contrast to oxide formation which is approximately parabolic (1). Thus, more metal is consumed by sulfide formation. The formation of eutectics with low melting points is also possible (2). Such occurrence at high-temperature conditions can lead to rapid corrosion. Even if sulfide formation in the transient state is overgrown by a protective oxide scale - such a

scale will eventually fail after long-term exposure to aggressive conditions (2, 9). A similar effect was observed for the formation of transient chromium nitrides on Fe-Cr alloys (9). Although the chromium nitrides were overgrown by an oxide, the scales were found to be less protective (9).

While there is a general agreement on alloy degradation via sulfide formation with gaseous S species, mechanisms of a degradation process due to S originating as an impurity from the metal or alloy are controversial. In the past years, it has been suggested that poor adherence of oxide scales is caused by the segregation of sulfur to the scale/metal interface. It was hypothesized that interfacial S weakens the bonding between the oxide and the substrate causing the oxide to spall (3). Consistent with this hypothesis was the observation of improved oxide adhesion for Ni alloys whose sulfur impurity levels were reduced (by hydrogen annealing) (3). Other workers (20), however, have reported that S does not segregate to the intact alloy/oxide interface but rather to the free metal surfaces of voids formed at the interface. These findings (20) were based on SEM and AES depth profiling studies on chromia and alumina-forming alloys. It was argued that the segregation of S to the free metal/alloy surfaces, a thermodynamically favorable process, enhances the formation of voids. This void formation consequently results in the reduction of the contact area between oxide and substrate resulting in oxide spallation. Other investigators (6), on the other hand, have shown that S does segregate to the intact metal-oxide interface. Using AES measurements and an in-situ scratch method, S was not only detected at interfacial voids but also in areas where the chromia and alumina scales were in direct contact with the alloy surface. In addition, TEM and STEM

studies (21) have demonstrated that S was present at the chromia/metal interface but not within the oxide grain boundaries of the scale.

An analogous phenomenon to the segregation of S to the scale/metal interface is S segregation to the grain boundaries in steels and superalloys (Fig. 1.2). A grain boundary is an interface between two single crystals with different crystallographic orientations. The segregation of S and other impurities to the grain boundaries of metals has been linked to grain boundary embrittlement (13-15). This intergranular brittleness is a well-known problem in metallurgy. A catastrophic example of grain embrittlement was the Hinkley Point Power Plant incident where a rotor of a turbine generator exhibited an intergranular fracture mode resulting in the disintegration of the equipment.

Experimental Aspects

In this research, both polycrystalline and single-crystal surfaces were employed as samples. A polycrystalline surface has the advantage of more closely resembling the behavior of real-world materials. However, due to the presence of grains with various crystallographic orientations, a polycrystalline surface is structurally complex and generally not amenable to studies using STM and LEED techniques. The distinct advantage of studying single crystal surfaces is the fact that they are structurally and compositionally well-characterized surfaces. A well-ordered single crystal surface consists mostly of atoms that are in identical equilibrium positions. Single crystals are therefore ideal samples for the investigations of site-specific or orientation-dependent reactions. Fig. 1.3 shows a schematic illustrating the different lattice planes of a body-centered cubic (bcc) crystal, their Miller indices as well as the atomic

arrangements of these surfaces. For a bcc crystal, the most open orientation is the (111) plane while the most dense is the (110) orientation.

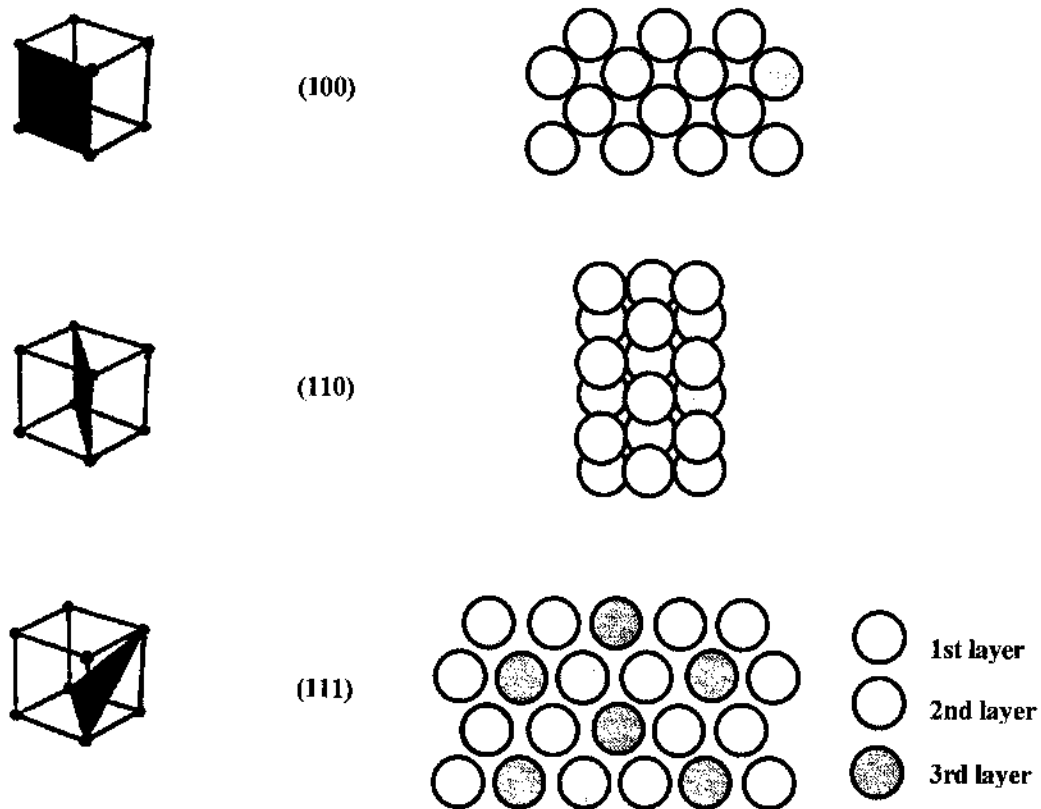


Figure 1.3. Low Miller index surfaces of a bcc crystal.

Because of the asymmetric nature of the surface, the coordination and the electronic structure of surface atoms are different from those of the bulk. The structure of the surface may be very different from a simple bulk terminated model (22). Surface modifications involve changes in the interlayer spacings of the first few layers of the surface (relaxations) and/or lateral displacements of the outermost layers (reconstructions). The adsorption of a chemical

species alters the electronic environment of a surface and may induce the surface to reconstruct. A more massive rearrangement of surface atoms can also occur resulting in the formation of a new crystal orientation (22). This phenomenon is called faceting.

Studies of surfaces at the atomic level necessitate that the surface remain clean at the time scales of the experiments. For most materials, this can only be achieved under ultra-high vacuum conditions (10^{-9} Torr or less). Under UHV environment, a surface can stay clean for about an hour. As mentioned previously, several UHV-based surface analytical methods were employed in this work including electron spectroscopies such as Auger electron spectroscopy (AES), X-ray photoelectron spectroscopy (XPS) and low energy electron diffraction (LEED). These techniques can probe the first few layers of the surface by measuring the kinetic energies of electrons emerging from solids. The surface sensitivity of these techniques is due to the nature of the low-energy electrons. The mean free path of an electron through a solid is dependent upon its kinetic energy (13, 23). For electrons with kinetic energies between 100 eV to 1000 eV, the mean free path is only between 6 Å to 20 Å (13, 23). This means that these low-energy electrons can provide information that is characteristic of the surface only and not of the bulk. In AES and XPS, elastically-scattered secondary electrons from the solid provide information on the elemental composition of the surface. In LEED, the incident electron beam (primary electrons) that have been elastically back-scattered contain information on the surface crystal structure.

In addition to AES and XPS, other surface characterization techniques were used, namely temperature programmed desorption (TPD) and ultra-high vacuum scanning tunneling

microscopy (UHV-STM). TPD is a method that probes adsorbate-surface interactions through analysis of desorbing products from the surface. STM can provide a local real-space picture of a surface. The principles of operation for each of the surface analytical techniques are discussed in more detail below.

XPS. This technique is based on the photoelectric effect. When a surface is irradiated with x-rays, a core-level electron (a photoelectron) is ejected (Fig. 1.4). The vacancy left by the photoelectron is filled by an electron from a higher level which can lead to either X-ray fluorescence, or the radiationless de-excitation process of Auger emission (13, 23) (discussed in the next subsection). The kinetic energy of the photoelectron is given by (13, 23):

$$E_{\text{kin}} = h\nu - E_{\text{B}} - e\Phi_{\text{sp}} \quad (1.8)$$

where $h\nu$ is the energy of the incident X-ray photon, E_{B} is the binding energy of the core-level electron, e is the electronic charge and Φ_{sp} the spectrometer work function.

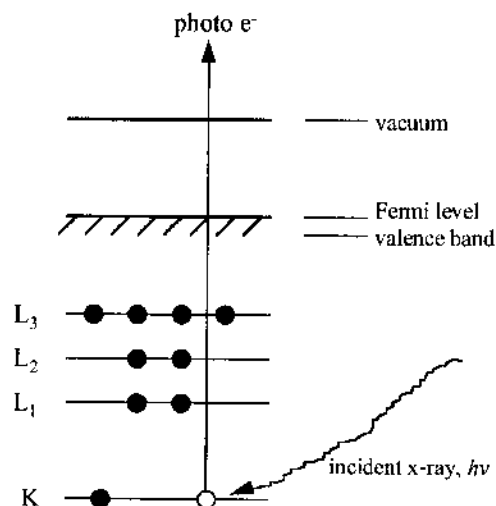


Figure 1.4. Schematic of the photoemission process.

The X-rays are produced by bombardment of anode materials (Al or Mg) with high-energy electrons. For an Al anode, the line energy of the X-rays is 1253.6 eV while for a Mg anode, the energy is 1486.6 eV (13, 23). The photoelectrons are analyzed usually with a concentric hemispherical analyzer (CHA) schematically shown in Fig. 1.5. It consists of two hemispherical sectors. Electrons with different kinetic energies are differentiated by applying a potential difference (U_k) across the inner and outer hemispheres (R_1 and R_2) (24). Electrons of particular energy (eV_e) are allowed to pass through the exit slit only at conditions when the following condition is met:

$$U_k = V_e(R_2/R_1 - R_1/R_2) \quad (1.9)$$

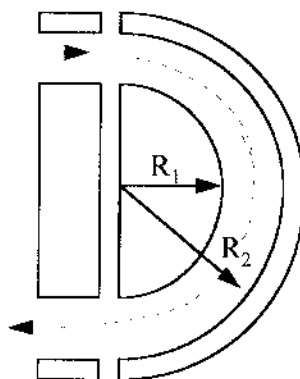


Figure 1.5. Schematic of a concentric hemispherical analyzer (CHA) (24).

XPS is also known as Electron Spectroscopy for Chemical Analysis (ESCA) because it is sensitive to the chemical environment of an element. Information on the chemical state is obtained from the shifts in the binding energies of the electrons (chemical shifts). This arises because the potential felt by a core electron is dependent on the valence electron distribution of the atom (23). During chemical bonding, a spatial redistribution of the valence electrons

occurs changing the valence shell contribution to the potential. The core electron perceives this change in the potential and a shift in the binding energy occurs. A loss of negative charge (oxidation) is usually accompanied by an increase in the binding energy E_B of the core electrons. A XPS spectrum is typically presented as the intensity of the electron signal vs. the binding energy of the electron. A typical full scan XPS spectrum of clean Fe is shown in Fig. 1.6. In addition to the Fe photoelectron peaks, the Fe Auger peaks are also evident.

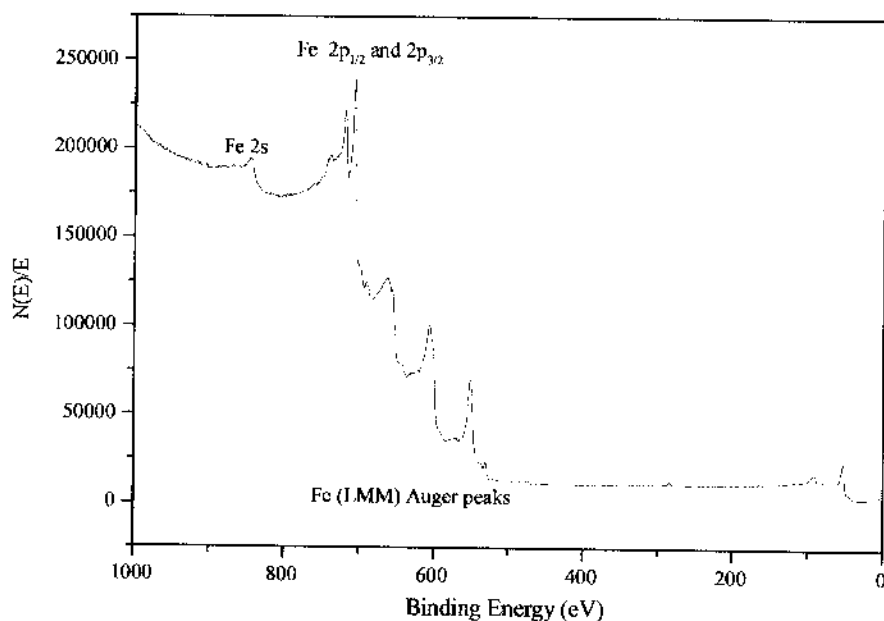


Figure 1.6. Full scan XPS spectrum of clean Fe showing XPS and Auger peaks.

AES. The Auger process involves three electrons. This is schematically depicted in Fig. 1.7. When a beam of electrons or X-rays is impinged onto the sample surface, a core level electron (K) is ejected creating a “hole” (electron vacancy). The core vacancy is filled by an

electron from a higher energy level (L_1). This electronic transition is accompanied by the release of energy which is taken up by a third electron (L_3) causing it to be ejected from the shell. This third electron is the Auger electron. The particular Auger transition is labeled as KL_1L_3 . In contrast to the XPS photoelectron, the kinetic energy of the Auger electron is dependent upon the binding energies of the K, L_1 , and L_3 electrons but not upon the energy of excitation source. The appropriate relationship is given by (13):

$$E_{KL_1L_3} = E_K - E_{L_1} - E_{L_3}^* - e\Phi_{sp} \quad (1.10)$$

where e is the electronic charge and Φ_{sp} the spectrometer work function. The $E_{L_3}^*$ is the binding energy of a doubly-ionized state.

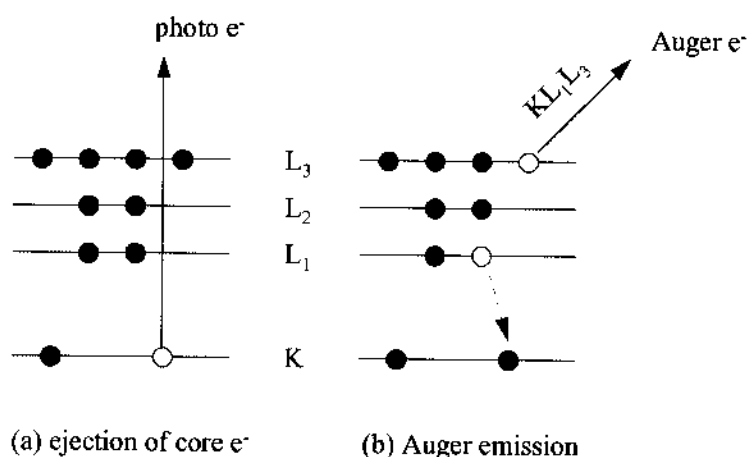


Figure 1.7. Schematic of the Auger process.

Auger emission peaks are usually of low intensities superimposed on a large secondary emission background (see Fig. 1.6). The Auger spectrum is typically presented in a differentiated manner. Differentiation removes the background and enhances the Auger peaks.

The horizontal scale of the spectrum consists of the kinetic energy of the electron, as opposed to an XPS spectrum that has the binding energy as its horizontal scale.

In AES, energy analysis is commonly achieved with either a cylindrical mirror analyzer (CMA) (Fig. 1.8) or a retarding field analyzer (RFA) consisting of LEED optics. The CMA is the preferred energy analyzer because of its superior signal-to-noise ratio. In a CMA, electrons of varying kinetic energies are resolved with a cylindrical electric field achieved by applying a potential to two coaxial electrodes (Fig. 1.8) (23). For a particular applied potential, electrons of the appropriate energy are focussed to the exit and into the detector. A derivative spectrum is obtained by superimposition of a modulating ac voltage on the cylinder potential. Modulation of the Auger signal can also be achieved using a computer and the appropriate software.

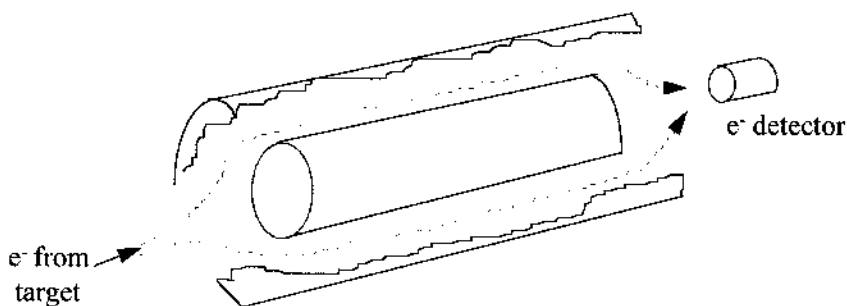


Figure 1.8. Schematic of a cylindrical mirror analyzer (23).

LEED. This is a diffraction technique that is based on backscattered, low-energy electrons. In order to provide information on the atomic arrangement of a surface, the de Broglie wavelength of the probing particle must satisfy the atomic diffraction condition. That is, its wavelength must be smaller or equal to atomic dimensions (22). The de Broglie

wavelength for a particle is given by the following relationship

$$\Sigma_{e^-} = h\sqrt{2mE} \quad (1.11)$$

where h is the Planck's constant, m is the mass of the particle and E is its energy. For an electron, the de Broglie equation is more conveniently expressed as

$$\Sigma_{e^-} = \sqrt{150/E} \text{ (eV)} \quad (1.12)$$

Therefore, electrons with very low kinetic energies (10 - 300 eV) can be used to determine the crystalline order of a surface.

A schematic of a LEED experiment is shown in Fig. 1.9. A monoenergetic beam of electrons (10 eV to 300 eV) is impinged on a single crystal surface. A set of hemispherical grids is used to filter out the inelastically backscattered electrons and allow only the elastically backscattered electrons to form a diffracted pattern on a phosphor-coated screen (25). The diffracted spots are the result of the constructive interference of wavelets of elastically-

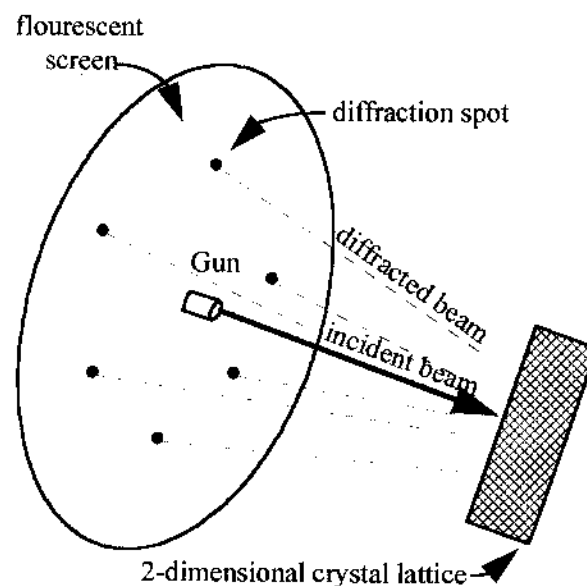


Figure 1.9. Schematic of a LEED experimental set-up (25).

backscattered electrons. The condition for constructive interference is

$$n\lambda = a \sin\theta, \quad (1.13)$$

where $n\lambda$ is the integral number of wavelengths and $a \sin\theta$ is the projection of the interatomic spacing along the backscattering direction (23). For a two-dimensional periodic arrangement of atoms, two sets of diffraction conditions must be met simultaneously and these are

$$n_a\lambda_a = a \sin\theta_a \text{ and } n_b\lambda_b = b \sin\theta_b, \quad (1.14)$$

where a and b correspond to the interatomic spacing of the surface net (23). Owing to the fact that these diffraction conditions must be met simultaneously, an electron from a two-dimensional array can only be scattered along a set of lines radiating away from the surface.

These lines of diffracted electrons are perceived as spots on a phosphorescent screen (Fig. 1.9). Each of the diffraction spot can be denoted as (n_a, n_b) where n_a and n_b are the integral number of wavelengths, in the a and b directions of the backscattered beam of electrons (23).

A diffraction pattern corresponds to the reciprocal lattice of the surface. The reciprocal lattice can be transformed to the real-space lattice using the relationships between their basis vectors (25). In the case of a surface reconstruction where a new surface periodicity ("superstructure" or an ordered overlayer) is superimposed on the original substrate surface net, a change in the diffraction pattern occurs. By visual comparison of the unreconstructed pattern and the new LEED pattern, it is possible to determine the symmetry of a new surface structure relative to the substrate. It is important to note that a particular LEED pattern is not unique for one real-space lattice. Different atomic arrangements can give identical diffraction patterns if they possess identical periodicities. More detailed information on the actual

locations of atoms can be obtained by analysis of the intensity of diffraction spots as a function of electron energy (I/V measurements) (23). Such measurements require a current detector to the schematic set-up in Fig. 1.9.

The formation of a new structure or periodicity on a surface that is different from that of the bulk is either due to clean surface reconstruction or due to the adsorption of a chemical species which forms an ordered overlayer on the surface. In LEED, the formation of such reconstructed surfaces or overlayer structures are denoted by the Wood method which uses the general form $S(hkl)\text{-}p(u\times v)R\phi^\circ$ or $S(hkl)\text{-}c(u\times v)R\phi^\circ$ depending on whether the structure is centered (c) or primitive (p). S stands for the substrate element, hkl are the Miller indices of the crystallographic surface. The p symbol in $p(u\times v)R\phi^\circ$ is usually dropped for abbreviation. u and v are the scale factors relating the surface atom or adsorbate and substrate unit cell vectors. The $R\phi^\circ$ indicates a rotation of the superstructure or overlayer by ϕ° from the substrate lattice. The Wood notation is more widely used but is applicable only when the angle of the basis vectors in the overlayer is equal to the angle of the basis vectors in the substrate.

TPD. In this method, gas molecules are adsorbed on a surface at a low temperature. A linear heating rate is applied to the sample and species adsorbed on the surface will desorb at a rate which increases with temperature. The temperature rise of a TPD experiment is typically expressed as $T = T_0 + It$ where T_0 is the starting temperature, I is a constant of proportionality and t is time. The desorbing species are identified by a quadrupole mass analyzer (QMA). A schematic of a TPD set-up is shown in Fig. 1.10. The QMA which consists of four parallel rod-shaped electrodes serves as a mass filter. By application of a varying electrical field on its

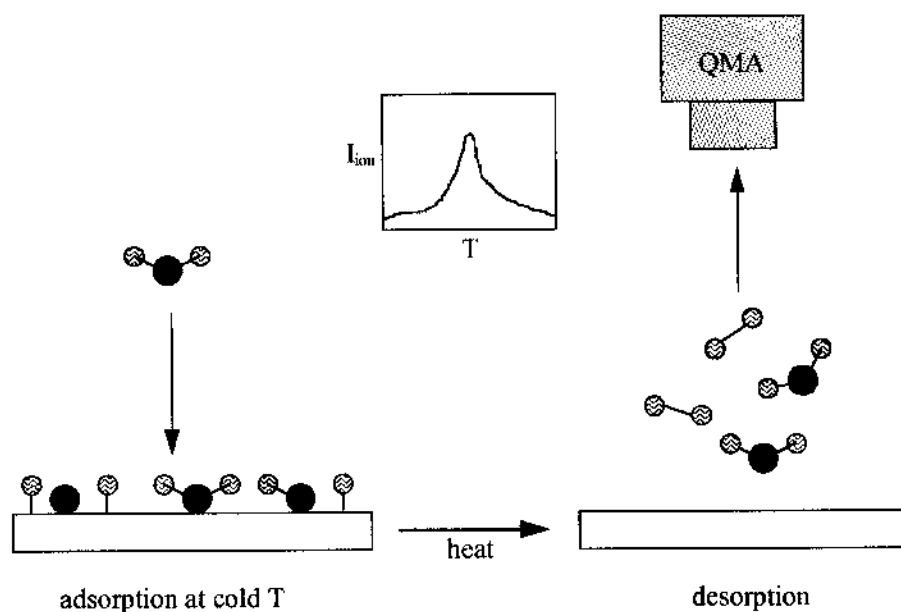


Figure 1.10. Schematic of a TPD process. Inset: a desorption spectrum.

electrodes, only ions of a particular mass-to-charge ratio are allowed to pass to the detector. It is important for the sample to be positioned as close as possible to the mass spectrometer so that the detection of desorption products is exclusive of the sample surface only and not due to the outgassing from other components of the system. This can be accomplished by masking the QMA with a small aperture (line-of-sight detection).

The TPD spectrum consists of the intensity signal of desorbing gas (x-axis) as a function of temperature or time (y-axis) (Fig. 1.10, inset). Kinetic and thermodynamic information can be deduced from TPD data. The maximum peak of desorption of a TPD spectrum is reflective of the strength of the bonding between the surface and the adsorbate. If one assumes a certain order of reaction, the energy of activation for desorption can be obtained based on the temperature of maximum desorption (26). The activation energy of desorption is

related to the heat of adsorption by the following equation:

$$E_d = E_a + \Delta H_{\text{ads}} \quad (1.15)$$

In cases when the adsorption is non-activated,

$$E_d = \Delta H_{\text{ads}} \quad (1.16)$$

UHV-STM. This instrument is based on quantum tunneling between a very sharp metal tip and a conductive surface (Fig. 1.11). The tip is brought within atomic distances to the surface and electrons tunnel through a vacuum barrier (27). The movement of the tip is controlled using a piezoelectric material which expands in atomic dimensions under an applied potential. A feedback circuit constantly adjusts the tip height so that a constant tunneling current is maintained. The tunnel current (I_t) varies exponentially with both the distance (d) of

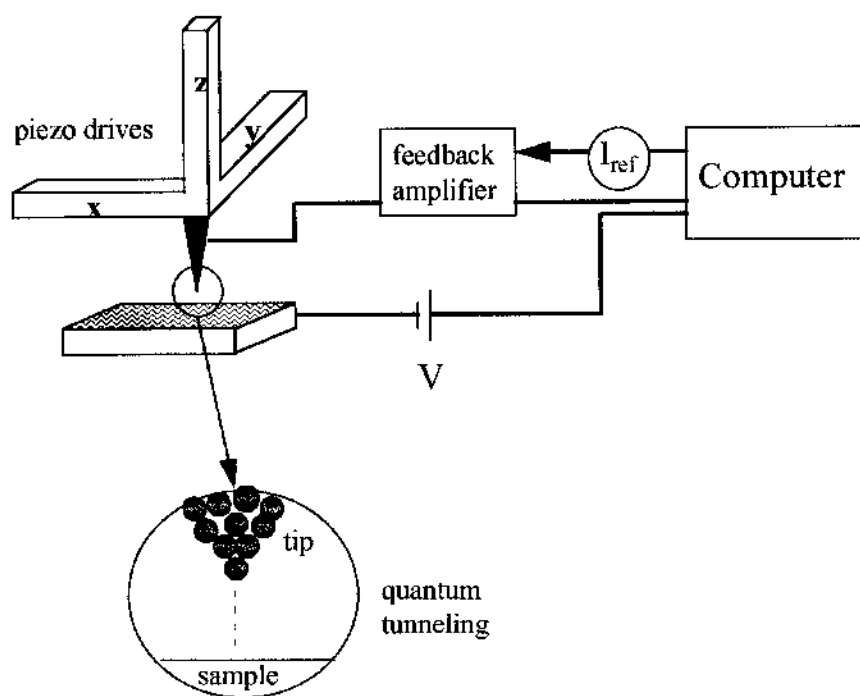


Figure 1.11. Schematic of a scanning tunneling microscope (STM).

the tip from the surface and its work function (Φ) ($I_t \approx \exp(-\Phi d/2)$). Atomic-level variations in the electronic charge density can be mapped by moving the tip while keeping the current constant.

Chapter References

- (1) Baxter, D. J.; Natesan, K. *Oxidation of Metals*. **1989**, 31(3/4), 305.
- (2) Lobnig, R. E.; Grabke, H. J. *Corrosion Science*. **1990**, 30(10), 1045.
- (3) Smialek, J. M.; Jayne, D. T.; Schaeffer, J. C.; Murphy, W. H. *Thin Solid Films*. **1994**, 253, 285.
- (4) Forest, C.; Davidson, J. H. *Oxidation of Metals*. **1995**, 43(5/6), 479.
- (5) Stasik, M. C.; Pattit, F. S.; Meier, G. H. *Scripta Metallurgica et Materiala*. **1994**, 31(12), 1645.
- (6) Stringer, J.; Hou, P. Y. *Oxidation of Metals*. **1992**, 38(5/6), 323.
- (7) Wiemer, D.; Grabke, H. J.; Viehhaus, H. *Fresenius Journal of Analytical Chemistry*. **1991**, 341, 402.
- (8) Colson, J. C.; Larpin, J. P. *MRS Bulletin*. October **1994**, 23.
- (9) Meier, G. H. *Material Science Engineering*. **1989**, A120, 1.
- (10) Li, L. C.; Gesmundo, F.; Viani, F.; Toledo, G. P. *High Temperature Material Processes*. **1993**, 12(4), 199.
- (11) Gesmundo, F.; Young, D. J.; Roy, S. K. *High Temperature Material Processes*. **1989**, 8(3), 149.
- (12) Stott, F. H. *Reports of Progress in Physics*. **1987**, 50, 861.
- (13) Briggs D.; Seah, M.P. *Practical Surface Analysis*, Vol. 1, 2nd edition; John Wiley and Sons: England, 1990; Chap 6.
- (14) Oudar, J. *Material Science Engineering*. **1980**, 42, 101.

- (15) Briant, C. L. *MRS Bulletin*, October **1990**, 26.
- (16) Jones, D. A. *Principles and Prevention of Corrosion*; Macmillan Publishing Company, New York, New York, 1992; Chap. 12.
- (17) Scully, J. C. *The Fundamentals of Corrosion*; Second Edition; Pergamun Press, New York, 1990; Chap. 1.
- (18) Pieraggi, B.; Rapp, R. A. *Journal of Electrochemical Society*. **1993**, *140(10)*, 2844.
- (19) Shores, D. A. *The Electrochemical Society Interface*. Spring **1997**, *6(1)*, 42.
- (20) Grabke, H. J.; Wierner, D.; Viehhaus, H. *Applied Surface Science*. **1991**, *47*, 243.
- (21) Fox, P.; Lees, D. G.; Lorimer, G. W. *Oxidation of Metals*. **1991**, *36(5/6)*, 491.
- (22) Somorjai, G. A. *Introduction to Surface Chemistry and Catalysis*; John Wiley and Sons, New York, 1994; Chap. 2.
- (23) Feldman, L. C.; Mayer, J. W. *Fundamentals of Surface and Thin Film Analysis*; PTR Prentice Hall, Inc., New Jersey, 1986; Chap. 7.
- (24) Ertl, G.; Koppers, J. *Low Energy Electrons and Surface Chemistry*; VCH Publishers, New York 1985.
- (25) Ohtani, H.; Kao, C.-T.; Van Hove, M. A.; G. A. Somorjai. *Progress in Surface Science*. **1986**, *23(2/3)*, 155.
- (26) Redhead, P. A. *Vacuum* **1962**, *12*, 203.
- (27) Tersoff, J.; Lang, N. D. in *Scanning Tunneling Microscopy*, Vol. 27. edited by Stroscio, J. A.; Kaiser, W. J.; Academic Press, Inc., California, 1993; Chap. 1.

CHAPTER 2

TPD AND AES STUDIES: SULFUR ON IRON METAL, OXIDE SURFACES AND INTERFACES

Introduction

The interfacial chemistry of S and H₂S on Fe metal, Fe oxide surfaces and interfaces is studied using a combination of temperature programmed desorption (TPD) and Auger electron spectroscopy (AES). Results demonstrate the deleterious effect of S when present at the metal-oxide interface. S located at the metal-oxide interface reacts with the oxide to form SO₂. This S-O bond formation suggests a mechanism for the S-induced oxide instability. In contrast to interfacial S, S adsorbed (S_(a)) on the oxide surface does not form SO₂ under UHV conditions. However, SO₂ formation occurs in the presence of H₂O or O₂ vapor which is attributed to a reaction between S adsorbed on the oxide surface and H₂O or O₂ vapor. For S_(a) on the Fe(poly) metal surface, no such SO₂ formation is observed. These data indicate that the initial adsorption site of the S atom (metal vs. oxide) exerts a critical influence on subsequent oxidation chemistry.

Experimental

Experiments were carried out in a stainless steel turbomolecularly pumped ultra high vacuum (UHV) system (Fig. 2.1) equipped for TPD and AES. Pressure after bakeout was 3 × 10⁻¹⁰ Torr. The sample was cleaned by repeated cycles of Argon ion sputtering and annealing

(to 900 K) for several weeks. Sample temperature was varied continually between 85 K and 1000 K by a combination of direct resistive heating and liquid nitrogen cooling. The sample was a 10 mm square, 0.5 mm thick polycrystalline Fe foil (99.998 % purity) spotwelded to two Ta leads. Sample temperature was measured by a chromel-alumel thermocouple spotwelded to the back of the sample. Sample cleanliness was determined by AES. The sample was considered clean when S(LMM) and other contaminant peaks were less than 5 % of the Fe(MVV) peak intensity (peak-to-peak height).

AES spectra were excited using 3 KeV electrons, and recorded in the differential mode using a commercial cylindrical mirror analyzer, lock-in amplifier (4 eV peak-to-peak

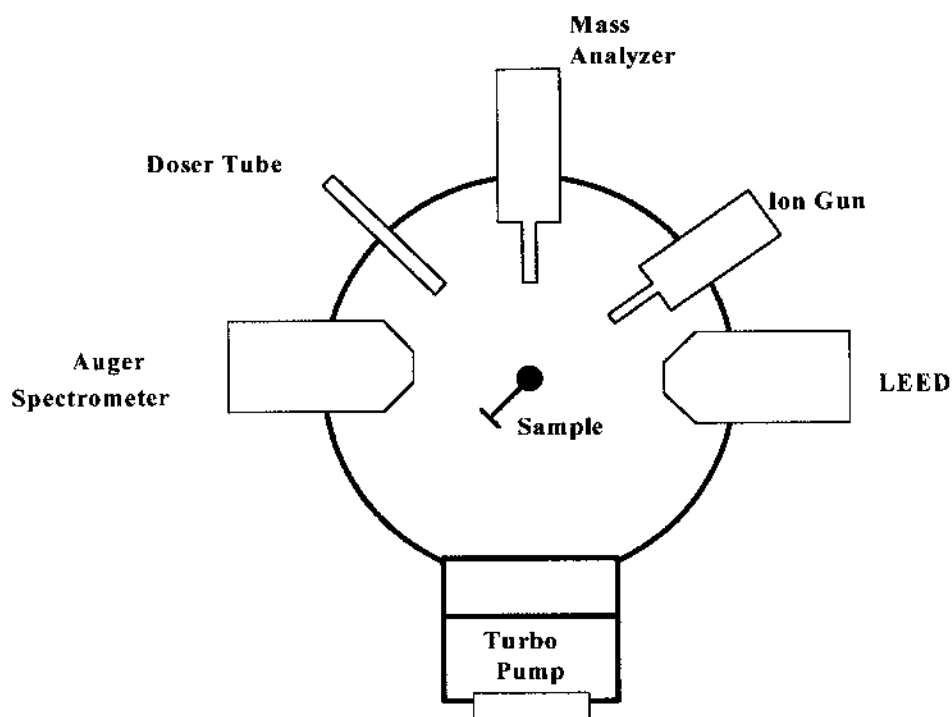


Figure 2.1. Schematic of the UHV system used in this study.

modulation), and x-y recorder. TPD spectra were recorded with a linear heating rate (10 ± 2 K/s) using a quadrupole mass spectrometer collimated for line-of-sight to the sample. The spectrometer was interfaced to a personal computer to allow recording of up to 10 different amu settings during a single run.

H₂S (99.95 %) and O₂ (99.995 %) were admitted to the chamber by backfilling using 2 separate dosers and manually operated leak valves. Background pressures were determined with a nude ion gauge calibrated for dinitrogen and mounted out-of-line-of-sight to the sample, in order to minimize gauge-induced decomposition. Gas exposures are reported here in terms of background pressure x duration of dose (1 Langmuir (L)) = 10^{-6} Torr-sec), and have not been corrected for flux to the sample or ion gauge sensitivity.

A sulfided sample was prepared by exposure of clean Fe to H₂S at 85 K with subsequent anneal to 500 K to remove all adsorbed hydrogen. To create a thin oxide overlayer, the sulfided Fe surface (corresponding to saturation coverage) was subsequently exposed to 900 L of O₂ at 300 K. Oxide formation was evidenced by the appearance of a bifurcated Fe(MVV) lineshape (1). Attenuation of the S AES intensity during the oxidation indicates that adsorbed S is overgrown by the oxide, in agreement with results of other investigations (2, 3). A rough estimate (4) of the oxide thickness yielded 6 Å.

Oxidation of the Fe metal with no S contamination was accomplished in a similar manner described above. Bifurcation was observed on the clean Fe surface after approximately 70 L of O₂ exposure, compared to about 900 L on the S-covered Fe surface indicating a drastic decrease in the sticking coefficient of O₂ on the S-covered Fe surface. A similar study (5) on a

S-covered Fe(111) surface has determined the sticking coefficient of O_2 at 300 K to be 10 times smaller than on a clean Fe(111) surface, consistent with the results here.

The unavoidable adsorption of H_2O at 85 K made it difficult to unambiguously investigate the reaction of H_2S with Fe metal and Fe oxide surfaces in the absence of H_2O at cold temperature. To avoid this complication, some studies were performed near room temperature at which negligible H_2O adsorption occurs on the time scales of these experiments (6). Clean Fe metal and Fe oxide surfaces were exposed to H_2S near room temperature with no cooldown to low temperature. Subsequently, TPD and AES measurements were performed following the adsorption of H_2S on the samples. Additionally, TPD experiments were performed at room temperature in an overpressure of H_2O (10^{-8} Torr) to unambiguously characterize the reaction between H_2O and $S_{(a)}$ on Fe metal and Fe oxide surfaces. For these experiments, H_2O was introduced into the chamber by backfilling using a separate doser. Before dosing, the H_2O underwent repeated freeze-thaw-pump cycles to ensure sufficient degassing. Corresponding measurements performed in an overpressure of O_2 were also carried out to investigate possible interactions between $S_{(a)}$ on Fe metal and O_2 and between $S_{(a)}$ on Fe oxide and O_2 .

Results

Three different types of S-interface/surface interactions were investigated here and the results are presented in the following order: (a) H_2S/S on the Fe metal surface (in UHV and in O_2 or H_2O environment) (b) S located at or near the metal-oxide interface and (c) H_2S/S on the Fe oxide (in UHV and in O_2 or H_2O environment).

H₂S/S on Fe Metal

Figure 2.2 shows the variations in relative S coverage ($S_{(152)}/Fe_{(651)}$) Auger intensity ratios on clean Fe as a function of H₂S exposure. The data show that repeated exposures of H₂S at 80 K (Fig. 2.2a) do not result in saturation. This indicates multilayer formation at 80 K. Multilayer formation for low temperature H₂S adsorption on transition metal surfaces has been

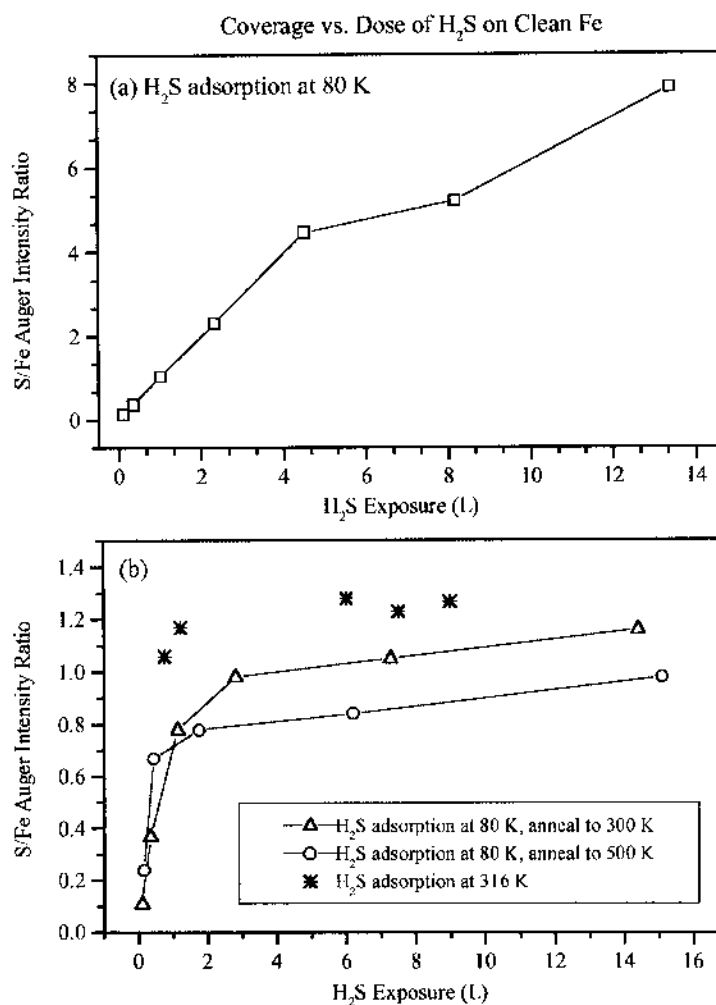


Figure 2.2. Variations in the $S_{(152)}/Fe_{(651)}$ Auger peak-to-peak intensity ratios as a function of H₂S exposure on a clean Fe(poly) surface: (a) adsorption at 80 K (b) adsorption at 80 K with subsequent annealing to 300 K or 500 K and adsorption at 316 K.

reported (7, 8). Figure 2.2b shows a comparison of S coverage vs. exposure with subsequent annealing to either 300 K or 500 K. In addition, the corresponding data for H₂S dosing carried out at 316 K (no annealing) is presented (Fig. 2.2b). The results (Fig. 2.2b) indicate that saturation is approached for all conditions for exposures of ≥ 3 L. Further, the data show a lower saturation coverage for the 500 K anneal. That this might be due to desorption of S-containing species between 300 K and 500 K is contradicted by the failure to observe H₂S or S₂ evolution during TPD of adsorbed H₂S. It appears that some diffusion of S into the sample occurs during the 500 K anneal. For a given sample, differences in saturation coverage upon annealing were reproducible. Such differences were not, however, reproducible between different Fe samples. These inconsistencies may be due to differences in grain size as well as annealing history which presumably affect the rate of impurity diffusion within the crystal.

TPD of H₂S following adsorption at 80 K (Fig. 2.3, 2.4a) indicates the evolution of H₂. H₂ has a maximum desorption peak at 230 K and desorption is complete by 500 K. This is significantly different from the H₂ evolution from a H₂O-dosed Fe surface, which has a maximum desorption peak at 375 K (9). In addition to H₂, H₂O was observed to desorb from the sulfided surface (Fig. 2.3, 2.4a). H₂O and H₂ desorption behavior are shown in Fig. 2.3 for an Fe surface exposed to 6 L H₂S at 80 K and annealed to 500 K prior to TPD. Repeated anneals of the sulfided layer to 900 K in the course of TPD eliminated any significant H₂ yield. However, some H₂O desorption was observed even after repeated annealing of the sulfided surface and in the absence of exposure to O₂. The intensity and temperature dependence of the H₂O yield remained roughly constant even after repeated annealing of the sulfided surface to

900 K (Fig. 2.3b). In addition, no O(KLL) signal is observed after adsorption of H₂S on clean Fe at 80 K. This rules out an impurity in the H₂S as the cause of H₂O desorption. AES measurements of a clean Fe surface at 80 K at various intervals over 600 s reveal the gradual growth of a small but detectable O(KLL) signal. H₂O desorption similar to Fig. 2.3b was observed for TPD of the clean surface after cooling to 80 K. This confirms that the source of H₂O signal is readsorption of H₂O from the ambient while the sample is at 80 K.

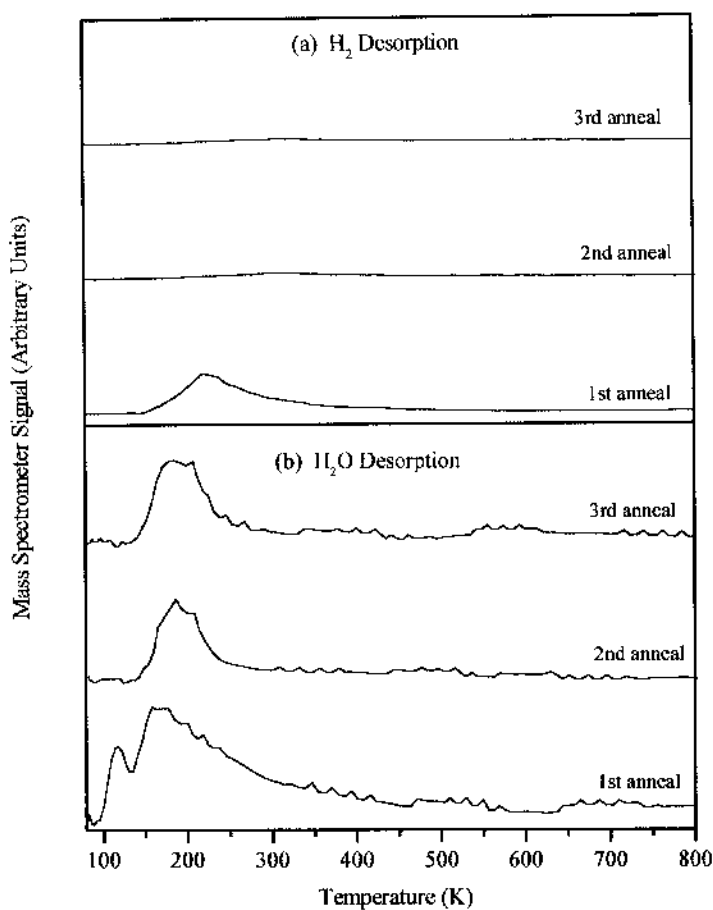


Figure 2.3. (a) H₂ and (b) H₂O desorption from a cleaned Fe(poly) surface exposed to 6 L H₂S at 80 K. Curves are for successive TPD measurements without additional gas exposures. Each TPD measurement annealed the sample to 900 K.

TPD data of a clean Fe surface exposed to 6 L of H_2S at 85 K are presented in Fig.2.4a. As alluded to previously, H_2 and H_2O desorb from the surface (Fig. 2.4a). In addition, a small amount of H_2S desorbed at 110 K which is attributable to multilayer H_2S (7, 8). As discussed previously, the H_2O desorption observed here is attributed to adsorption of H_2O from the chamber ambient while the sample was at 85 K. The H_2O peak has two components: a sharp peak at 110 K and a broad peak between 150 K and 340 K. The 110 K

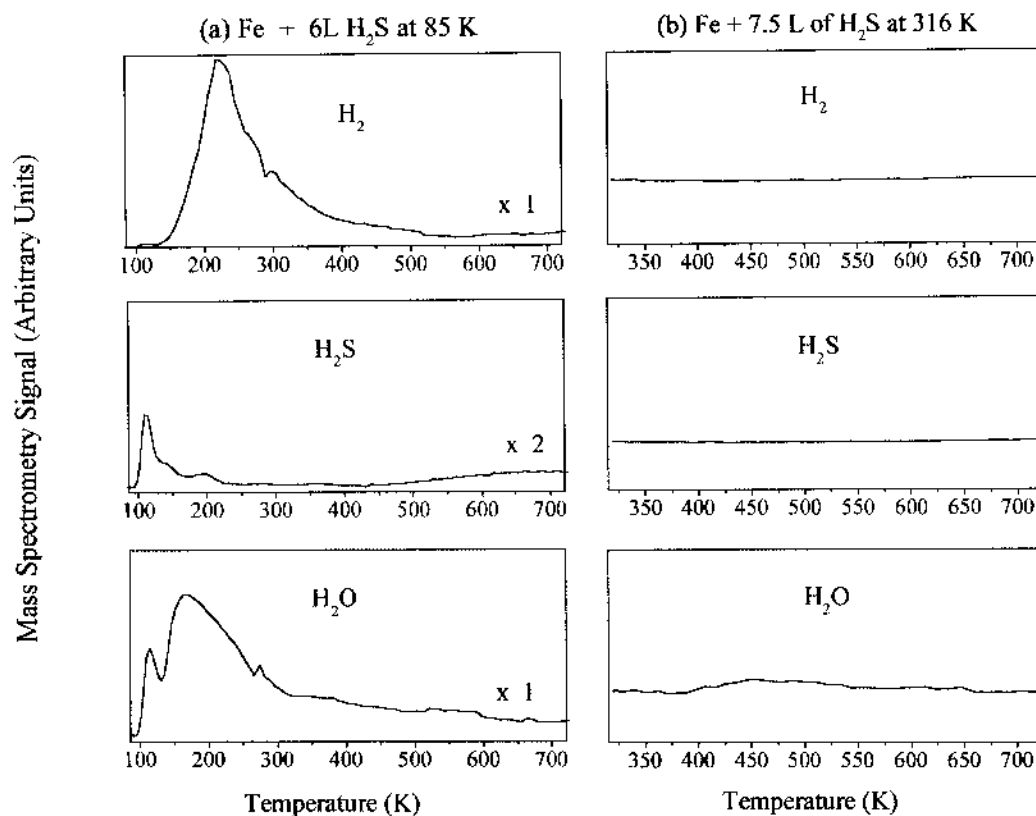


Figure 2.4. (a) TPD spectra obtained from a clean Fe(poly) surface following adsorption of 6 L of H_2S at 85 K. H_2 , H_2S and H_2O desorption are observed. (b) TPD spectra obtained from a clean Fe(poly) surface following adsorption of 7.5 L of H_2S at 316 K. No H_2 , H_2S nor H_2O desorption were observed.

desorption temperature is much lower than observed H₂O multilayer desorption from Fe (9) or other transition metal surfaces (10) but consistent with H₂S multilayer desorption (7, 8). The 110 K H₂O desorption is therefore attributed to H₂O physisorbed on adsorbed H₂S which desorbs with the H₂S multilayer. The failure to observe a 110 K-H₂O desorption peak in the absence of an H₂S multilayer confirms this assignment. Repeated thermal cycling of the sulfided sample between 85 K and 720 K in UHV did not produce any H₂ or H₂S. Further, no SO₂, SO, S₂ were observed to desorb from the surface.

For comparison, TPD data from a clean Fe surface exposed to H₂S at 316 K are displayed in Fig. 2.4b. No H₂, H₂S or H₂O desorption were observed. The absence of H₂ evolution indicates that all the H₂ has “desorbed“ (i.e., H₂S → S_(a) + H₂↑) while dosing at 316 K, consistent with previous results (11).

H₂S/S on Fe Metal in H₂O or O₂ environment

To test for possible formation of SO₂ between S_(a) on Fe and H₂O vapor, TPD measurements were carried out on sulfided Fe surfaces (with varying S coverages) in a partial pressure of H₂O vapor. The sulfided samples were prepared either by exposure of clean Fe to H₂S at 80 K with subsequent annealing to 500 K (which removes all H₂) or dosing with H₂S directly at 316 K. TPD measurements were performed in an overpressure of H₂O (10⁻⁸ Torr). In all cases, no SO₂ desorption or any other S-containing product was detected. This is consistent with TPD results obtained from an Fe metal surface with coadsorbed H₂S and H₂O. Possible interaction between sulfided Fe metal and O₂ was also investigated. TPD measurements were performed in an overpressure of O₂ (10⁻⁸ Torr). Again, no S-containing species were observed to desorb from the surface.

Sulfur Lineshape Changes

Variations on the Auger lineshape of S adsorbed on Fe were observed that are dependent on the temperature at which the H₂S exposure was carried out, as well as on S coverage. Fig. 2.5 shows the Auger spectra of S on Fe as a function of varying conditions for H₂S dosing. When H₂S gas was dosed at 85 K, the S(LMM) spectrum consisted of a single peak (Fig. 2.5a). Dosing at 85 K did not saturate and both low and high exposures of H₂S resulted in the appearance of a single S(LMM) peak. However, when H₂S was dosed at 85 K followed by a 500 K anneal, the S(LMM) shows a subtle but discernible appearance of a

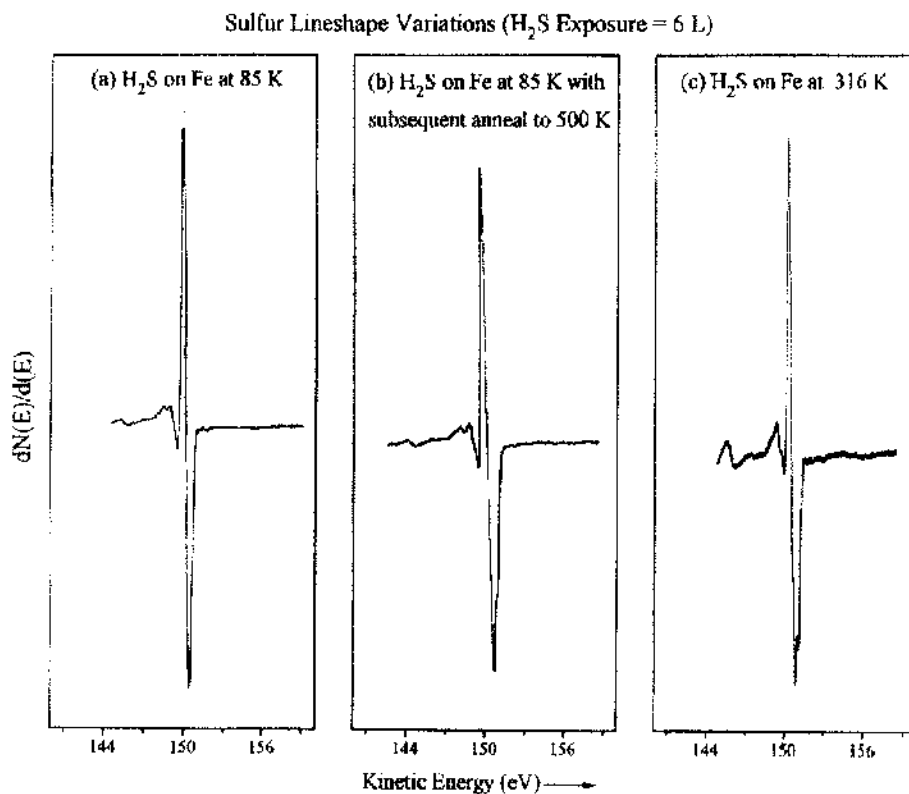


Figure 2.5. S(LMM) Auger lineshape as a function of varying H₂S dosing conditions on clean Fe(poly) surface: (a) adsorption of 6 L of H₂S at 85 K (b) adsorption of 6 L of H₂S at 85 K with subsequent annealing to 500 K (c) adsorption of 6 L of H₂S at 316 K (no annealing). The spectra have been normalized to the same scale for clarity.

second peak on the high energy side (Fig. 2.5b). Furthermore, H₂S dosing carried out directly at a temperature of 316 K shows a S lineshape whose peak on the high energy side is enhanced resulting in a bifurcated S(LMM) lineshape (Fig. 2.5c). Low exposures (< 7.5 L) of H₂S at 316 K resulted in the bifurcated S lineshape while higher exposures (> ~8.5 L) resulted in a single peak. Similar changes in the S lineshape were reported in a previous study (2) on Fe(111). In that study (2), the authors proposed that the S single peak is due to S cluster formation on the Fe(111) surface while a bifurcated S peak denotes a stronger interaction between Fe and S. In the present study, the appearance of a S single peak occurs only at high exposures of H₂S at 316 K, in agreement with the proposed model (2) of S clusters on Fe. A study (8) of S(LMM) lineshape analysis for S on Ni(110) indicated that the change in the S lineshape is not associated with the conversion from a molecular state (H₂S or SH) to chemisorbed S atoms. This present study show that the sulfided surface is completely dehydrogenated by 500 K (Fig. 2.4a). Moreover, the S peak bifurcation on the 500 K-annealed sample is subtle and poorly defined compared to the bifurcation of the S lineshape when the H₂S exposure was carried out at 316 K. These results therefore indicate no correlation between complete H₂ removal and the bifurcated S peak, in agreement with previous work (8). Instead, changes in the S(LMM) lineshape appear to be a function of S coverage, a single peak spectrum indicating S-S interactions.

Changes in the S lineshape were also observed upon exposure of S/Fe to O₂ (not shown). When a sulfided Fe surface was exposed to a partial pressure of O₂ (900 L) at 300 K, an oxide overlayer was formed which consequently attenuated the S peak. The attenuation is

accompanied by a lineshape change from the bifurcated S(LMM) to the S single peak. Upon annealing of the Fe-S-oxide surface to 720 K, Auger measurements reveal a broadening of the S lineshape, suggesting a return to the original S state. These results are in accord with previous studies (2).

S at the Fe-oxide interface: SO₂ Formation

To investigate the chemistry of interfacial S on the Fe-oxide interface, experiments were carried out on thin oxide layer grown on a pre-sulfided Fe surface. Oxidation of the sulfided Fe layer was carried out by exposure to O₂ at 300 K. This procedure eventually results in the formation of a very thin oxide overlayer (~6 Å). Auger measurements (Fig. 2.6a, b) show that the S intensity is attenuated by oxygen exposures (O₂ pressure = 10⁻⁶ Torr) at 300 K, indicating that the oxide layer forms over the S layer. This is consistent with previous studies on Fe (2) and Ni (3) which indicate that S signal attenuation is due to the growth of a thin oxide over the S layer, resulting in the incorporation of S at or near the interface between the metal and metal oxide. The AES data (Fig. 2.6) indicate that O₂ exposures do result in oxide formation, rather than in an S-O surface layer, as evidenced by changes in the Fe (LMM) lineshape (Fig. 2.6a, b). Similar changes in Fe AES lineshape upon oxidation have been reported (1). The attenuation of the S signal accompanied by Fe oxide formation therefore indicate the growth of an oxide layer over the sulfur, as reported by other studies (2, 3).

Following TPD in which the sample is heated up to 900 K, AES spectra (Fig. 2.6c) showed an enhanced S signal and the loss of most (but not all) the O(KLL) signal. The Fe(MVV) signal following annealing (Fig. 2.6c) is characteristic of reduced Fe (1). These

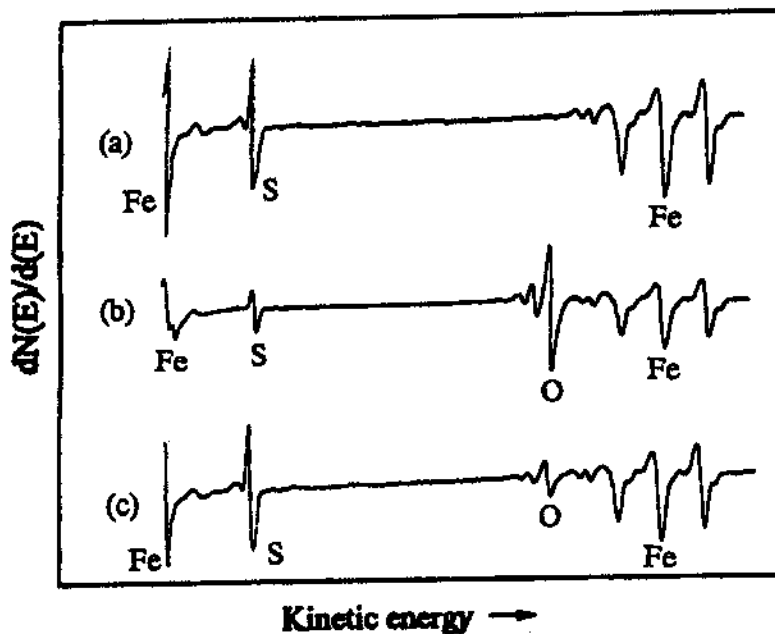


Figure 2.6. AES spectra of an Fe(poly) surface: (a) after exposure to 6 L H_2S at 80 K and annealing to 500 K (b) after subsequent exposure to 1258 L O_2 at 300 K, and (c) after heating the oxidized sample to 900 K during TPD.

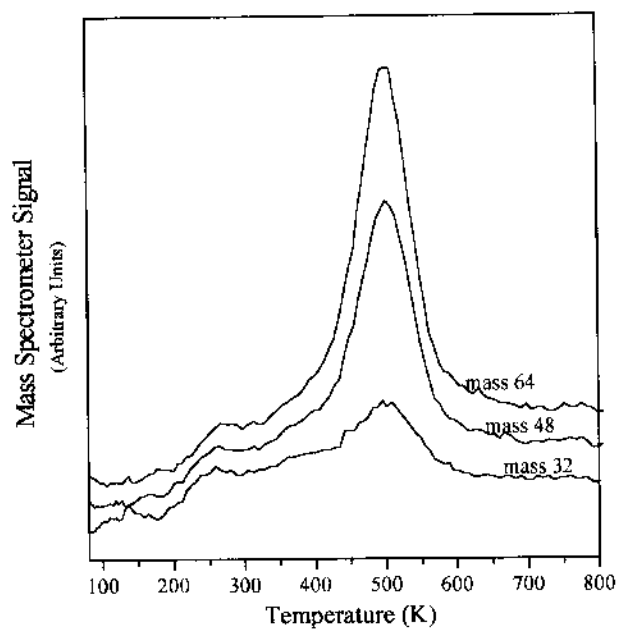


Figure 2.7. Cracking pattern analysis of a surface exposed to 6 L of H_2S (80 K, 500 K anneal) followed by 1258 L of O_2 at 300K.

results indicate the removal of the oxide overlayer upon annealing, though some oxygen remains within the surface region. For some spectra, the relative S(LMM) intensity was higher after the disappearance of the oxide than before oxidation, indicating that some diffusion of S to the surface had occurred during the TPD process. In the absence of S, the oxide remained stable on the Fe surface in UHV up to at least 720 K (the highest temperature examined for S-free surfaces).

TPD measurements of the oxidized presulfided Fe surface reveal the desorption of SO_2 . Figure 2.7 shows the cracking pattern behavior for a sulfided surface exposed to 1258 L O_2 at 300 K. The assignment of the amu 64 peak to SO_2 was confirmed by the similar desorption behavior observed for amu 48 (SO^+) and amu 32 (S^+ or O_2^-) (Fig. 2.7). No H_2 was observed, nor were any Fe-containing fragments (Fe, FeS, FeO) observed.

The amount of SO_2 desorbed varies with O_2 exposure (Fig. 2.8). Since no S_2 , Fe-S or Fe-O was observed, the data show that SO_2 is the only reaction product of the sulfide and overlying oxide layer. The SO_2 desorption (Fig. 2.7, 2.8) begins above 300 K and displays a desorption maximum at 500 K. The temperature of the desorption maximum does not change with O_2 exposure (Fig. 2.8). The SO_2 desorption process is completed by 700 K. XPS and AES studies (2) of the oxidation of S/Fe(111) report the disappearance of the oxide overlayer by 720 K, consistent with these results.

The dependence of SO_2 yield on O_2 exposure is displayed graphically in Fig. 2.9, along with the relative attenuation of the S(LMM) signal (S/O AES intensity). The increase in SO_2 yield is monotonic with increasing O_2 exposure, but also non-linear (Fig.

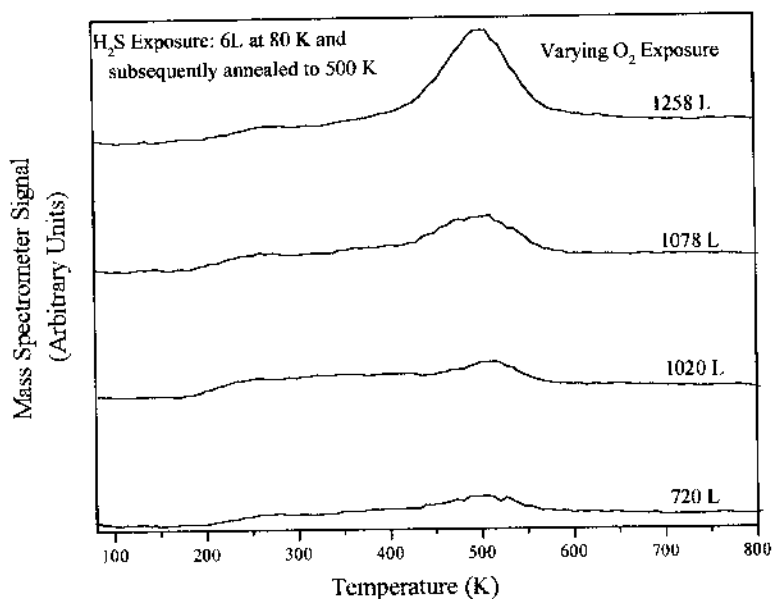


Figure 2.8. Dependence of SO_2 TPD yield on O_2 exposure at 300 K. Each curve was taken from a cleaned Fe(poly) surface exposed to 6 L H_2S (80 K, 500 K anneal), and varying O_2 exposure at 300 K.

2.9a). In particular, the SO_2 yield increase rapidly with O_2 exposure above 1000 L. At this point the relative S(LMM) intensity also decreases abruptly (Fig. 2.9). Additionally, the double-peaked Fe(MVV) signal, characteristic of an Fe oxide (1), is observed only for exposures > 1000 L.

In addition to SO_2 , H_2O desorption from the oxidized sulfided surface was also observed (not shown). Possible origins of the H_2O are adsorbed H_2O due to cooldown to 85 K and recombinant H_2O from the hydroxylated oxide surface. To examine possible H_2O evolution from the oxide, TPD measurements were carried out on a S-free oxide surface starting at 300 K (no cooldown) to avoid H_2O adsorption at cold temperature. Fig. 2.10a displays the H_2O desorption from the S-free oxide with a maximum desorption temperature at

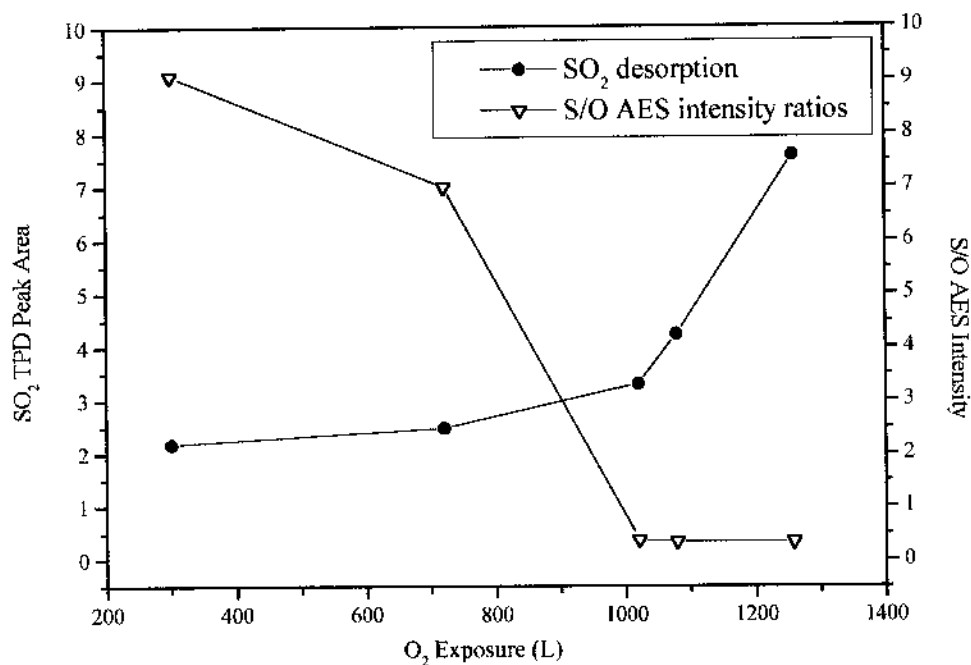


Figure 2.9. (a) SO₂ desorption peak area and (b) S(LMM)/O(KLL) AES intensity ratios as a function of O₂ exposure (L). The initial sulfidation of the Fe surface was carried out by exposure to 6 L H₂S at 80 K and subsequent annealing to 500 K.

475 K. This demonstrates that some H₂O originated from the oxide itself, an indication that the oxide was initially hydroxylated. Annealing of a hydroxylated oxide produces H₂O via the following reaction pathway: $\text{OH}_{(a)} + \text{OH}_{(a)} \rightarrow \text{H}_2\text{O}\uparrow + \text{O}_{(a)}$ (12). Repeated annealing of the S-free oxide did not produce H₂O, indicating that the hydroxylated surface was completely consumed via H₂O formation on the first anneal.

To verify that SO₂ formation is not affected by physisorbed H₂O, TPD measurements were carried out on a Fe-S-oxide surface prepared initially by exposure of a clean Fe surface to H₂S at 316 K (no annealing, no cooldown) followed by oxidation at 300 K. SO₂ desorption

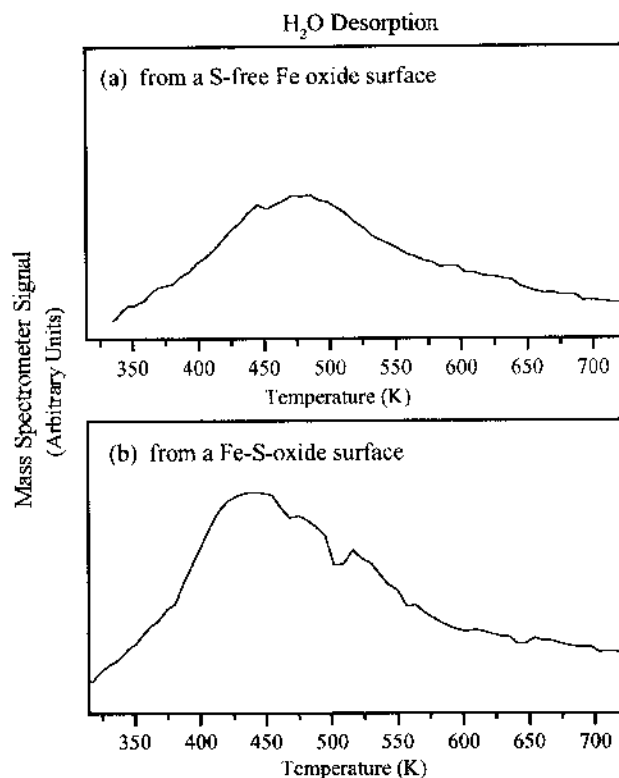


Figure 2.10. TPD spectra of H_2O : **(a)** obtained from a *S-free* Fe oxide prepared by exposure of a clean Fe surface to 900 L of O_2 at 300 K **(b)** obtained from a Fe-S-oxide surface prepared by exposure of a clean Fe surface to 6 L of H_2S at 316 K, followed by exposure to 900 L of O_2 at 300 K. The H_2O desorption in both cases is attributed to a hydroxylated oxide surface.

was still observed during TPD proving that the SO_2 formation is not affected by the presence of physisorbed H_2O on the oxide surface. For comparison, Fig. 2.10b displays the H_2O desorption obtained from the Fe-S-oxide surface whose temperature was maintained at 316 K (no cooldown). A broad H_2O peak was observed similar to the H_2O peak from the S-free oxide (Fig. 2.10a) indicating that they both are due to the hydroxylated oxide surface.

Fig. 2.11 displays data for successive TPD and AES measurements of a sulfided Fe sample initially covered with a thin oxide overlayer. The first TPD cycle performed up to a

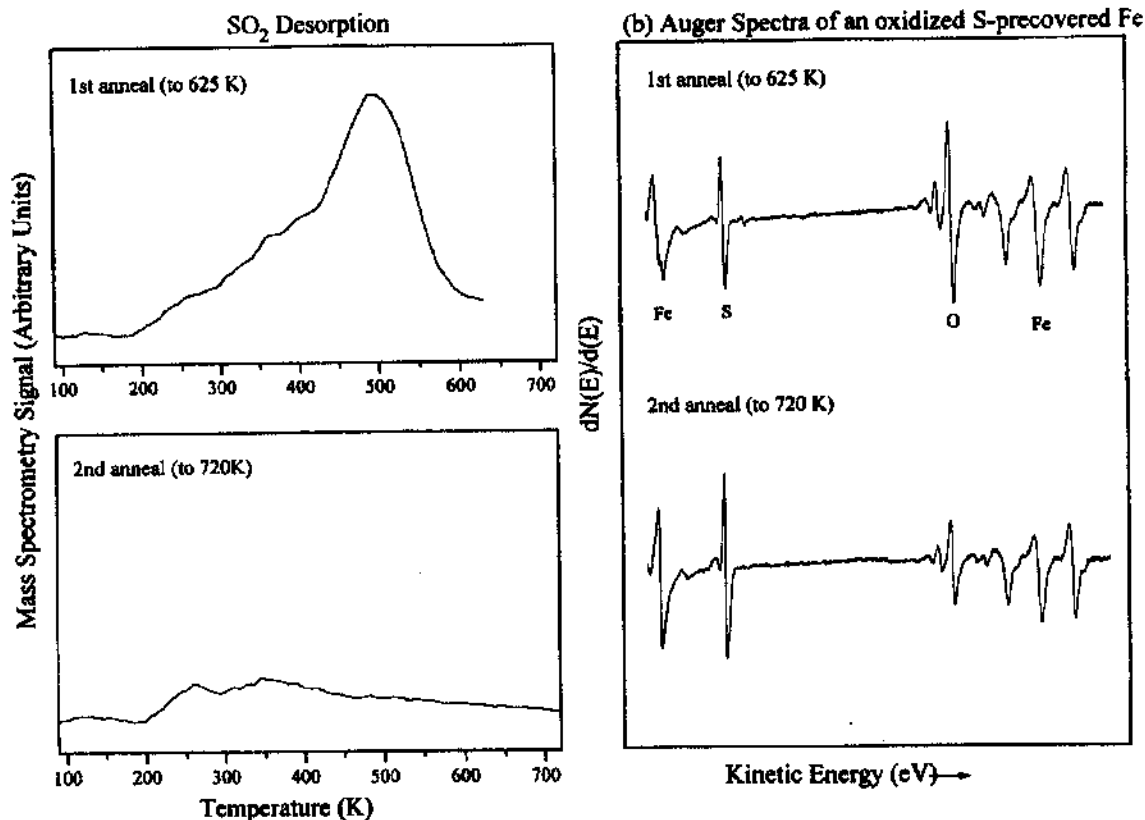


Figure 2.11. TPD and AES data obtained from a Fe-S-oxide surface: (a) SO_2 desorption after first anneal to 625 K (top trace) and repeated anneal to 720 K (bottom trace) (b) corresponding Auger spectra after first anneal (top trace) and second anneal (bottom trace). The sample was prepared by exposure of clean Fe to 6 L of H_2S (85 K, 500 K anneal), followed by 900 L of O_2 at 300 K.

temperature of 625 K, shows that SO_2 desorption started at 250 K and is complete by 620 K.

The corresponding Auger data for the first anneal is presented in Fig. 2.11b. As shown in Fig. 2.11b (top trace), the oxide was not decomposed upon heating to 625 K, evidenced by the presence of the bifurcated Fe(MVV) peak. A second heating of the sample from 85 K to 720 K did not produce SO_2 (Fig. 2.11a, bottom trace) even though initially the sample has an overlayer of thin oxide. However, the anneal to 720 K resulted in the removal of most of the oxide (Fig. 2.11b, bottom trace). This is indicated by the replacement of the bifurcated

Fe(MVV) with the Fe(MVV) single peak and by a decrease in the O(KLL) relative intensity. Thermal cycling of an uncontaminated (S-free) oxide to 720 K did not result in oxide film spallation. The data indicate that the initial SO₂ formation from the Fe-S-oxide surface is breaking interfacial bonds between the oxide and substrate. Further heating or thermal cycling thus results in oxide spallation.

H₂S/S on Fe Oxide

Fig. 2.12a displays the changes in S/O AES peak-to-peak intensity ratios as a function of H₂S exposure on the Fe oxide surface at 85 K, with and without subsequent annealing to 500 K. It is clear from the curves that saturation was achieved quickly for H₂S exposures with no subsequent annealing. However, a slower approach to saturation was observed when dosing is followed by annealing to 500 K. In contrast to the Fe metal, there was no H₂S multilayer formation observed on the oxide surface at 85 K. It is also evident from the data that annealing to 500 K results in a significantly higher saturation coverage. These results suggest that during dosing, S diffuses into the oxide and possibly even to the metal-oxide interface. A subsequent anneal to 500 K causes the S atoms within the oxide to diffuse to the oxide surface. It is possible that annealing to 500 K results in sulfide layer formation on top of the oxide. Fig. 2.12b shows the variations in the dose vs. coverage for H₂S exposures on the oxide at 316 K. A similar trend was observed in that annealing to 500 K also resulted in a higher saturation coverage (Fig. 2.12b). Comparison of the curves in Fig. 2.12a and 2.12b shows a higher saturation coverage for H₂S exposures carried out at 85 K with a 500 K anneal than at 316 K followed by a 500 K anneal. This indicates a higher sticking coefficient of H₂S

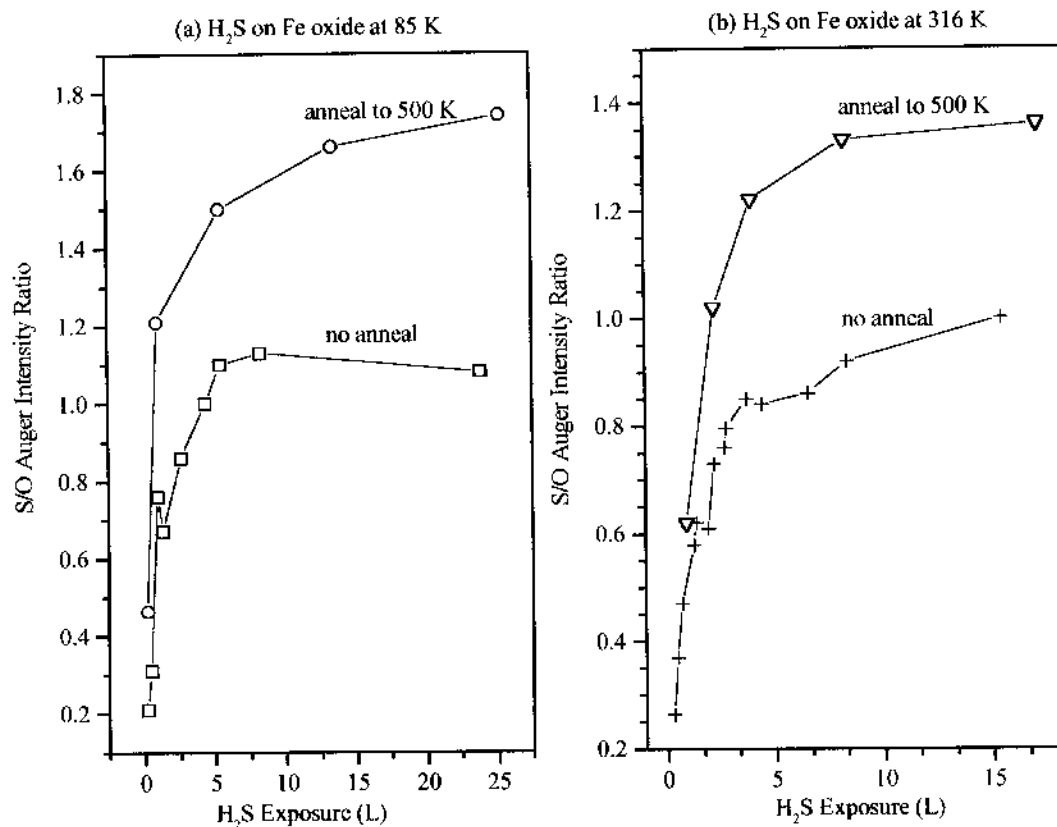


Figure 2.12. Variations in S(LMM)/O(KLL) Auger peak-to-peak intensity ratios as a function of H₂S exposure on a Fe oxide (900 L O₂, 300 K) surface: (a) adsorption at 85 K with and without subsequent annealing to 500 K (b) adsorption at 316 K with and without subsequent annealing to 500 K.

on the oxide surface at lower temperature.

To avoid the complication of H₂O adsorption at low temperatures, TPD measurements on the Fe oxide were carried out at room temperature (no cooldown). Fig. 2.13a shows the TPD spectra obtained from an Fe oxide surface following adsorption of H₂S at 316 K. A fresh oxide - and therefore hydroxylated (Fig. 2.10a) - was prepared prior to each H₂S exposure.

There was no SO₂ desorption observed for a low exposure (Fig. 2.13a). However, at higher exposures (8.3 L, 67 L in the figure), a small amount of SO₂ desorbed from the surface (Fig. 2.13a). The peak is broad, ranging from 340 K to 560 K. This is in contrast to the well-defined SO₂ peak observed from the Fe-S-oxide surface (Fig. 2.7). The SO₂ desorption at high exposures may be due to S that has diffused into the metal-oxide interface. This result indicates that adsorbed S on the oxide does not produce SO₂. No H₂ desorption or any other S-containing product was observed. The corresponding H₂O desorption is displayed in Fig. 2.13b. As shown in the figure, the H₂O yield did not correlate with H₂S exposure indicating that H₂O formation is not associated with H₂S dosing. It would seem that the source of the

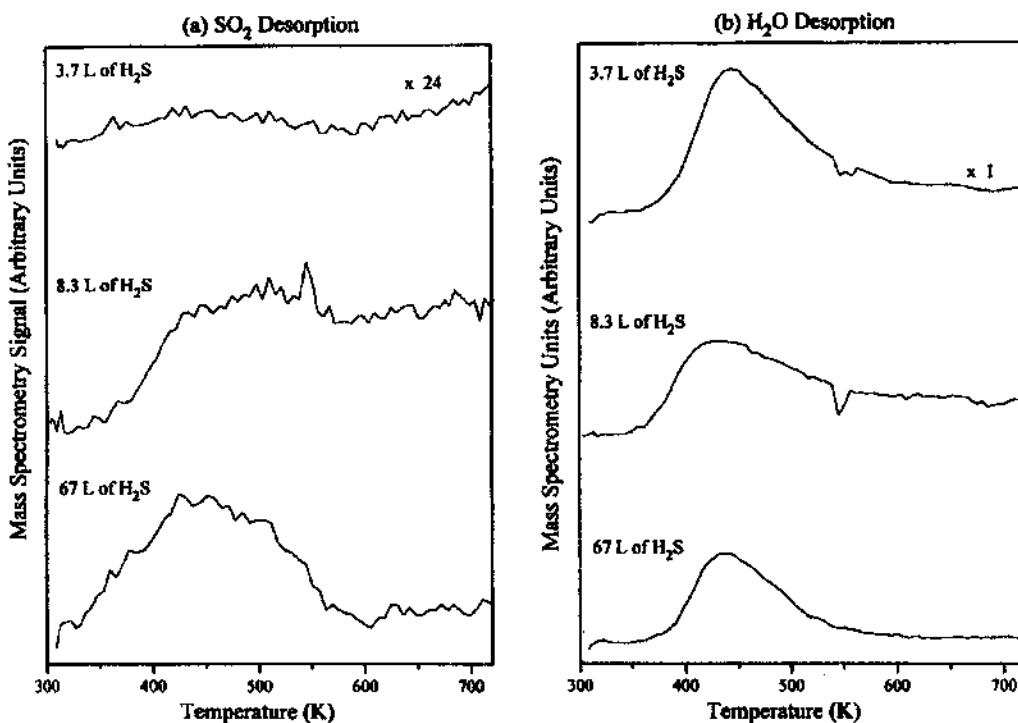


Figure 2.13. (a) TPD profiles of SO₂ obtained from a Fe oxide surface (900 L O₂, 300 K) following adsorption of H₂S at 316 K (no cooldown). SO₂ desorption is observed only at high exposures. (b) Corresponding TPD spectra of the H₂O desorption.

H₂O is simply the hydroxylated oxide surface. However, H₂O formation due to a reaction between H₂S and the oxide (i.e., $\text{H}_2\text{S} + \text{oxide} \rightarrow \text{H}_2\text{O}\uparrow + \text{S}_{(\text{a})}$) is a possibility. To distinguish between H₂O from the oxide itself and the H₂O due to the oxide-H₂S interaction, TPD measurements were carried out on a pre-annealed Fe oxide following adsorption of H₂S at 316 K (no cooldown). Repeated annealing of an uncontaminated (S-free) oxide does not produce H₂O after the first heating cycle. Thus, annealing the oxide at least once eliminates the hydroxylated surface. When the pre-annealed oxide was exposed to H₂S at 316 K, TPD measurements revealed no H₂O desorption. This indicates that no H₂O formation occurs upon adsorption of H₂S on the Fe oxide surface at 316 K. The implication of this result is that the H₂ or H₂O resulting from the H₂S exposure “desorbs” immediately upon H₂S exposure to the Fe oxide surface at 316 K, consistent with previous results (11). Examination of the H₂O data in Fig. 2.13b shows that the H₂O yield did not increase with increasing H₂S exposure thus corroborating this conclusion.

When an Fe oxide surface subsequently exposed to H₂S at 316 K was momentarily annealed to 720 K in UHV, a significant loss of O intensity was evident from Auger measurements. The decrease in O(KLL) signal ranged from 37 %-50 % for the varying S coverages. In contrast, corresponding measurements for the *S-free* oxide revealed that the O loss was only 17 %. The decrease of the O signal in the *S-free* oxide may be attributed to H₂O desorption from the hydroxylated oxide surface. However, the decrease of the O signal in the S-contaminated oxides is significant and indicates an additional mechanism of oxide loss. The variation in % loss (ranging from 37 % - 50 %) vs. H₂S exposure suggests a non-uniform loss

of O across the oxide surface. It can be argued that the decrease of the O signal may be due to attenuation as a result of FeS formation on *top* of the oxide surface. However, after the anneal to 720 K, a corresponding decrease of the S signal (31 % - 38 %) was also observed which may be due to S diffusion into the bulk during the anneal. Since the S signal has decreased, S could not have attenuated the O signal. It is therefore concluded that the decrease in the O signal upon annealing to 720 K is mainly due to S-induced removal of oxygen from the surface region by a mechanism which does not involve SO₂ formation.

Fig. 2.14 shows the Auger spectra of an Fe oxide surface following exposure with H₂S at 316 K before annealing (top trace), after first anneal 720 K (middle trace) and after second anneal to 720 K (bottom trace). As shown in the display, the S(LMM) spectrum consists of a single peak before the anneal. After annealing to 720 K, the appearance of the bifurcated S peak was observed (middle trace). This is accompanied by a substantial reduction of the Fe oxide to metallic Fe as evident from the enhanced peak on the low energy side of the bifurcated Fe(MVV) peak. Subsequent repeated anneal to 720 K (bottom trace) enhanced the bifurcation of the S peak and the reduction of the oxide to metallic Fe. The data suggest that S still causes degradation of the oxide even when S is present not at the metal-oxide interface but rather on the oxide surface. The data also indicate that, in the latter case, SO₂ formation is not a major reaction pathway for the loss of the oxide.

H₂S/S on Fe Oxide in H₂O or O₂ environment

TPD experiments on the Fe oxide with H₂S dosing carried out at low temperature reveal SO₂ desorption (Fig. 2.15a), in contrast to the corresponding experiments at room

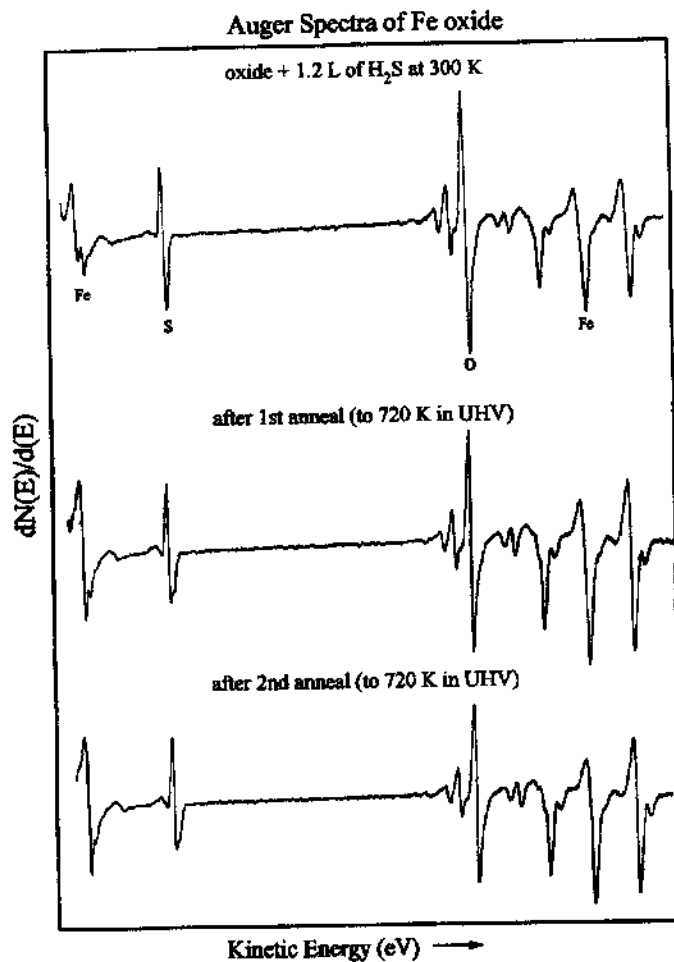


Fig. 2.14. Auger spectra of Fe oxide (900 L O₂, 300 K). **Top trace:** following adsorption of H₂S at 316 K (no cooldown). **Middle trace:** after first anneal of the surface to 720 K in UHV. **Bottom trace:** after second anneal to 720 K in UHV. Note the enhancement of the bifurcated S lineshape upon thermal cycling of the sample.

temperature. This SO₂ formation is attributed to the adsorption of H₂O on the oxide surface upon cooldown to low temperatures.

The TPD spectra of an Fe oxide surface following adsorption of 1.2 L of H₂S at 85 K is displayed in Fig. 2.15a. The desorption has 3 components: a peak at 515 K and a broad

peak from 200 - 420 K and a low temperature peak at 115 K. The data presented here (Fig. 2.15a) is in contrast to the well-defined peak of SO_2 from the Fe-S-oxide surface (Fig. 2.7). Moreover, there is a shift to a higher maximum temperature of desorption (515 K vs. 500 K). No H_2S or H_2 desorption was observed.

The Fe oxide surface was not pre-annealed before exposure to H_2S and was therefore hydroxylated. H_2O desorption was observed (Fig. 2.15a) due to adsorbed H_2O and/or H_2O from the oxide itself (due to hydroxylation). As discussed previously (Fig. 2.13a) there is no

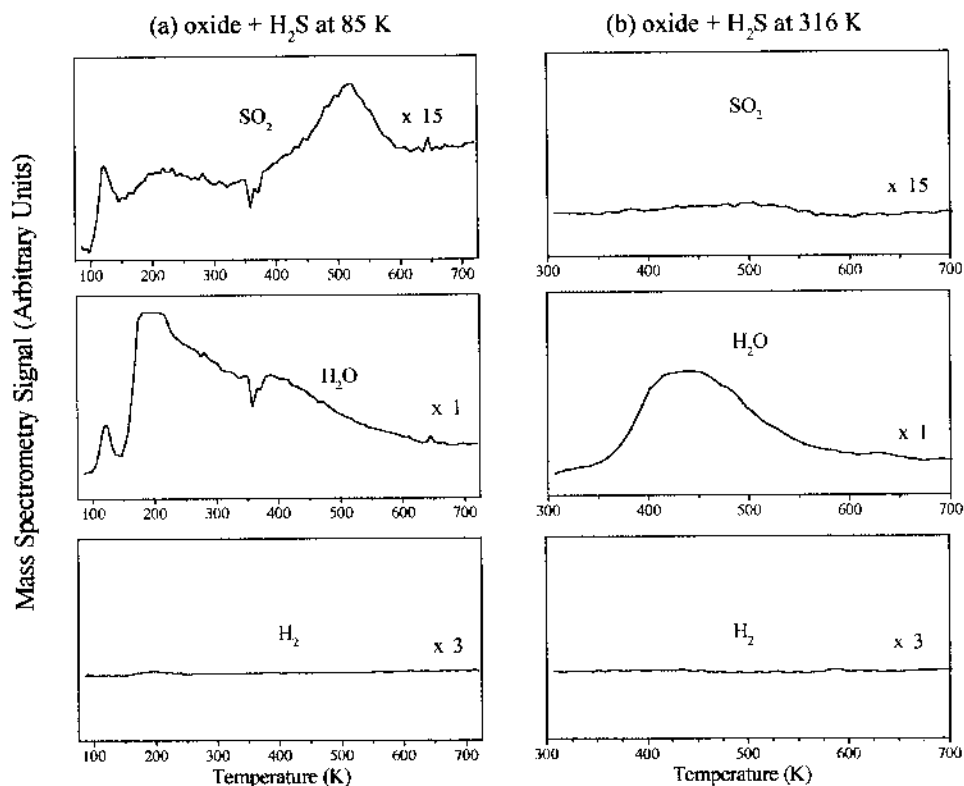


Figure 2.15. TPD spectra obtained from a Fe oxide surface (900 L O_2 , 300 K) following adsorption of 1.2 L of H_2S (a) at 85 K and (b) at 316 K (no cooldown). SO_2 desorption is observed only when H_2S and H_2O are coadsorbed on the oxide surface.

SO₂ desorption observed for the Fe oxide exposed to H₂S at room temperature, in contrast to the TPD results of the Fe oxide surface with coadsorbed H₂S and H₂O. Therefore, the SO₂ formation upon H₂S adsorption at 85 K is due to a reaction between S and H₂O physisorbed on the oxide surface.

This observation is further verified by the TPD data shown in Fig. 2.16a. The measurements were obtained from an Fe oxide following adsorption of 1.2 L of H₂S at 316 K with subsequent cooldown to 85 K to allow for H₂O adsorption from the ambient. The results indicate that the SO₂ yield increases with the waiting time at 85 K (roughly proportional to the amount of adsorbed H₂O at the surface). The data corroborate the previous observation that adsorbed H₂O is reacting with the adsorbed S on the oxide surface.

Additional TPD experiments were performed to confirm the interaction between adsorbed S and H₂O on the oxide surface. In these experiments, H₂S dosing was carried out at 316 K (no cooldown to 85 K) to avoid H₂O physisorption. The TPD measurements (between 316 K to 720 K) were carried out in an overpressure of H₂O (10⁻⁸ Torr) or O₂ (10⁻⁸ Torr). Fig. 2.16b displays the SO₂ desorption data. As shown in the figure, SO₂ desorption occurred in the presence of either H₂O (Fig. 2.16b, bottom trace) or O₂ (Fig. 2.16b, middle trace). The maximum peak is near 515 - 530 K. The data presented here are clear evidence that SO₂ formation on a S-oxide surface occurs only in the presence of H₂O or O₂ vapor. H₂S adsorption at 316 K and reaction with H₂O and O₂ vapor leads to the SO₂ peak at 515 K. Lower temperature features at 200 - 420 K and 115 - 150 K (Fig. 2.16a) were not observed. This indicates that at lower temperatures, SO₂ formation pathways are specifically associated

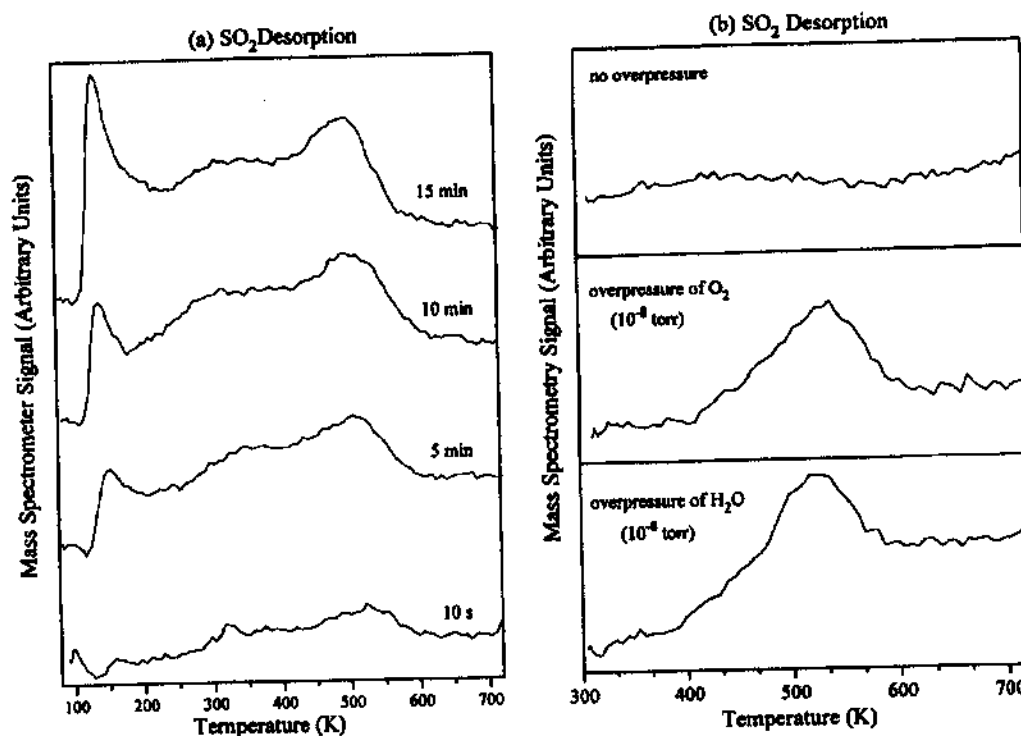


Figure 2.16. (a) TPD profiles of SO₂ obtained from a Fe oxide surface exposed to 1.2 L of H₂S at 316 K with subsequent cooldown to 85 K. The spectra were taken at varying periods of waiting time at 85 K before TPD. The cooldown to 85 K allows the physisorption of H₂O from the chamber ambient. (b) TPD profiles of SO₂ obtained from a Fe oxide surface exposed to 1.2 L of H₂S at 316 K (no cooldown). The measurements were carried out in UHV (top trace), in an overpressure of 10⁻⁸ Torr O₂ (middle trace), and in an overpressure of 10⁻⁸ Torr H₂O (bottom trace).

with reactions between adsorbed species, whereas the 530 K feature can arise from an Eley-Rideal mechanism (Fig. 2.16b).

Discussion

The results presented above demonstrate the varying chemical behavior of H₂S/S adsorbed at a clean Fe(poly) metal surface, at an Fe oxide surface and S at the Fe-oxide interface. These results are summarized schematically in Fig. 2.17. No SO₂ formation occurred between S_(a) on the Fe metal and H₂O or O₂ vapor (Fig. 2.17a). In contrast, S

adsorbed on the Fe oxide surface reacted with either physisorbed H_2O or H_2O or O_2 vapor to form SO_2 (Fig. 2.17b). A similar behavior was observed when H_2O was physisorbed on the S-covered Fe and oxide surfaces: on the Fe metal surface, no SO_2 was formed between co-adsorbed H_2S and H_2O while on the oxide surface SO_2 desorption was observed. For low H_2S exposures on the oxide surface, no SO_2 evolution was observed demonstrating that the oxide does not react with the adsorbed S to form SO_2 . However, SO_2 formation occurred between S and the oxide when S is present at the Fe-oxide *interface* (Fig. 2.17c).

From the thermodynamic point of view, the data reveal some unexpected results. The reaction of *bulk* FeS with O_2 to form SO_2 is favorable ($\Delta G_{500\text{K}} = -207\text{ kJ/mol}$) under the

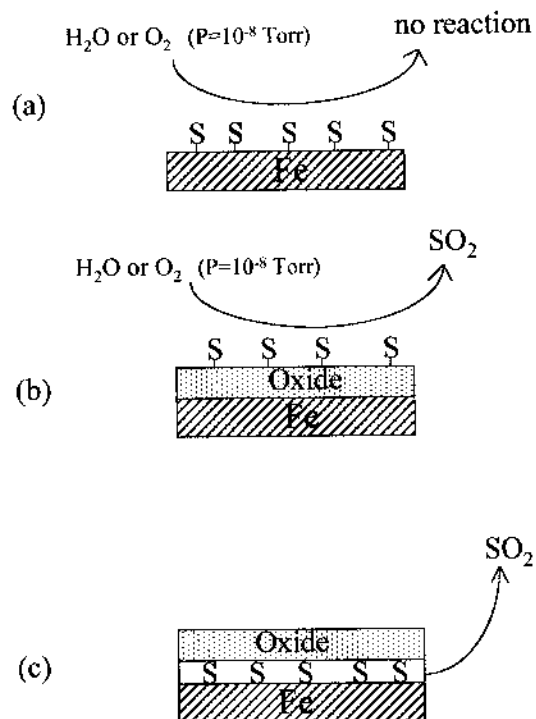


Fig. 2.17. Schematic representation of results.

experimental conditions. The results, however, showed no SO_2 formation for $\text{S}_{(\text{a})}$ on Fe exposed to O_2 . Moreover, the reaction of *bulk* FeS and FeO to form SO_2 is thermodynamically uphill under these conditions ($\Delta G_{500\text{ K}} = +187\text{ kJ/mole}$). In contrast, the data from this study demonstrate the formation of SO_2 at the Fe-S-oxide interface at 500 K. The formation of SO_2 which implies the breaking of Fe-O bonds, is also in disagreement with previous quantum mechanical calculations (21). The apparent contradiction of the results here with simple thermodynamic and more detailed quantum mechanical calculations suggests that the actual bonding environment at the Fe-S surface and at the Fe oxide/sulfide interface is significantly different from bulk sulfides and oxides. Furthermore, while it has been demonstrated that there is significant charge transfer between adsorbed S and free metal surfaces (14), modification of the charge distribution may be occurring at the interface when a thin oxide overlayer is grown on the sulfided metal surface. This is corroborated by the Auger data for S adsorbed on Fe which showed a change from a bifurcated S Auger peak to a single S peak upon formation of a oxide overlayer on the presulfided Fe surface. This change in S lineshape has been interpreted (2) to be due to an increase in the S-S interactions and a consequent decrease of Fe-S interactions.

The chemical behavior of adsorbed S on the Fe metal or on Fe oxide surfaces is in apparent contrast to the chemical behavior observed for adsorbed S on Ni. Previous studies (15, 16) reported SO_2 formation due to a reaction between a sulfided Ni single crystal and gas phase O_2 near ambient temperature. These studies (15, 16) concluded that S adsorbed on the Ni surface is removed via a reaction with O_2 to form SO_2 . Another investigation (3) reported

no SO₂ or very little SO₂ formation upon annealing of an oxidized Ni(111) surface precovered with S, in contrast with the results presented here. That study, however, reported evidence of some SO₂ formation upon annealing of oxidized Ni with S deposited on the oxide surface. Although in the present study the TPD measurements revealed no SO₂ formation between the oxide surface and adsorbed S at low exposures, high exposures of H₂S resulted in the desorption of a small amount of SO₂ (Fig. 2.13a). This may be due to S that has diffused across the thin oxide film to the metal-oxide interface. The variance of the results here with previous investigations (3, 15, 16) may be due to the different chemical behavior of S adsorbed on Ni as compared to S adsorbed on Fe. Another possibility is that SO₂ is formed at the Ni-S-oxide interface, but was not observed due to the relative placement of quadrupole and sample (3). The results here also emphasize the importance of controlling ambient H₂O contamination in order to obtain consistent results.

Even though there was no significant SO₂ formation for S adsorbed on Fe oxide, some oxide destabilization was observed to occur when S is deposited on *top* of the Fe oxide surface. This is evident from the significant oxide loss upon annealing of the S-contaminated Fe oxide sample (Fig. 2.14). The oxide loss observed here is consistent with previous studies (17, 18) of the effect of sulfidizing atmospheres on preformed oxides of Fe-Cr and Fe-Cr-Ni alloys. These previous studies (17, 18) reported failure of the preformed oxides due to external sulfidation and/or internal sulfidation. External sulfidation occurs when base metal ions are transported across the oxide scale to the gas-oxide interface with consequent formation of an external metal sulfide (17, 18). In contrast, internal sulfidation occurs when S penetrates into the metal-

oxide interface via gaseous transport or solid-state diffusion of S across the oxide layer (17, 18). A study on Ni (111) (3) also reported some oxide instability due to adsorbed S on the oxide surface. In that study (3), some SO₂ formation was observed and was suggested as a possible cause for the oxide instability. However, the data here demonstrate no such SO₂ formation between the oxide surface and adsorbed S except at high exposures (Fig. 2.13a). The SO₂ formed upon higher exposures is presumably due to S diffusion into the metal-oxide interface. The results here therefore indicate that SO₂ formation is not a major reaction pathway for the loss of oxide. The data revealed by the TPD and Auger measurements are more consistent with solid state diffusion of S across the oxide *during* the anneal to 720 K and subsequent oxide instability due to metal sulfide layer formation at the metal-oxide interface. The appearance of a bifurcated S peak upon annealing is in agreement with this premise since a bifurcated S denotes a stronger Fe-S interactions (2). It is interesting to note, however, that when a S-covered oxide was annealed up to 500 K, Auger measurements did not reveal any bifurcation of the S peak. Furthermore, the anneal to 500 K resulted in a higher S saturation coverage compared to the unannealed S-covered oxide surfaces (Fig. 2.12). These results are consistent with a sulfide layer formation on top of the oxide surface.

The data further show that adsorption of H₂S on the Fe metal surface at 316 K is dissociative since no H₂S desorption was observed (Fig. 2.4b). No H₂ desorption was observed suggesting that H₂ was “desorbed” during dosing of H₂S at 316 K. These results are in agreement with previous studies conducted on other transition metals (11, 19). In contrast, H₂S adsorption on the Fe metal surface at 80 K results in H₂S multilayer formation for

exposures of 6L H₂S or greater (Fig. 2.2a). The TPD measurements revealed that desorption of the multilayer occurs at 110 K, identical to the multilayer desorption temperature of H₂S on other transition metals (8, 19). Decomposition of the H₂S_(a) starts at temperatures above 100 K as indicated by H₂ desorption (Fig. 2.4a). This is also in agreement with previous XPS results (20).

In contrast to the Fe metal, no multilayer formation of H₂S (for exposures of 25 L or less) on the Fe oxide surface was observed at 85 K (Fig. 2.12a). This variance on multilayer formation in clean Fe and oxide surfaces seems surprising considering the very low temperature (85 K) of adsorption. These results demonstrate that even at 85 K the nature of the adsorption site (metal vs. oxide) exerts a significant influence on multilayer formation. There are two phenomena that may explain this difference. One is significant diffusion of S species into the oxide during H₂S dosing. A second possibility is that the site geometry for H₂S adsorption on the oxide results in a more scattered H₂S layer on the oxide surface. Either of these factors could result to a lower packing density of adsorbed H₂S on the oxide in comparison to adsorbed H₂S on the clean Fe and consequently on the formation or non-formation of multilayer H₂S. Previous XPS results (20) have shown that adsorption of H₂S on Fe oxide at 110 K results in SH_(a) and S_(a) formation, in corroboration of our data. The decomposition of the H₂S on the oxide surface at low temperature is also consistent with the observation of low temperature SO₂ peaks (Fig. 2.15a, 2.16a) upon reaction of the H₂S/oxide surface with physisorbed H₂O or H₂O vapor. These low temperature SO₂ peaks were never observed upon annealing of the Fe-S-oxide surface (Fig. 2.7). Annealing of an Fe oxide surface exposed to

H₂S at 85 K did not produce any H₂ evolution (Fig. 2.15a). This suggests that there is no cleavage of the SH_(a) or OH_(a) bonds to form H_(a) which can then combine to form H₂. It is possible that extensive H-bonding occurs between the H of SH_(a) and the O of OH_(a) thus preventing the release of H atoms.

The H₂O evolution observed after adsorption of H₂S on the oxide at low temperature is due in part to the inevitable H₂O adsorption from the ambient. Although a low temperature interaction between H₂S and the oxide to form H₂O is a possibility, no such interaction was observed when H₂S was adsorbed on the oxide surface at 316 K. The H₂O data was further complicated by the presence of an initially hydroxylated surface, also a source of the H₂O desorption (Fig.2.10a). The hydroxylation of the oxide surface cannot be due to H₂O impurity from the O₂. No H₂O impurity was detected by the mass spectrometer upon repeated checking of the O₂ gas used in these experiments. Therefore, hydroxylation is attributable to H₂O (and possibly H₂ also) from the chamber ambient which was trapped in the oxide lattice during growth of oxide at 300 K.

The dependence of the S(LMM) peak lineshape variations on H₂S dosing conditions and coverage are in accord with the conclusions from previous studies (2, 8). The results presented suggest that the bifurcated S peak is not associated with a change from a molecular species (H₂S or SH) to adsorbed S in agreement previous work (8). The appearance of a single peak upon exposure at 85 K as opposed to a bifurcated S peak at 316 K suggests that S clusters are formed at low temperature (2). S clustering is further supported by the observation of the appearance of a S single peak only upon high H₂S exposures on the Fe surface at 316 K.

The change of the S bifurcated peak to a single peak upon exposure to O₂ has been reported before (2). In that study (2), the change in S lineshape was interpreted as being due to the formation of S clusters upon formation of a thin oxide on top of a S-precovered Fe(111). It was proposed that the formation of oxide overlayer causes the S atoms underneath the oxide to coalesce resulting in stronger S-S interactions with consequent weakening of Fe-S interactions (2). The results show that upon annealing of the Fe-S-oxide surface, a slight bifurcation of the S single peak was observed, in agreement with the previous study (2). Destruction of the oxide by annealing to 720 K results in stronger Fe-S interactions resulting in the appearance of the S bifurcated peak (2). It can be deduced that the bifurcation of the S peak is not associated with S-O bond formation.

Summary and Conclusions

In summary, TPD and AES studies were carried out to investigate the interactions of H₂S/S adsorbed on an oxidized Fe(poly) with H₂O or O₂ as well as the interactions of H₂S/S adsorbed on a Fe(poly) metal surface with H₂O or O₂. On the clean Fe(poly) surface, the following interactions were revealed by the line-of-sight TPD measurements:

- (a) $\text{Fe} + \text{H}_2\text{S}_{(a)} + \text{H}_2\text{O}_{(a)} \rightarrow \text{no SO}_2 \text{ formation (85 K - 720 K)}$
- (b) $\text{Fe} + \text{S}_{(a)} + \text{H}_2\text{O}_{(g)} \text{ or } \text{O}_{2(g)} \rightarrow \text{no SO}_2 \text{ formation (85 K - 720 K)}$
- (c) $\text{Fe} + \text{H}_2\text{S} \text{ at } 80 \text{ K} \rightarrow \text{multilayer formation (exposures of 6 L or greater)}$
- (d) $\text{Fe} + \text{H}_2\text{S} \text{ at } 316 \text{ K} \rightarrow \text{dissociative adsorption (no H}_2 \text{ desorption; H}_2 \text{ "desorbs" during H}_2\text{S dosing)}$

On the Fe oxide surface, the following interactions were revealed:

(e) oxide + S_(a) → no SO₂ formation

(f) oxide + S_(a) + H₂O_(g) or O_{2(g)} → SO₂ formation (515 K - 530 K)

(g) oxide + H₂S_(a) + H₂O_(a) → SO₂ formation (115 - 150 K, 200 - 420 K, 515 K)

(h) oxide + H₂S at 85 K → no multilayer formation (for exposures of 24 L or less)

On the metal-oxide interface, the following reaction occurs:

Fe + interfacial S + oxide overlayer → SO₂ formation (500 K)

The results presented demonstrate that the initial adsorption site of S (metal vs. oxide) is important in determining reaction pathways. Our results suggest that the initial oxidation state of S at the Fe-oxide interface and at the oxide surface are different. The data shown here indicate that only S adsorbed on the metal surface reacts *with the oxide* to form SO₂. Therefore, only S that is truly at the Fe-oxide interface can induce oxide-metal bond scission. The results of this study has direct implications in the area of corrosion. The effect of S is most destructive when present at the metal-oxide interface. The segregation of internal S impurities to the metal-oxide causes destabilization with consequent lift-off of the protective oxide via SO₂ formation. In addition, there is evidence of some oxide degradation due to S adsorbed on the oxide surface. SO₂ formation between oxide and S is not the oxide loss mechanism in this case. The destabilization maybe due to solid state diffusion of adsorbed S close to or at the vicinity of the metal-oxide interface with subsequent formation of internal sulfides. A detailed explanation of the oxide destabilization due to S adsorbed on the oxide surface could not be established from this study.

Chapter References

- (1) Seo, M.; Sato, M.; Lumsden, J. B.; Staehle, R. W. *Corrosion Science*. **1977**, *17*, 209.
- (2) Arabczyk, W.; Baumann, T.; Mussig, H.-J.; Storbeck, F. *Vacuum* **1990**, *41*, 79.
- (3) Liu, J.; Lu, J. P.; Chu, P. W.; Blakely, J. M. *Journal of Vacuum Science and Technology. A* **1992**, *10(4)*, 2355.
- (4) Feldman, L.C.; Mayer, J.W. *Fundamentals of Surface and Thin Film Analysis*; PTR Prentice Hall, New Jersey, 1986; p. 127.
- (5) Arabczyk, W.; Narkiewicz, U.; Kalucki, K.; Freidenberg, E. *Applied Surface Science*. **1993**, *72*, 45.
- (6) Murray, E.; Kelber, J.A. *Journal of Vacuum Science and Technology. A* **1995**, *13(5)*, 2558.
- (7) Koestner, R. J.; Salmeron, M.; Kollin, E. B.; Gland, J. L. *Surface Science*. **1986**, *172*, 668.
- (8) Huntley, D. R. *Surface Science*. **1990**, *240*, 13.
- (9) Murray, E.; Prasad, J.; Cabibil, H.; Kelber, J. A. *Surface Science*. **1994**, *319*, 1.
- (10) Thiel, P. A.; Madey, T. E. *Surface Science Reports*. **1987**, *7*, 211.
- (11) Hardegree, F. L.; Ho, P.; White, J. M. *Surface Science*. **1986**, *165*, 488.
- (12) Hung, W.-H.; Schwartz, J.; Bernasek, S.L. *Surface Science*. **1993**, *294*, 21.
- (13) Chase, M. W., et al., *JANAF Thermochemical Tables*; American Chemical Society, Washington DC, 1986.
- (14) Oudar, J. *Material Science Engineering*. **1980**, *42*, 101.
- (15) Holloway, P. H.; Hudson, J. B. *Surface Science*. **1972**, *33*, 56.
- (16) Windawi, H.; Katzer, J. R. *Journal of Vacuum Science and Technology*. **1979**, *16(2)*, 497.

- (17) Baxter, D. J.; Natesan, K. *Oxidation of Metals*. **1989**, 31(3/4), 305.
- (18) Lobnig, R. E.; Grabke, H. J. *Corrosion Science*. **1990**, 30(10), 1045.
- (19) Hedge, R.I.; White, J.M. *Journal of Physical Chemistry*. **1986**, 90, 296.
- (20) Prasad, J.; Murray, E.; Kelber, J.A. *Chemical Physics Letters*. **1992**, 190(3/4), 187.
- (21) Hong, S. Y.; Anderson, A. B., *Physical Review B*. **1988**, 38(14), 9417.

CHAPTER 3

XPS STUDIES: EFFECTS OF SULFUR ON Fe AND Cr OXIDE THERMAL STABILITY IN 304 STAINLESS STEEL

Introduction

This section discusses X-ray photoelectron spectroscopy (XPS) studies of a Fe-Cr-Ni alloy exposed to H₂S and O₂ under ultra-high vacuum (UHV) conditions. Results indicate that the presence of S at the predominantly Fe metal surface prior to oxidation inhibited surface oxidation at temperatures between 325 K and 825 K. The presence of adsorbed S did not, however, inhibit the surface segregation of Cr for temperatures > 600 K, compared to a S-free sample. Upon annealing of a pre-sulfided, oxidized sample to 900 K in UHV, the Fe oxide largely disappears, while no change is observed in the Cr oxide. The results presented here will show that sulfidation of an alloy metal surface prior to oxidation and surface segregation can adversely affect the thermal stability of the Fe oxide without affecting the Cr oxide overlayer resulting from surface segregation and preferential oxidation.

Experimental

The experiments reported here were carried out in a stainless steel turbomolecularly pumped UHV system (schematically shown in Fig. 3.1) with a base pressure after bakeout

of 5×10^{-10} Torr. The system was equipped with XPS capability, an ion sputter gun for sample cleaning, and a quadrupole mass analyzer for residual gas analysis. Unmonochromatized $AlK\alpha$ radiation from a dual anode x-ray source was used to excite photoelectron spectra. Data were acquired using a commercial hemispherical analyzer operated in the constant pass energy mode. All data were acquired with the analyzer take-off angle perpendicular to the sample surface. The polycrystalline stainless steel foil sample was mounted on Ta leads and the temperature was controlled by a combination of resistive heating and liquid nitrogen cooling. Sample temperature was monitored by a chromel-alumel thermocouple spotwelded to the back of the sample. XPS data were analyzed with a commercial software (1) for non-linear curve fitting. Quantitative analyses of spectral intensities and lineshapes were carried out by fitting experimental spectra to synthetic spectra composed of Voigt functions (2). Relative

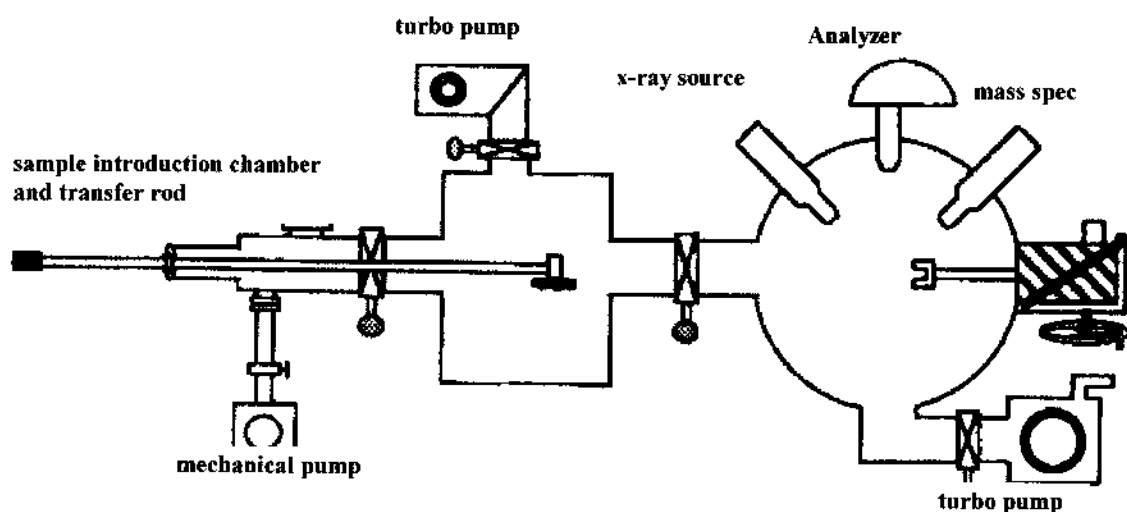


Figure 3.1. Schematic of the XPS System.

atomic concentrations were derived from relative core-level intensities according to:

$$(i) N_a/N_b = (I_a/I_b) * (A_b/A_a)$$

where N_a is the atomic concentration of species a, I_a is the core level signal intensity, and A_a is the atomic sensitivity factor (3). Atomic sensitivity factors used here have been published and include correction terms for the transmission function of the analyzer and changes in the source volume with kinetic energy (3). The use of equation (i) assumes a homogeneous distribution of species within the sampling region. Obviously, such is not always the case. Eqn. (i) was used to determine changes in relative concentration of Fe, Cr or Ni within the sampling region. For cases where (i) is obviously inappropriate, particularly in estimating adsorbate concentrations, (i) was modified by taking into account mean free path corrections (4) (*vide infra*).

Gases were admitted into the UHV chamber via separate stainless steel doser tubes and manual leak valves. The gas exposures are reported here in terms of background pressure x time of exposure (1 Langmuir {L}=10⁻⁶ Torr-sec) and have not been corrected for the effects of directional dosing or flux to the sample. Background pressures in the UHV chamber were measured by a nude ion gauge calibrated for dinitrogen. The ion gauge was mounted out of direct line-of-sight to the sample surface in order to minimize electron-induced decomposition. Gases used were obtained from commercial sources (O₂ 99.997 %, H₂S 99.5 %) and used without further purification.

The stainless steel sample was cleaned in UHV by a combination of Ar⁺ sputtering (2.5 KeV) and thermal annealing to 900 K. This procedure was continued until S, N and other impurities were no longer observed to segregate to the surface during the annealing cycle.

During the course of these studies, the sputter-cleaned sample was repeatedly checked for the possible segregation of internal S to the metal surface during annealing. No such impurity segregation was observed. This procedure ensured that the only S present at or near the metal/oxide interface was that introduced by deliberate exposure to H₂S.

The bulk composition of the sample, as reported by the vendor (5), is compared in Table 3.1 to surface composition obtained by XPS analysis.

Table 3.1: Analysis of the stainless steel (304) sample used in this experiment

<i>Element</i>	<i>Bulk composition (in weight %) as reported by the vendor (ESPI)</i>	<i>Surface composition as determined by XPS after repeated sputtering and annealing</i>
Fe	69.64	54.074
Cr	18.11	20.047
Ni	9.67	25.879
S	0.002 (20 weight ppm)	–
others	balance	–

The results in Table 3.1 indicate that the sample surface is considerably enriched in Ni relative to the nominal bulk composition. The surface composition shown in Table 3.1 was readily reproduced by sputtering and annealing, with relative Fe, Cr and Ni atomic percentages varying by 0.1 % or less. A small amount of residual oxygen was observed for clean samples in XPS, probably due to readsorption of residual contaminant gases. The atomic ratio of oxygen to metal atoms within the XPS sampling region was < 0.016. Assuming an escape depth of all

metal core electrons of approximately 30 Å (4), a rough estimate of 17 % of the metal XPS signals originate from the first layer. On an oxygen/metal atom basis, the total oxygen coverage is estimated as < 9.0 atomic %.

In order to determine the effects of contaminant S on oxidation of 304 stainless steel, three samples were studied: (a) a clean sample exposed only to O₂ with no S contamination; (b) a clean sample exposed to 150 L H₂S followed by a 500 K anneal ("high dose", *vide infra*); and (c) a sample exposed to 0.05 L H₂S at 318 K with no anneal - the "low dose" sample. This procedure permitted comparison between the stability of Fe and Cr oxides formed by oxidation of a clean, predominantly Fe surface with oxides formed on a similar surface covered with a monolayer (high dose) and partial monolayer (low dose) of adsorbed S.

The oxidation process was the same for all samples. Samples were exposed to 60 L of O₂ (1×10^{-7} Torr, 600 s) at 325 K, 425 K, 525 K, 625 K, 725 K and 825 K. After each oxygen exposure, the sample was allowed to cool to 120 K. XPS data were acquired during or after cooldown to 120 K. Samples were subsequently annealed momentarily to 900 K in UHV. XPS spectra were again acquired during or immediately after cooldown. Energy calibration of the spectrometer was achieved by comparing the observed Fe(2p), Cr(2p) and Ni(2p) binding energies to published values (3).

Results

Clean Sample/No S exposure

Fig. 3.2 contains Fe, Cr and Ni core level spectra before O₂ exposure and after exposure for the clean alloy surface at 325 K, 625 K and 825 K. Both Fe and Cr display new

features at higher binding energies relative to the main peak after the 325 K exposure, indicating that both Fe and Cr oxidation have begun near room temperature (Fig. 3.2a, b). There is no significant change in the Ni (2p) spectrum lineshape or binding energies (Fig. 3.2c). This indicates that Ni is not oxidized under these conditions.

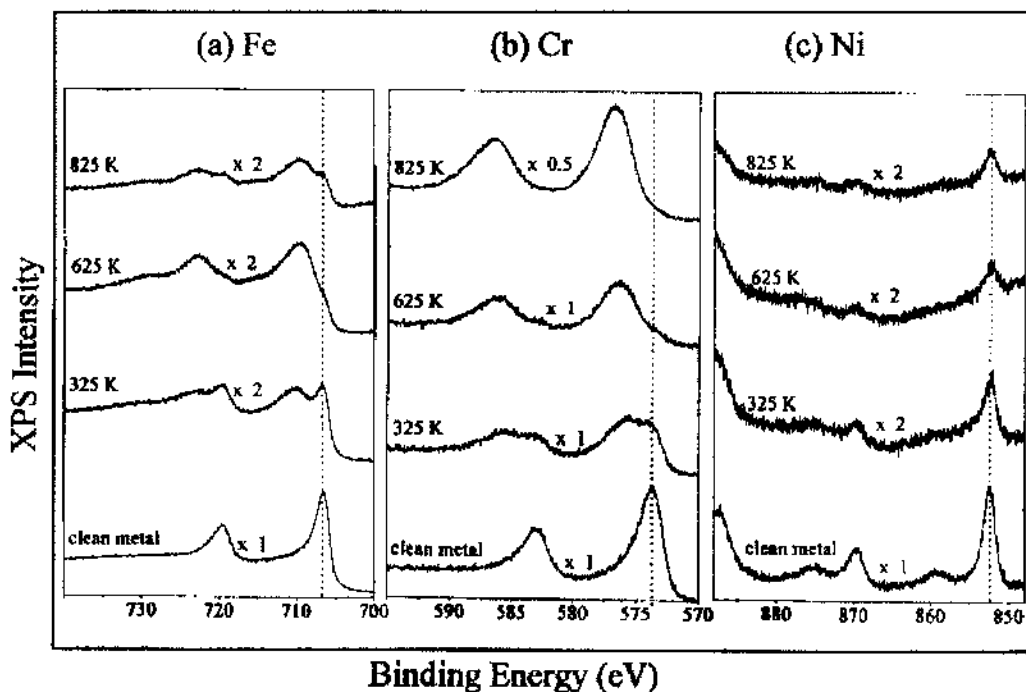


Figure 3.2. XPS spectra of Fe (2p), Cr (2p) and Ni (2p) for a clean 304 stainless steel surface before and after successive 60 L O₂ exposures (10^{-7} Torr, 600 s) from 325 - 825 K. Only spectra from oxidation at 325 K, 625 K and 825 K are shown.

The relative concentrations of each component element as a function of oxidation temperature are displayed in Fig. 3.3. The data (Fig. 3.3) indicate that the segregation of Cr to the surface region occurs above 600 K, coinciding with a relative decrease in the intensity of the Fe and Ni signals. The segregation of Cr above 625 K in the presence of oxygen is

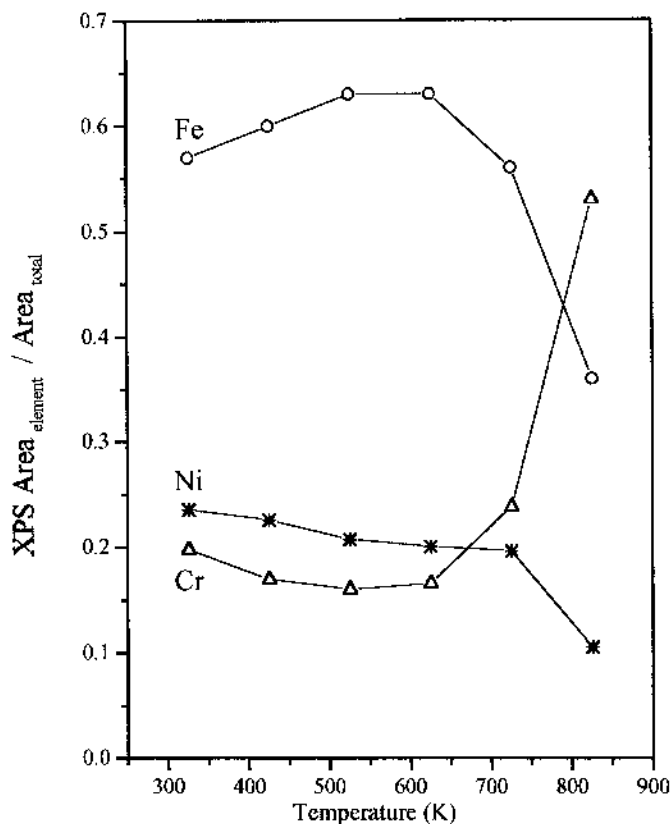


Figure 3.3 Variations in the relative Fe, Cr and Ni XPS intensities for a clean 304 stainless steel sample as a function of oxidation temperature. The sample was dosed successively with 60 L O₂ exposure (10⁻⁷ Torr, 600 s) from 325 - 825 K.

consistent with results of a previous study (6) on Fe-Cr single crystal surfaces. By 825 K, the concentration of Cr on the surface has increased drastically (Fig. 3.3). The onset of Cr oxidation is evidenced by the appearance of a feature at 575.8 eV (Fig. 3.2) after exposure to O₂ at 325 K. By 825 K the binding energy has shifted to 576.6 eV, evidence of Cr₂O₃ formation (3, 7). The onset of Fe oxidation is marked by the appearance of a feature at 709.2 eV (Fig. 3.2) after oxidation at 325 K. In contrast to the Cr XPS spectrum, there is no change

in the binding energy of the Fe oxide feature upon further oxidation. The intensity of the oxide peak, however, does increase relative to that of the metal (Fig. 3.2). The observed 709.2 eV binding energy oxide peak is in good agreement with published values (3, 7) for FeO (709.2-709.3 eV), and significantly different from the binding energy values reported for Fe₂O₃ formation (3, 7) (710.7-710.9 eV). Although the broad nature of the Fe (2p_{3/2}) signal makes precise identification of oxide composition problematic, it is significant that the binding energy of the Cr oxide gradually changes toward that of the stoichiometric oxide (Cr₂O₃, 576.6 eV), while the Fe oxide shows no evidence of Fe₂O₃ formation. This indicates that the latter stages of oxidation involve principally if not entirely the oxidation of the Cr component of the alloy.

Samples Exposed to H₂S

Exposure of a clean sample surface to 0.05 L of H₂S at 318 K yields a single feature in the S(2p) spectrum at 161.1 eV (Fig. 3.4a). This is consistent with the value obtained for S_a on pure Fe (8, 9). At 150 L exposure (Fig. 3.4b), a broader S(2p) spectrum is apparent, indicating the presence of both SH_a (near 164 eV) as well as S_a. The appearance of SH_a only upon high exposures, and the conversion of SH_a to S_a upon annealing has been reported for Fe (8, 9) surfaces. Annealing to 500 K yields the single peak feature indicative of S_a (Fig. 3.4c). It is apparent that the chemical behavior of H₂S on the unoxidized 304 stainless steel surface is similar to that observed on unalloyed transition metal surfaces.

The variation in relative S coverage determined as the ratio between the S(2p) XPS intensity and the total intensities of the Fe, Cr and Ni(2p) signals, is shown in Fig. 3.5 for exposure of the clean surface to H₂S at 318 K. It is apparent that saturation coverage is

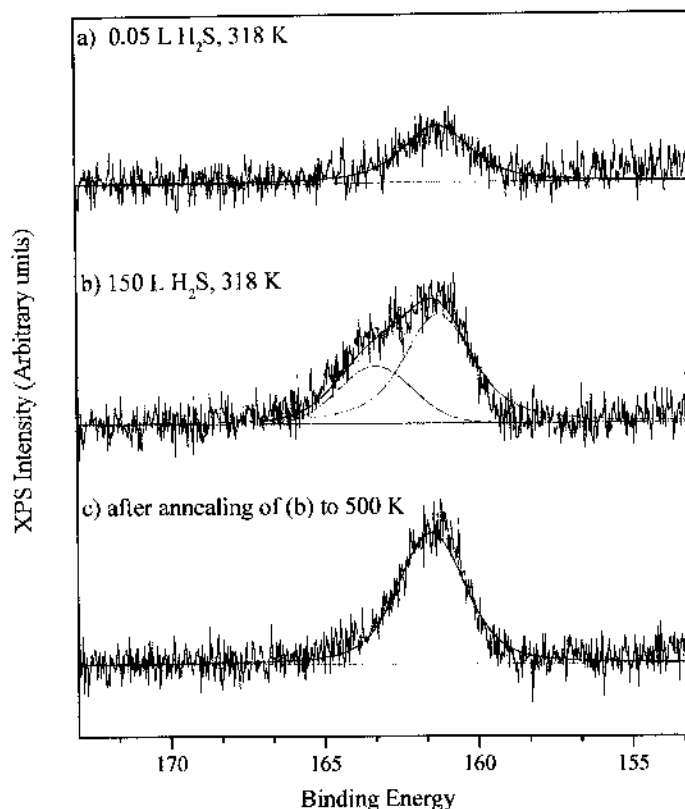


Figure 3.4. XPS spectra of S(2p) obtained following the adsorption of H₂S at 318 K on a clean 304 stainless steel sample. (a) low H₂S coverage (0.5 L) showing one S(2p) peak at 161.1 eV due to S_a (b) high H₂S coverage (150 L) showing 2 peaks at 161.1 eV due to S_a and at 163.1 eV due to SH_a (c) after subsequent anneal of (b) to 500 K.

approached quickly and is complete near 2.0 L exposure. In order to determine the effects of variations in S coverage on subsequent oxidation behavior, a "high dose" sample was prepared by exposure to 150 L H₂S at 318 K followed by annealing to 500 K in UHV. This resulted in the presence of S_a only (Fig. 3.4b, c) at the surface prior to oxidation. The 500 K anneal did not alter the alloy characteristic composition at the surface, and yielded a S/(Fe + Cr + Ni) intensity ratio of 0.012 corresponding to saturation coverage (Fig. 3.5). The S/metal atomic

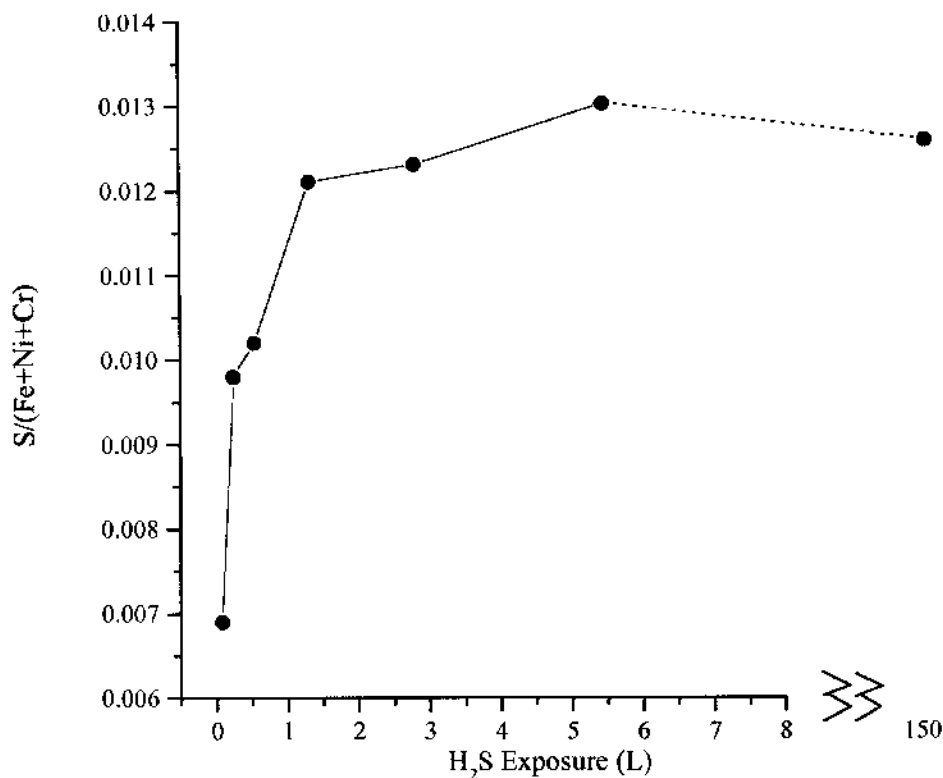


Figure 3.5. XPS peak intensity ratio (S/Fe + Cr + Ni) as a function of H₂S exposures at 318 K. The data have not been corrected for atomic sensitivity factors.

ratio at saturation coverage can be roughly estimated by again assuming (as for contaminant oxygen) that all the sulfur is at the surface, and that approximately 17 % of the total metal signal comes from the first layer of the substrate (see above). This procedure yields a S/metal atom atomic ratio of 0.82 for saturation coverage. A "low" dose sample was prepared by exposing a clean metal to 0.05 L H₂S at 318 K, well below saturation coverage. Using the same estimation method, the S/metal atomic ratio for the low dose sample is 0.25 or 25 atomic % of saturation coverage.

The oxidation behavior of the "high" dose sample is displayed in Fig. 3.6. The data show that the presence of a sulfur-saturated surface strongly retards the formation of Fe and Cr oxide (Fig 3.6a, b) at temperatures above 300 K. There is no significant Fe oxide formation until 825 K (Fig. 3.6a). This is in contrast to the behavior of the S-free sample where oxidation occurs readily near room temperature (Fig. 3.2a, b). As a result of this retardation, the relative amount of the Fe oxide formed in the S-contaminated "high" dose sample is significantly less than the oxide formed from the S-free sample. It is interesting to note that the binding energy of the Fe oxide formed here (708.6 eV) is slightly different from that of the Fe oxide formed on the S-free sample (709.2 eV). This suggests that the oxide formed on a presulfided Fe surface is chemically different from the oxide formed on a S-free sample (708.6 eV vs. 709.2 eV). It is

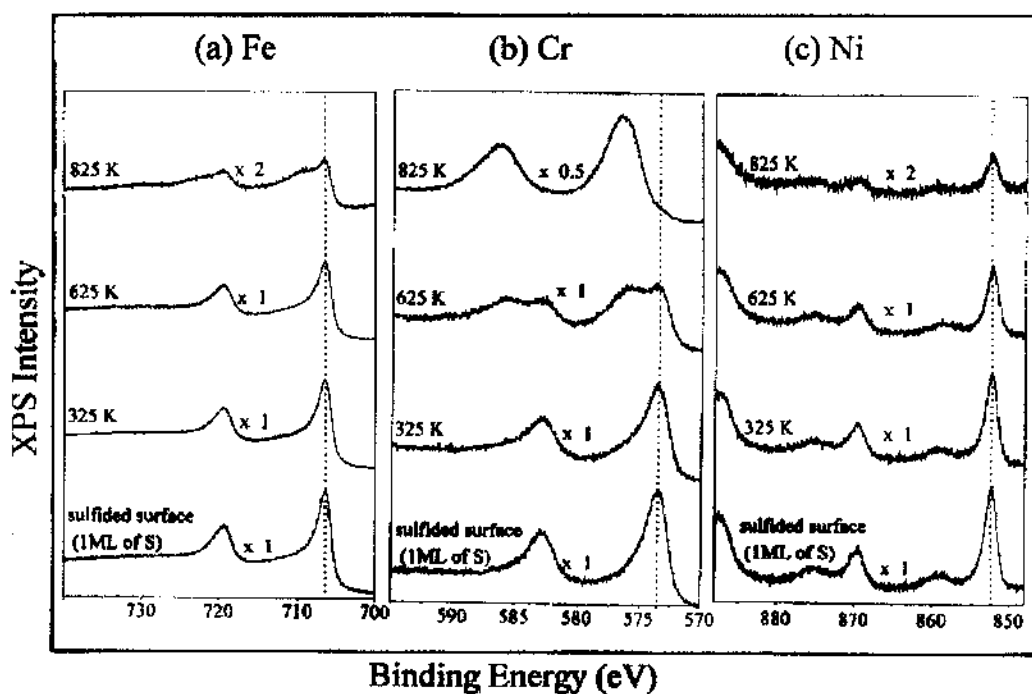


Figure 3.6. XPS spectra of Fe (2p), Cr (2p) and Ni (2p) for a sulfided (1 ML) 304 stainless steel surface before and after successive 60 L O₂ exposures (10⁻⁷ Torr, 600 s) from 325 - 825 K. Only spectra taken from oxidation at 325 K, 625 K and 825 K are shown.

a possibility that the peak at 708.62 eV could actually be FeS₂ or a mixture of both FeS₂ and FeO. However, examination of the data in Fig. 3.6 (bottom trace) reveal that upon adsorption of 1 ML of S coverage (no O₂ exposure) the only Fe peak apparent is that of Fe⁰ (706.8 eV). The observation of only Fe⁰ in the presence of high S surface coverage is consistent with work function measurements on S/Ni(100) (10) which indicated negligible charge transfer between adsorbed S and a transition metal surface. The peak at 708.6 eV grows only upon O₂ exposure and therefore must be assigned to an oxide phase rather than a sulfide phase.

The data in Fig. 3.6b show that the growth of Cr oxide (576.2 eV) does not occur significantly until 625 K. This is consistent with the temperature at which the Cr atoms start to become mobile (6). At 825 K, the binding energy of the Cr oxide peak has shifted to 576.6 eV indicating the formation of Cr₂O₃ (3, 7). For Ni, no new peaks nor any change in binding energies were observed.

Fig. 3.7 shows the relative amounts of each component element (Fe or Cr or Ni)/(Fe + Cr + Ni) as a function of oxidation temperature for the "high" dose sample. Similar to Fig. 3.3, attenuation of both Fe and Ni signals occur at temperatures greater than 625 K indicating that the presence of S has no significant effect on Cr segregation.

Oxidation data obtained from the "low" dose sample (less than a monolayer of H₂S) is shown in Fig. 3.8. Fe, Cr and Ni core level spectra are displayed before O₂ exposure and after oxidation at 325 K, 625 K and 825 K. Not surprisingly, the growth of the Fe and Cr oxide is retarded but to a lesser extent compared to the "high" dose sample. After exposure at 325 K, new peaks with higher binding energies appear for both Cr and Fe (Fig. 3.8). The new Cr peak

at 575.8 eV gradually grows in intensity and shifted to 576.6 eV at 825 K at which point the metallic Cr (2p) has disappeared completely. The new Fe peak (709.2 eV) does not change in binding energy even at higher temperatures. The amount of Fe oxide formed at 825 K approximates that of the oxide formed from the S-free sample. Again, the Ni signal is attenuated at higher temperatures but no change in binding energy is observed. Overall, the oxidation behavior of "low" dose sample is intermediate between that of the S-free sample and "high" dose sample. This observation indicates that S and O compete for the active sites

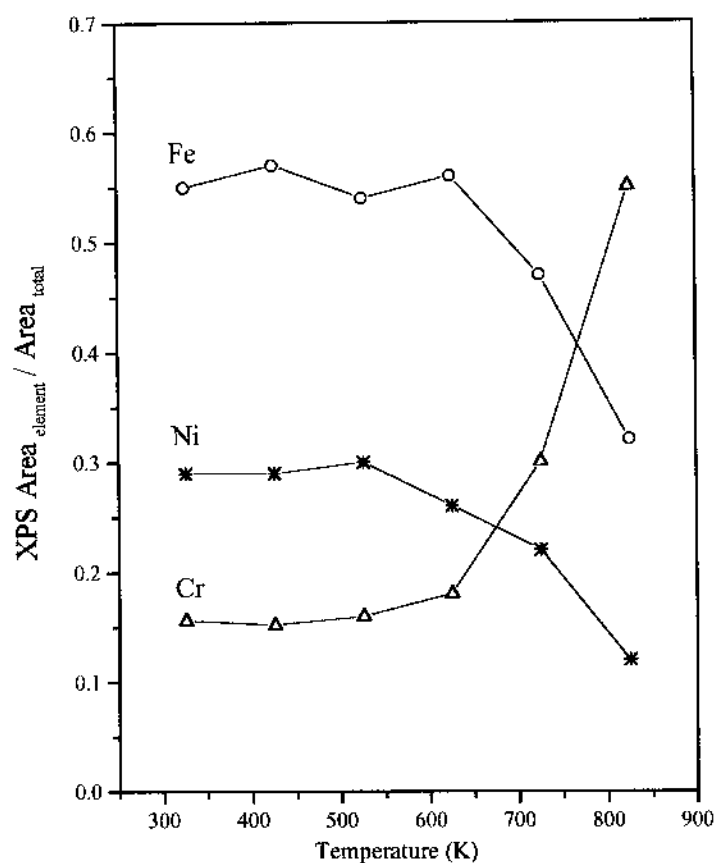


Figure 3.7. Variations in Fe, Cr and Ni XPS intensities for a sulfided (1 ML) 304 stainless steel as a function of oxidation temperature. The sample was successively dosed with 60 L O₂ exposures (10⁻⁷ Torr, 600 s) from 325 - 825 K.

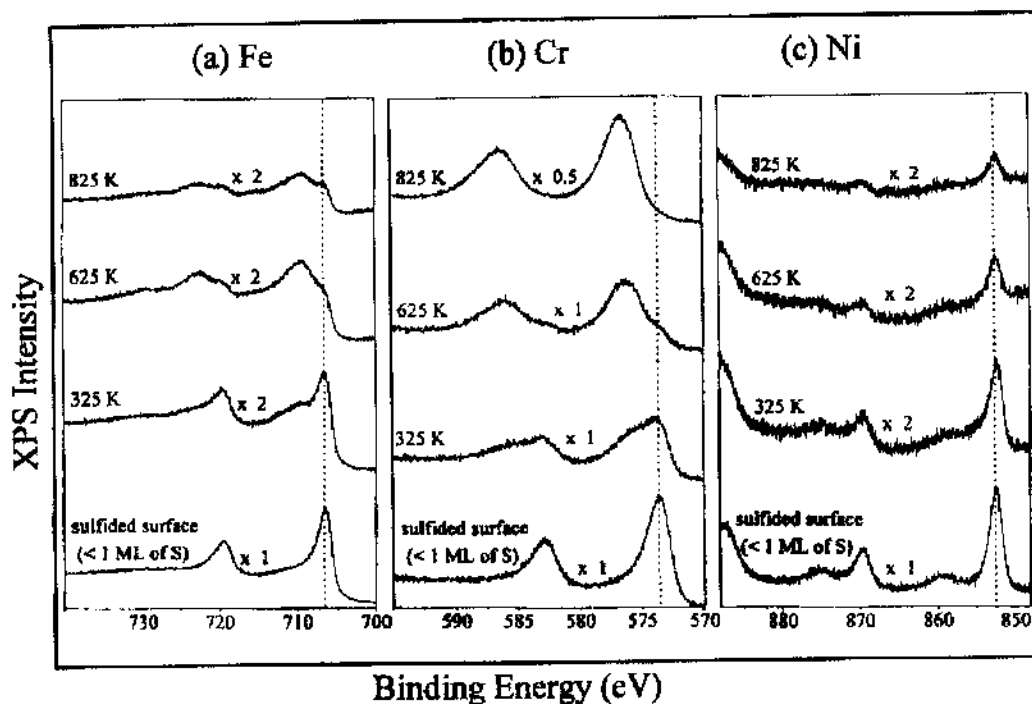


Figure 3.8. XPS spectra of Fe (2p), Cr (2p) and Ni (2p) for a sulfided (less than 1 ML) 304 stainless steel surface before and after successive 60 L O₂ exposures (10⁻⁷ Torr, 600 s) from 325 - 825 K. Only spectra taken from oxidation at 325 K, 625 K and 825 K are shown.

on the alloy surface, consistent with results observed for pure Fe single crystal surfaces (11).

Table 3.2 gives a summary of the binding energies of the observed peaks in this study as compared to the published values in the literature (3, 12).

Oxidized samples annealed momentarily to 900 K in UHV

Fig. 3.9 shows the Fe spectra before and after momentarily annealing the oxidized samples to 900 K in UHV. This procedure was accomplished by ramping the sample temperature from 120 K to 900 K. The temperature ramp is completed in approximately 1.5 minutes. As soon as 900 K was reached, the temperature ramp was stopped and the sample was allowed to cool down back to 120 K.

Table 3.2: A Comparison of the Binding Energies (eV) obtained from the present study and published values from the literature

A. S-free sample

Element/ Compound	Present study ($2p_{3/2}$)	Published values ($2p_{3/2}$)
Cr	573.8	574.1
CrO ₂	575.8 - 576.0 (appeared at 325 K)	576.1, 576.3 [*]
Cr ₂ O ₃	576.6 (observed at T>625 K)	576.6, 576.6 [*]
Fe	706.7	706.75
FeO	709.2 (appeared at 325 K)	709.3 , 710.2, 709.3 [*]
Ni	852.4	852.3

B. Sulfided sample (1 ML of S)

Element/ Compound	Present study ($2p_{3/2}$)	Published values ($2p_{3/2}$)
Cr	573.8	574.1
CrO ₂	576.0 (appeared only at T> 600 K)	576.1, 576.3 [*]
Cr ₂ O ₃	576.6 (appeared only at 825 K)	576.6
Fe	706.7	706.75
FeO	708.62 (appeared only at 825 K)	709.2, 710.2, 709.3 [*]
Ni	852.4	852.3

All published values were taken from the Handbook of X-ray Photoelectron Spectroscopy (3) except values marked with an asterisk (taken from the NIST XPS Database (12)).

Thermodynamic considerations (13) predict that both FeO and Cr₂O₃ should be stable upon annealing to 900 K. Brief annealing of the oxidized control sample (no sulfur) to 900 K in UHV (Fig. 3.9a) shows that only slight changes in the Fe(2p_{3/2}) spectrum occur upon annealing. No observable changes occur in the corresponding Cr(2p_{3/2}) spectrum. It is apparent that in the absence of contaminant S there is no significant thermal instability of Fe oxide or Cr oxide under these conditions.

Fig. 3.9b shows the Fe spectra for the oxidized "low" dose sample before and after momentarily annealing to 900 K in UHV. A considerable amount of the Fe oxide (2p_{3/2}) is reduced to the metallic Fe (2p_{3/2}) state (Fig. 3.9b). A comparison of Fig. 3.9a (S-free sample)

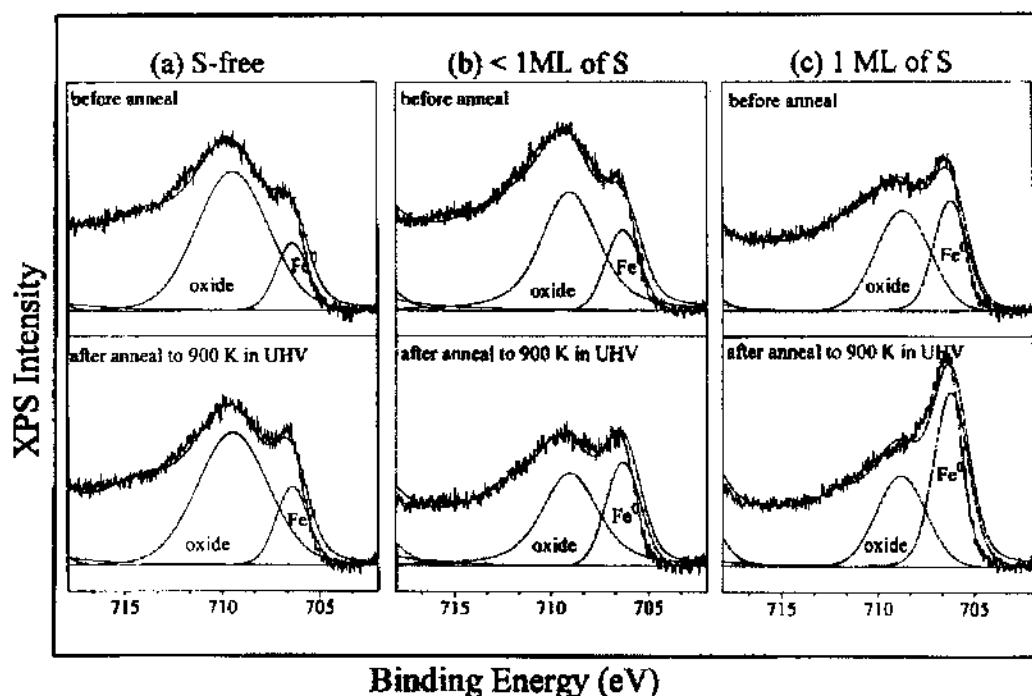


Figure 3.9. XPS spectra of Fe(2p_{3/2}) of an oxidized 304 stainless steel before and after momentary annealing to 900 K in UHV. (a) S-free sample (b) sample is predosed with less than a monolayer of S (c) sample is predosed with 1 monolayer of S. For simplicity, we did not attempt to deconvolute the Fe²⁺ and Fe³⁺ components of the oxide peak.

and Fig. 3.9b ("low" dose sample) suggests that some thermal instability occurs even with less than a monolayer of contaminant S. The corresponding Cr spectra did not exhibit any change.

The Fe oxide formed on the "high" dose sample (Fig. 3.9c) is significantly less than the Fe oxide formed on either the control sample or the "low" dose sample. This is due to the retarding effect of the adsorbed S on the oxidation of the sample. Annealing of the oxidized sample momentarily to 900 K results in the significant reduction of the Fe oxide to metallic Fe. Again, there is no significant change in the corresponding Cr (2p) spectrum.

Discussion

The data presented above demonstrate that S, when present at the predominantly Fe metal surface prior to oxidation and Cr surface segregation, subsequently results in the destabilization of the Fe oxide while leaving the Cr oxide unaffected. The data also demonstrate that S significantly retards the oxidation of the metal surface while not greatly affecting the surface segregation process as a function of temperature. The fact that adsorbed S retards oxidation is not surprising. This effect has been observed for the Fe(111) surface (11), as well as for a variety of Fe alloys (14, 15). It is apparent that S and O compete for the same initial adsorption site at the Fe (and presumably Cr) metal surface (11). It has been observed (14, 15) that formation of Fe or Cr sulfides hinders passivation in aggressive environments. The results reported above indicate that Fe oxide films formed in the presence of adsorbed S are chemically different than those formed in the absence of S. The detailed relationship between oxide structure and passivating qualities clearly warrants further study.

The observed instability of the Fe oxide compared to the Cr is consistent with most S

being initially adsorbed at Fe sites and remaining at Fe sites during subsequent heating and oxidation. As Fig. 3.3 indicates, at temperatures below 600 K, Fe is the primary elemental component in the XPS sampling region. Oxidation of Fe-Cr alloys at room temperature produces an oxide film which is primarily a mixed valence (Fe^{+3} , Fe^{+2}) oxide at the surface (with composition dependent on oxygen overpressure), with a chrome oxide layer underneath (6). The chrome oxide overlayer which forms at temperatures above 600 K (Fig. 3.3, 3.7) then forms over an Fe oxide layer. The instability of the Fe oxide on the sulfided samples (Figs. 3.9b, c) may occur only at patches of Fe oxide not covered by the more stable Cr oxide. Alternatively, destruction of the Fe oxide may result in additional oxidation of partially oxidized Cr beneath the surface region. In any event, it is apparent that decomposition of the Fe oxide does not affect the overlying Cr oxide layer.

Summary and Conclusions

The XPS data presented here demonstrate that interfacial S does result in oxide instability in an Fe-Cr-Ni alloy (304 stainless steel). Sulfidation of the predominantly Fe surface prior to oxidation from 325 K to 825 K results in the disappearance of the Fe oxide upon annealing to 900 K in UHV. No change upon annealing is observed for the Cr oxide. The presence of S at the surface prior to oxidation inhibits both Fe and Cr oxidation but does not significantly affect Cr segregation to the surface at elevated temperatures. The data demonstrate that sulfidation of (primarily) one alloy component may result in the thermal instability of the oxide of that component without affecting the oxides of other elements within the surface film of the alloy.

Chapter References

- (1) "Peak Fit" V 3.0, copyright 1991, AISN Software.
- (2) Voight functions are convolutions of Lorentzian and Gaussian functions. See Puerta, J.; Martin, P. *Applied Optics*. 1991, 20, 3923.
- (3) Wagner, C. D.; Riggs, W. M.; Davis, L. E.; Moulder, J. F.; Muilenberg, G. E. (eds.) *Handbook of X-ray Photoelectron Spectroscopy*; Physical Electronics-Division of Perkin-Elmer Corp., Eden Prairie, MN, 1979.
- (4) Briggs, D.; Seah, M. P. (ed) *Practical Surface Analysis: Volume I; Auger and X-ray Photoelectron Spectroscopy (second edition)*; J. Wiley and Sons, New York; 1990; p. 201.
- (5) Electronic Space Products International (ESPI). 1050 Benson Way, Ashland, OR 97520.
- (6) Leygraf, C.; Hultquist, G.; Ekelund, S. *Surface Science*. 1974, 46, 157.
- (7) Palacio, C.; Mathieu, J. J.; Stambouli, V.; Landolt, D. *Surface Science*. 1993, 295, 251.
- (8) Prasad, J.; Murray, E.; Kelber, J. A. *Surface Science*. 1993, 289, 10.
- (9) Prasad, J.; Murray, E.; Kelber, J. A. *Chemical Physics Letters*. 1992, 190, 187.
- (10) Hardegree, E. L.; Ho, P.; White, J. M. *Surface Science*. 1986, 165, 488.
- (11) Arabczyk, W.; Narkiewicz, U.; Kalucki, K.; Freidenberg, E. *Applied Surface Science*. 1993, 72, 45.
- (12) NIST XPS Database.
- (13) Jones, D. A. *Principles and Prevention of Corrosion*; MacMillan Publishing Company, New York, New York, 1992; p. 410.
- (14) Baxter, D. J.; Natesan, K. *Oxidation of Metals*. 1989, 31, 305.
- (15) Lobnig, R. E.; Grabke, H. J. *Corrosion Science*. 1990, 30, 1045.

CHAPTER 4

UHV-STM, LEED AND AES STUDIES:

SULFUR EFFECTS ON Fe(111)

Introduction

The effects of segregated S to the single crystal Fe(111) surface are relatively unexplored. A few previous studies (1-4) have used electron spectroscopy methods and have therefore not been able to elucidate real-space structural information on the S-modified Fe(111) surface. This present study has made use of a UHV-STM in combination with LEED and AES techniques to investigate the effects of segregated S on the topography and O₂ reactivity of the Fe(111) surface.

The (111) orientation of Fe, a bcc metal, is the most open surface of the low-Miller index Fe surfaces (5). As such, the Fe(111) possesses the highest surface free energy (6) and is expected to be morphologically unstable. LEED spectra analysis (7, 8) revealed multilayer relaxation of the first 4 atomic layers of the Fe(111) surface showing a contraction-contraction-expansion-contraction sequence. Previous LEED studies (1-4) on the interactions between Fe(111) and S observed the formation of a (1×1)-S overlayer. This is the only structure reported for the segregation of S to Fe(111). It was observed that S forms ordered adlayers on other Fe single crystal surfaces: a c(2×2) on the Fe(100) surface (9) and a p(2×2) on the Fe(110) surface (10). S has been known to induce reconstructions on single crystal transition

metal surfaces (6, 11-18). These reconstructions typically involve changes in the lateral and vertical atomic arrangements of the first few atomic layers of the substrate metal. S has also been observed to cause more drastic structural changes on certain metal surfaces (19, 20). Previous LEED and STM studies (19) on S/Mo(100) interactions have reported changes in the step structures varying from multi-height steps, double steps and monatomic steps depending on S coverage. LEED measurements revealed that adsorption of S on the open W(111) surface resulted in a completely faceted surface (20).

In this chapter, atomic resolution STM images of S overlayers and faceting transformations on the Fe(111) surface are presented along with previously unobserved LEED structures of S on Fe(111).

Experimental

The experiments were performed in a UHV system (base pressure $< 7.5 \times 10^{-11}$ Torr) shown schematically in Fig. 4.1. It consists of a scanning tunneling microscope and a sample analysis chamber. The sample analysis chamber is equipped with an Omicron four-grid LEED optics, a cylindrical mirror analyzer (CMA) from Physical Electronics for AES, and a UTI-100C quadrupole mass spectrometer for residual gas analysis. A 12-inch travel high precision manipulator allows translation of the sample along three dimensions as well as rotation around the manipulator axis. The system is equipped with an ion sputter gun for sample cleaning through Ar ion bombardment. The STM chamber is attached to the sample analysis chamber (Fig. 4.1). The whole chamber is evacuated by a Varian ion pump and a titanium sublimation pump (TSP). The sample was introduced from air into the UHV chamber via a magnetic linear

feedthrough. Sample transfer from the analysis chamber to the STM chamber was accomplished with the use of a wobble-stick.

The Fe(111) used in the experiments was obtained commercially with degree of purity at 99.94 %. The sample has a diameter of 9.6 mm and a thickness of 1 mm. The misalignment of the crystal from the (111) orientation is less than 1° . The S content as determined by the vendor (21) is 250 ppm. The sample was spotwelded onto a molybdenum plate that could be transferred between the manipulator and STM stage. The sample could be heated by indirect resistive heating. A K-type Cr-Al thermocouple was attached to a sample clip approximately 5

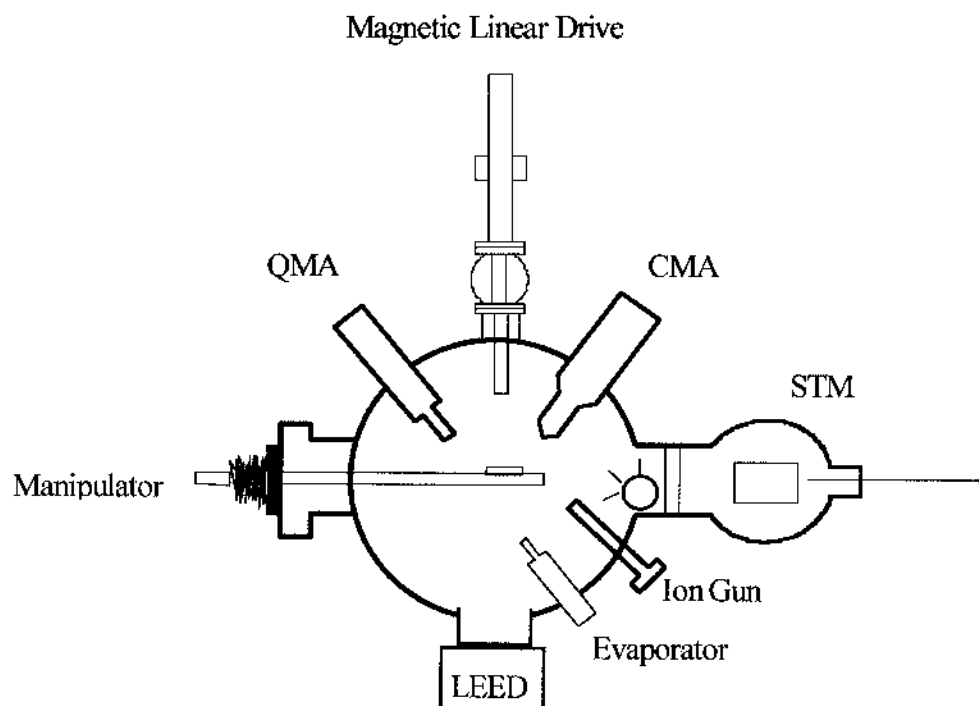


Figure 4.1. The ultra-high vacuum (UHV) system used in this study. The system is equipped with STM, LEED, AES and mass spectrometry capabilities.

mm away from the sample. The difference between the actual temperature and thermocouple reading was not calibrated.

The Fe(111) crystal was cleaned by Ar⁺ sputtering and subsequently annealed to elevated temperatures (473 K - 950 K) at various annealing times to generate the desired S coverage on the Fe(111) surface as indicated by AES. As the S content in the bulk was gradually depleted after several cleaning cycles, higher temperatures and longer annealing times were necessary to achieve the same S coverage. For oxygen reactivity studies, a 99.997 % O₂ gas was used which was obtained commercially and introduced into the chamber by a manual leak valve without further purification. Sample exposure to O₂ was carried out by backfilling the chamber at partial pressures between 10⁻⁸ Torr to 10⁻⁶ Torr. Gas exposures are reported here in terms of Langmuir (L) (1 L = 10⁻⁶ Torr.s). Pressures were measured with a nude ion gauge calibrated for dinitrogen. Exposures have not been calibrated for sensitivity or flux to the sample. AES measurements were obtained in the integral (N(E)/E) mode using a coaxial 2 KeV electron excitation source. Differentiation to obtain the dN(E)/dE spectra was carried out by computer. S coverages were measured by the peak-to-peak heights of the S(LMM) transition (152 eV) vs. the Fe(LMM) signal (651 eV). Similarly, O coverages of the S-precovered Fe(111) surface was determined by measuring the peak-to-peak heights of O(KLL) transition (503 eV) vs. Fe(LMM) transition (651 eV).

The surface ordering was checked by LEED and STM. STM measurements were performed in the constant current mode at room temperature. The images were recorded with typical sample bias voltages (V_t) between 10 to 100 mV and tunneling currents (I_t) between 1

to 3 nA. The tip was made by electrochemical etching of a polycrystalline tungsten wire (0.01 inch diameter). Most of the images shown in this publication have been processed to reduce linear background in the x and y directions of the plane and remove high frequency spatial noise.

Results

The LEED and STM results are presented in the order of increasing S coverage. The “clean” Fe(111) surface is presented first which contains low coverages (up to 20 atomic %) of S, N and/or O according to Auger measurements. The determination of Auger at. % concentrations has been corrected for sensitivity factors and assumes that the trace impurities were uniformly distributed within the AES sampling depth. The (1×1)-S phase is presented next which is associated with one “geometric” ML of S (*vide infra*). This structure was obtained by further annealing of the “clean” Fe(111) crystal resulting in the segregation of S and a transformation of the low S coverage phase to a (1×1)-S pattern. By driving additional S to the surface (annealing temperatures: ~ 775 - 950 K) a transformation to a new $(2\sqrt{3}\times 1)R30^\circ$ -S LEED pattern was observed associated with more than one “geometric” ML coverage of S. The reactivity with O₂ of the S-precovered Fe(111) surfaces was also investigated. The oxidation experiments were carried out at room temperature.

“Clean” Fe(111): trace impurities of S, N and O (“clock” structure)

Fig. 4.2a displays the complex LEED pattern obtained for a well-annealed “clean” Fe(111) surface. This LEED pattern was consistently observed for the Fe(111) surface containing trace impurities of S, N and O (Fig. 4.2b) (conc. from 0 to 20 at. %). The dominant

(a)



(b)

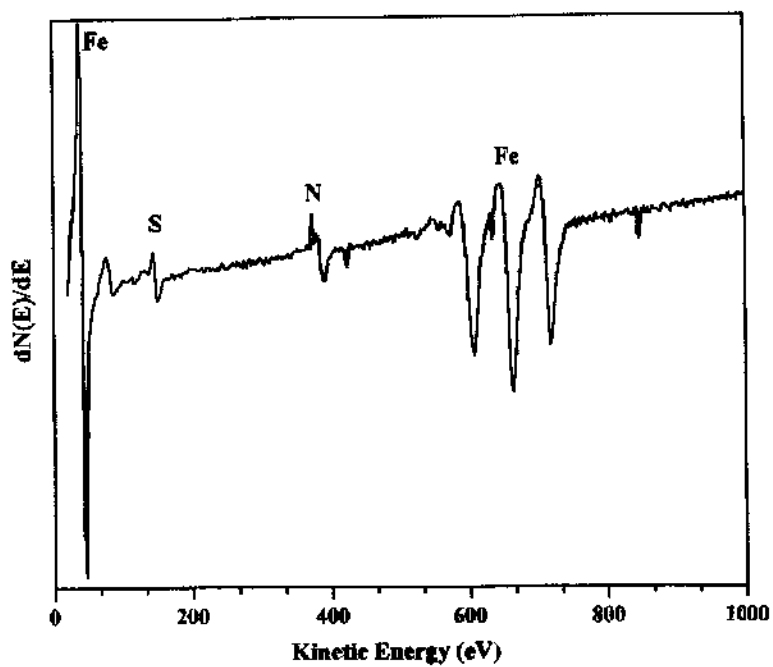


Figure 4.2. (a) “Clock” LEED pattern obtained from a less-than-clean Fe(111) surface. Beam energy = 47 eV. (b) A typical Auger spectrum corresponding to the “clock” structure showing low coverages of S, N and O.

features of the pattern are groups of spots that form rings around the first order diffraction spots of the Fe(111). Each of these rings look like a “clock” and so therefore, this phase is referred to as the “clock” surface throughout the remainder of the text. This LEED pattern (Fig. 4.2a) appeared only after annealing the sputtered-clean crystal to temperatures above 530 K but below temperatures at which significant S segregation occurs (typically 775 K). LEED measurements of a freshly-sputtered (unannealed) Fe(111) surface show a diffuse (1×1) pattern reflective of the Fe(111) bulk lattice geometry. Annealing of this sputtered-clean sample up to 475 K shows only the (1×1) pattern even when trace impurities of S, O and N are present on the surface. Previous LEED studies (1) on clean Fe(111) did not observed the complex “clock” LEED pattern shown here. Only the (1×1) pattern of the bulk Fe(111) was reported (1) despite of the fact that in these previous studies the crystal was annealed to temperatures (~575 K) above the typical annealing temperatures used here in the present study. The variance of these results maybe related to the presence of trace electronegative impurities on the Fe(111) surface (Fig. 4.2b).

Fig. 4.3a displays a typical atomic resolution STM image of the "clock" surface. A pseudo-quadratic symmetry is revealed which does not reflect the three-fold rotational symmetry of the original bcc Fe(111). The unit cell distances are significantly large, $\sim 8 \text{ \AA} \times \sim 7 \text{ \AA}$. The identity of the observed protrusions cannot be established from the STM and AES data. Attempts to correlate the complex “clock” LEED pattern and the atomically resolved image for the “clock” surface have been unsuccessful. Fig. 4.3b displays a typical large scan area (400 nm × 400 nm) STM image of the “clock” surface. The image shows a faceted

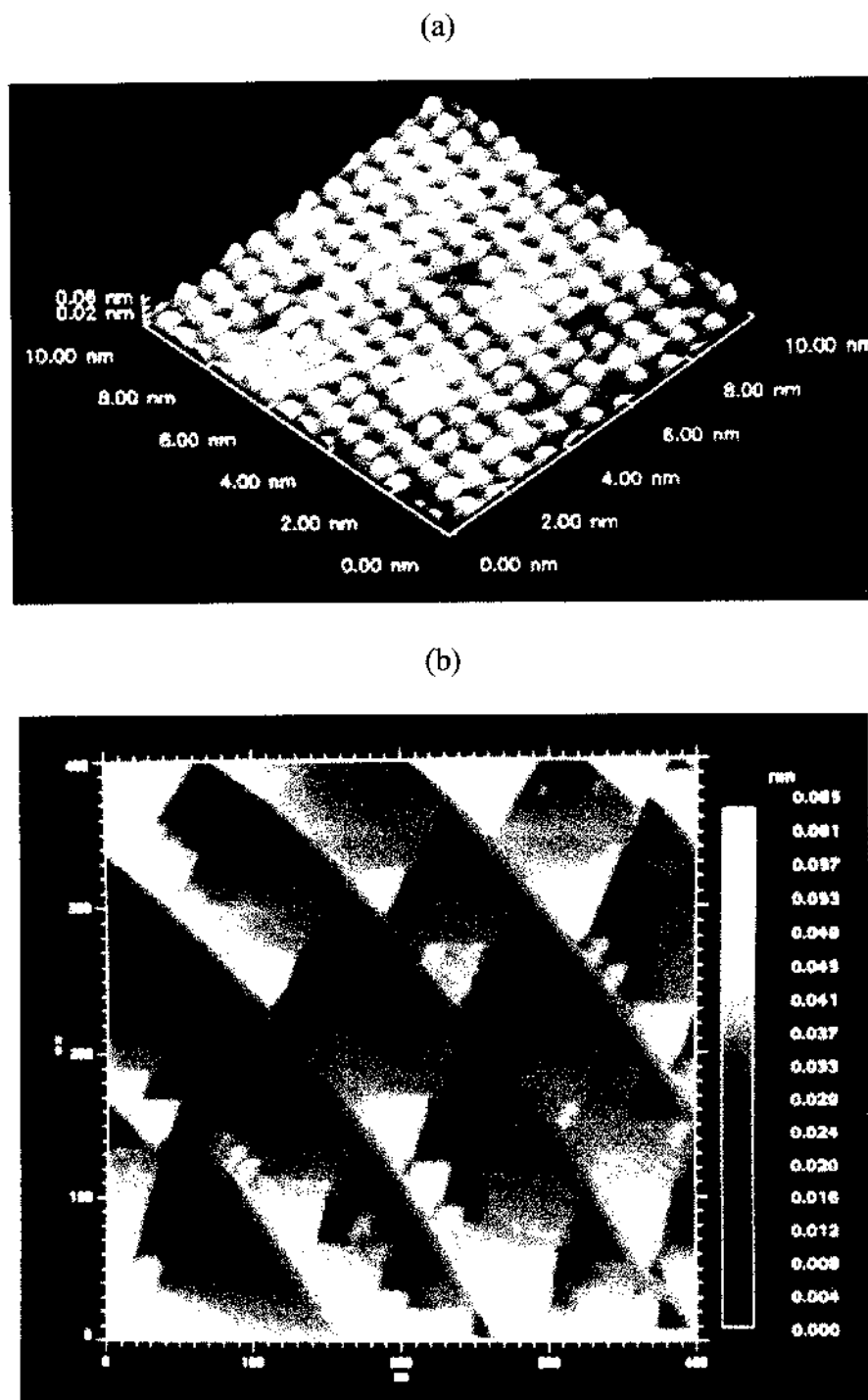


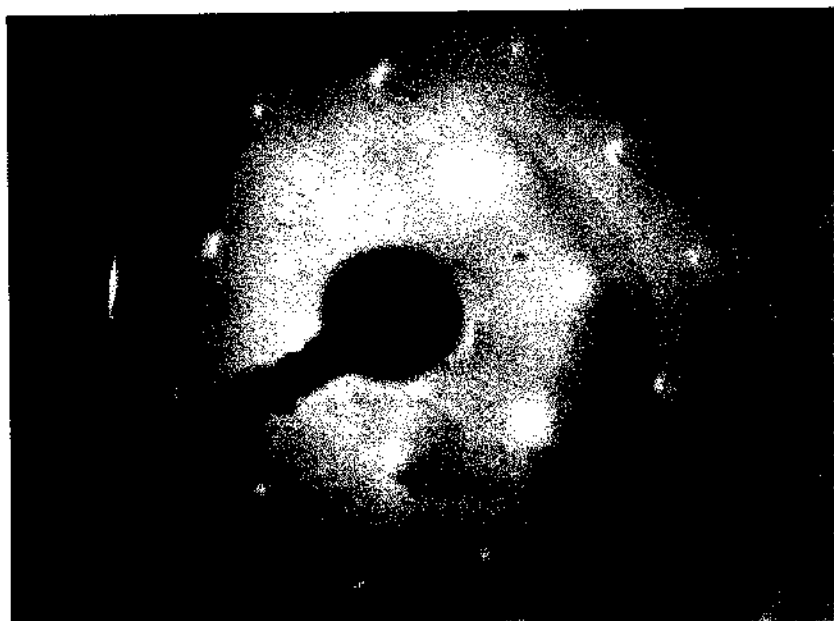
Figure 4.3. STM topographs of the “clock” surface. (a) An atomically resolved 10 nm x 10 nm area scan. Measurement parameters: sample bias = +0.01 V, feedback set = 3.00 nA, scan speed = 100 nm/s. (b) A 400 nm x 400 nm area scan. Measurement parameters: sample bias = -0.100 V, feedback set = 1.00 nA, scan speed = 1495.33 nm/s.

surface consisting of wide “triangular” terraces with an average width of ~ 1400 Å. The step heights are as high as ~ 50 Å. The steps are oriented along the energetically favourable $\langle 110 \rangle$ directions. Triangular mounds are evident whose edges are preferentially located on the step edges. In addition to the triangular mounds, other typical scans reveal saw-toothed structures, also formed on the step edges. It was observed that variations in the annealing time and temperature affect the topography of the surface. A well-annealed surface showed well-defined steps while a rougher surface was observed when the sample was annealed at shorter times after a sputtering procedure.

Fe(111)-(1×1)-S

Annealing of the “clock” structure to higher temperatures (≥ 700 K, up to 940 K) and at longer annealing times result in the significant segregation of S. Fig. 4.4a shows the (1×1) -S LEED pattern obtained for Auger peak-to-peak S/Fe intensity ratios in the range 0.9 - ~ 1.2 . The hexagonal pattern indicates that the S overlayer has the same periodicity as the Fe(111) substrate. Fig. 4.4b displays the typical Auger spectrum of the (1×1) -S surface. A representative atomic resolution STM image for the (1×1) -S surface is shown in Figure 4.5a. The image consists of a hexagonal array of protrusions. LEED intensity measurements on Fe(111)- (1×1) -S indicate that the S atoms sit on top of 3-fold hollow sites (1). The protrusions in Fig. 4.5a are therefore attributed to S atoms. The distance between neighboring maxima of the image (Fig. 4.5a) is found to be 4 Å which is in excellent agreement with the lattice constant of the Fe(111) surface (4.04 Å) (22). No image dependence on the bias polarity was observed (e.g. protrusions still observed even when the polarity used was

(a)



(b)

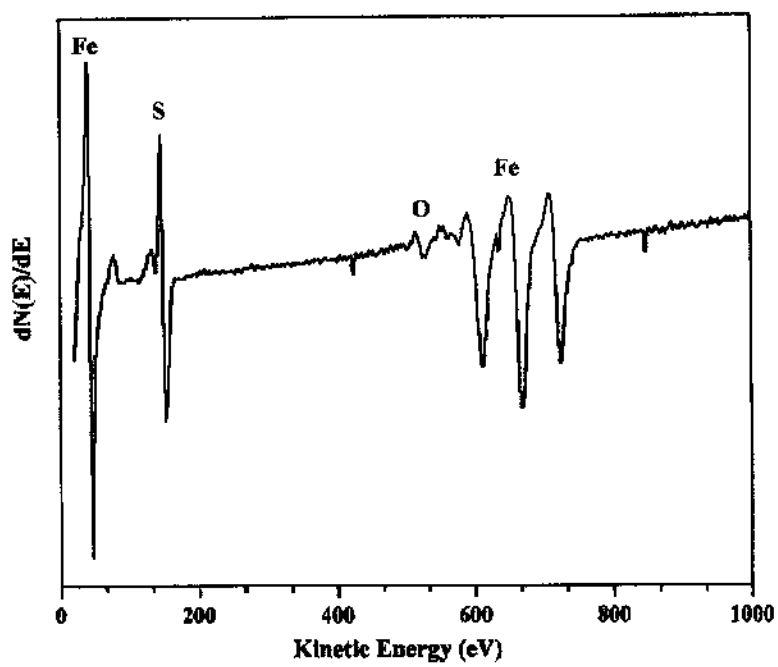
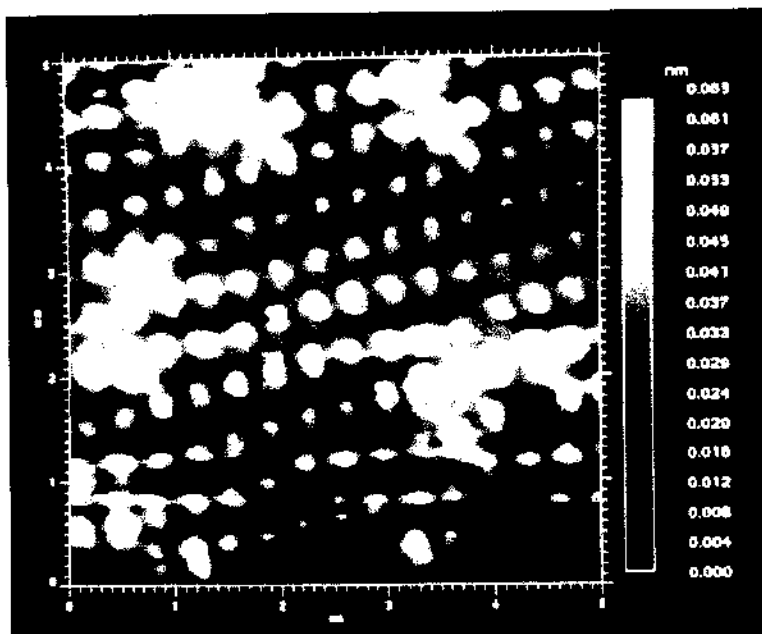


Figure 4.4. (a) LEED pattern obtained from the Fe(111)-(1×1)-S. Beam energy = 47 eV. (b) A typical Auger spectrum of the (1×1)-S surface.

(a)



(b)

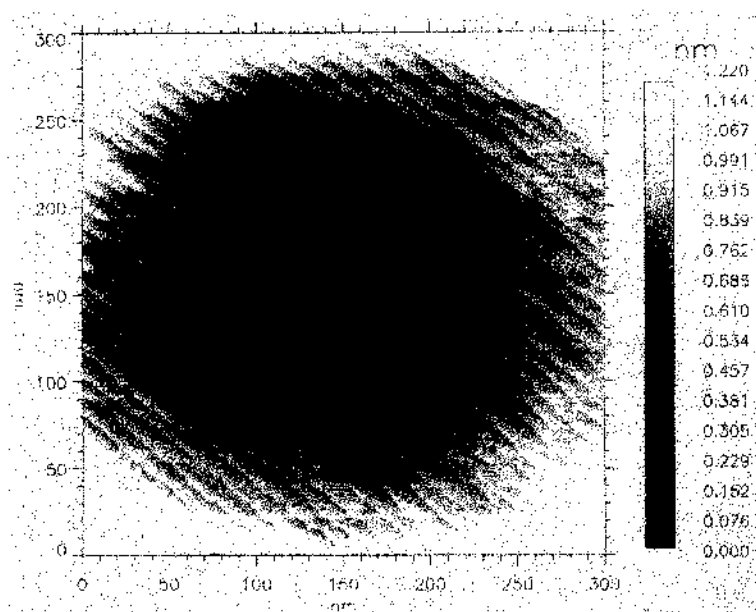


Figure 4.5. STM topographs of the Fe(111)-(1 \times 1)-S surface. **(a)** 5 nm \times 5 nm scan area. Measurement parameters: sample bias = +0.01 V, feedback set = 2.0 nA, scan speed = 50 nm/s. **(b)** A 300 nm \times 300 nm scan area. Measurement parameters: sample bias = +0.10 V, feedback set = 1.00 nA, scan speed = 1500 nm/s.

reversed). Previous studies (23, 24) of S adlayers on Ni and Pd have also imaged the S atoms as protrusions independent of bias polarity, consistent with the results presented here. The measured corrugation amplitude of S atoms in this present study is 1.0 Å, significantly larger than the corrugation amplitudes (0.3 - 0.4 Å) found for S atoms adsorbed on closed-packed Ni(111) surface (23). Fig. 4.5b shows a representative STM large area scan (300 nm × 300 nm) of the (1×1)-S phase. As can be seen from the image, the surface topography is dramatically different from the “clock” structure (Fig. 4.3b). The multi-height steps observed for the “clock” surface have broken up into narrow terraces approximately ~100 Å apart, separated by steps of single atom heights. Again, the terraces are oriented along one of the <110> directions.

Fig. 4.6 shows a 25 nm x 25 nm atomically resolved STM image of the Fe(111)-(1×1)-S surface. In addition to the monatomic steps, nanoscopic triangular pits are clearly evident on the surface. Fig. 4.7a displays a higher resolution image of one of the triangular pits which reveals that it is equilateral in geometry: all three of the pit’s edges are 11 atoms long. A three-dimensional representation of the pit (Fig. 4.7b) shows that it is only 1 atom deep. Further, the bottom of the pit is atomically resolved, showing an array of bumps of hexagonal symmetry. The triangular pits have the same orientation relative to the terraces. All are pointing to the next lower terrace. The triangular-shaped pits reflect the threefold symmetry of the (111) surface. This pitting increases in size and depth as the S coverage increases. The large-scale pitting which was observed only at S coverages greater than 1 “geometric” monolayer (Auger peak-to peak S/Fe ratios > ~ 1.4) are presented and discussed in the next subsection.

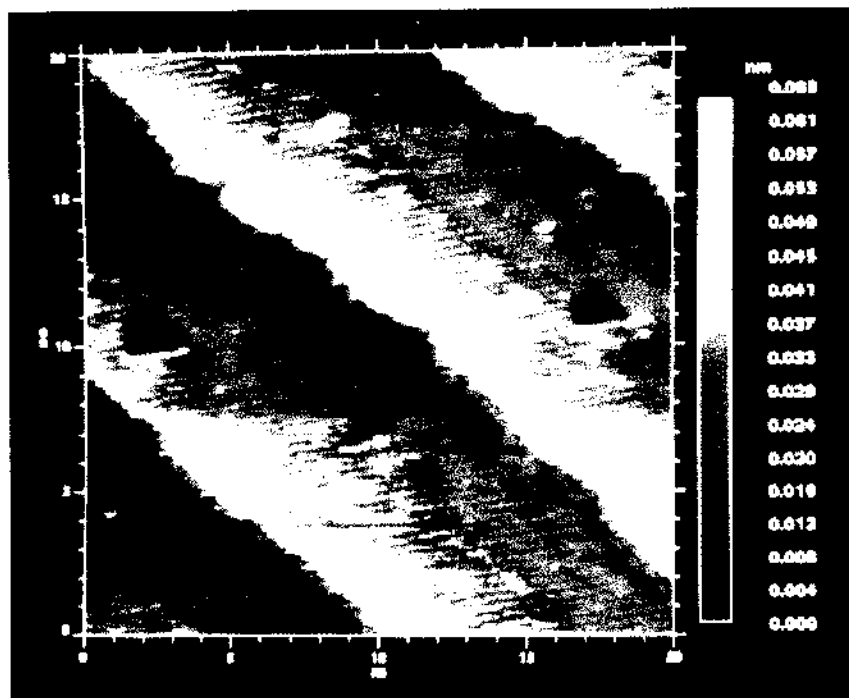


Figure 4.6. A 50nm x 50nm STM topograph of the Fe(111)-(1×1)-S surface. Nanoscopic triangular pits are present which are 1 atom deep. STM measurement parameters: sample bias = +0.10 V, feedback set = 2.0 nA, scan speed = 500 nm/s.

Fe(111)-(2√3×1)R30°-S

Further annealing of the specimen to even higher temperatures (up to 925 K) results in the transformation of the (1×1)-S structure to a new diffraction pattern presented in Fig. 4.8a. This new surface structure is assigned as the $(2\sqrt{3}\times 1)R30^\circ$ -S structure based on the atomic resolution images obtained for this surface, which is also consistent with the LEED symmetry shown in Fig. 4.8a. A typical Auger spectrum corresponding to the $(2\sqrt{3}\times 1)R30^\circ$ -S is shown in Fig. 4.8b. The $(2\sqrt{3}\times 1)R30^\circ$ -S phase is associated with more than 1 “geometric” ML coverage of S (based on 1 “geometric” ML coverage for the (1×1)-S phase) corresponding to Auger peak-to-peak S/Fe ratios greater than ~1.3 (highest S/Fe ratio achieved is 2.1). This is

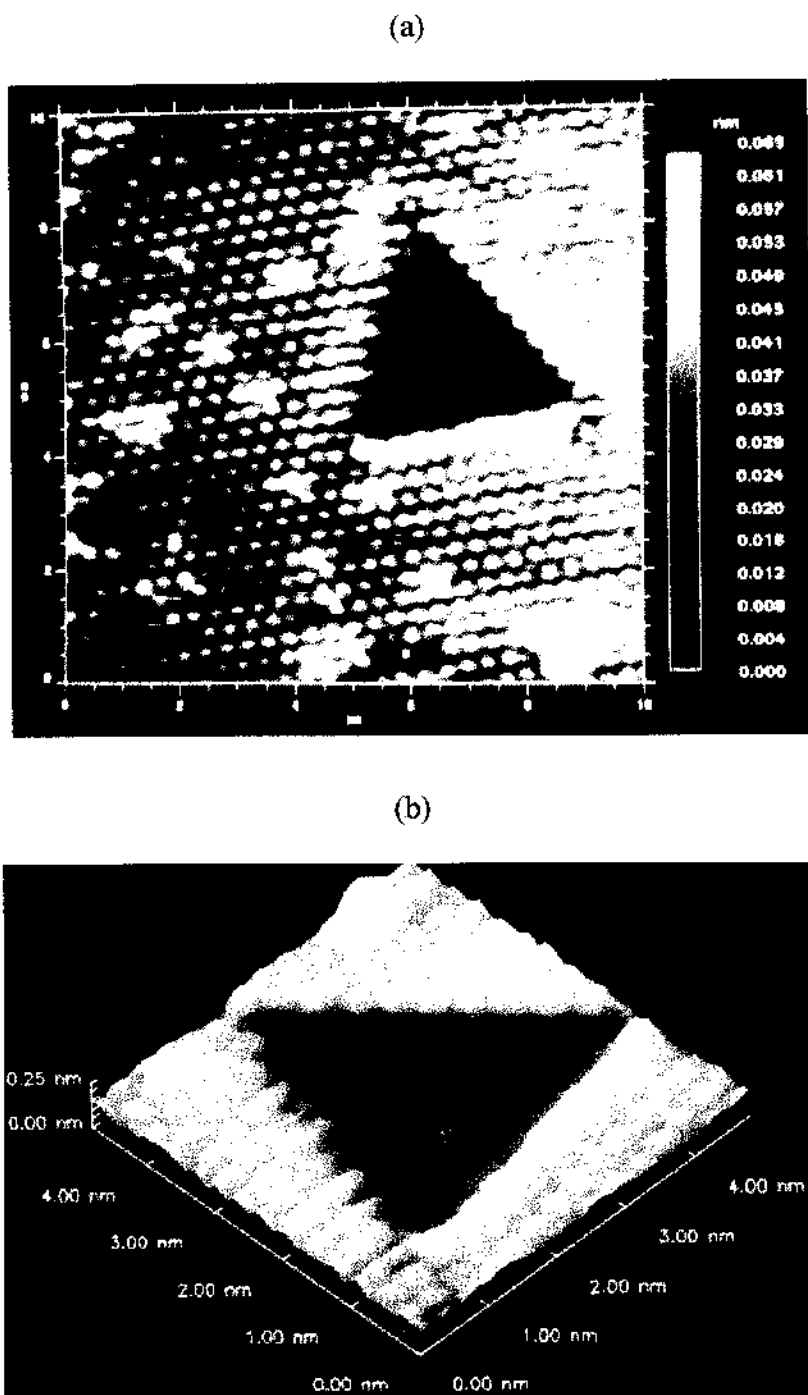


Figure 4.7. (a) A 10 nm x 10 nm STM topograph showing the equilateral triangular pit. The edges of the pit are 11 atoms long. (b) A 3-dimensional representation of the pit in (a). STM measurement parameters: sample bias = +0.10 V, feedback set = 2.00 nA, scan speed = 100 nm/s.

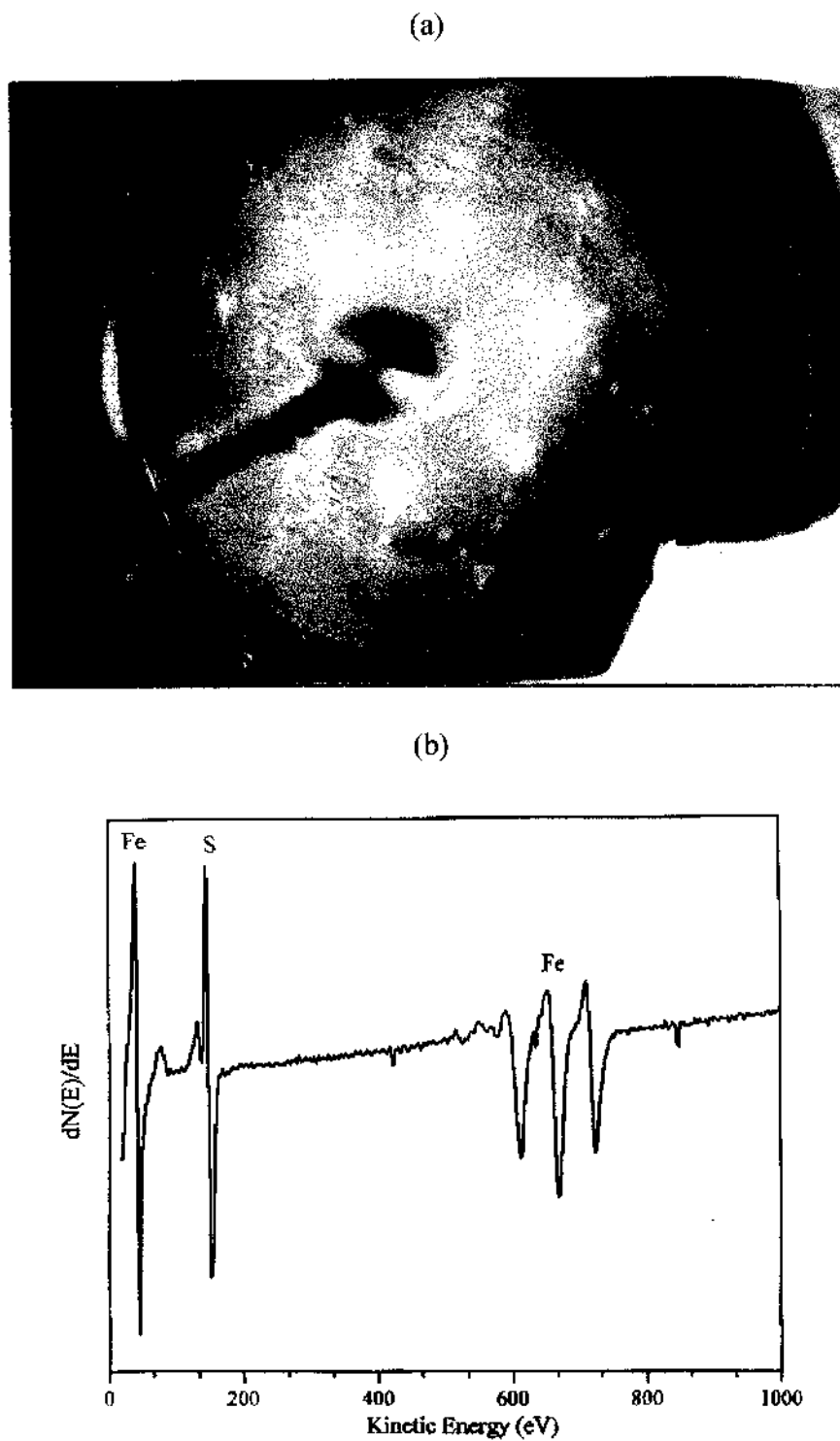


Figure 4.8. (a) LEED pattern obtained from the $\text{Fe}(111)-(2\sqrt{3}\times 1)R30^\circ\text{-S}$. Beam energy = 126 eV. (b) A typical Auger spectrum of the $(2\sqrt{3}\times 1)R30^\circ\text{-S}$ surface.

the first observation of a high-S coverage LEED pattern. Other investigators (1) have only reported the formation of a Fe(111)-(1×1)-S structure. The fact that this high-S coverage phase was not observed in those studies (1) may be due to a low bulk S concentration of the Fe(111) crystal used which contained only a total of 100 ppm of impurities (including S). In the present study, the Fe(111) crystal used initially contained 250 ppm S (21).

Fig. 4.9a shows a typical 400 nm × 400 nm STM scan of the $(2\sqrt{3} \times 1)R30^0$ -S surface. In contrast to the “clock” and (1×1)-S surfaces (Fig. 4.3b, 4.5b), the $(2\sqrt{3} \times 1)R30^0$ -S surface topography displays numerous triangular pits of various sizes. The pit depths range from 1 - 50 Å. The lengths of the pit’s edges range from 5 to 800 Å. The pitting is consistently observed for the $(2\sqrt{3} \times 1)R30^0$ -S phase. In addition to the pronounced pitting, the surface shows wide terraces separated by multi-height steps similar to those observed for the “clock” surface. This indicates that the monatomic steps observed on the (1×1)-S surface have coalesced upon the formation of the $(2\sqrt{3} \times 1)R30^0$ -S surface. Fig. 4.9b displays a 50 nm × 50 nm edge-enhanced (25) STM topograph of the pits. One can see clearly that within large pits a very periodic “step staircase” topography is observed. The “step staircase” spirals down into the bottom of the triangular pit. Fig. 4.10a shows a 25 nm × 25 nm STM image of the pitted surface along with its line profile taken perpendicular to the steps of a large pit. A preferential formation of a terrace width of 14 Å was observed, separated by steps one atom high, consistent with the $(2\sqrt{3} \times 1)R30^0$ -S LEED pattern. Atomically resolved STM images (Fig. 4.10b) obtained on the terraces inside a large pit reveal a hexagonal pattern of protrusions

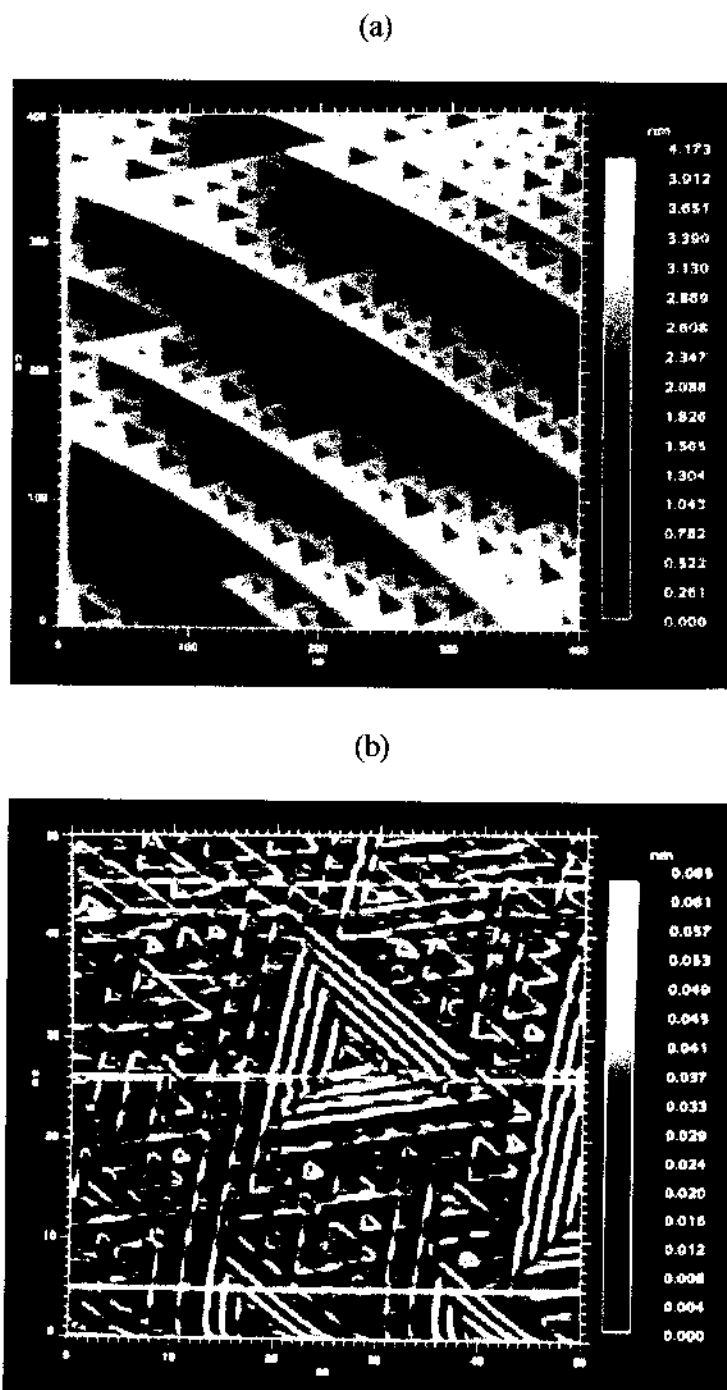


Figure 4.9. (a) A 400 nm x 400 nm STM topograph of the $\text{Fe}(111)-(2\sqrt{3}\times 1)R30^\circ\text{-S}$ surface. Measurement parameters: sample bias = +0.10 V, feedback set = 1.00 nA, scan speed = 1495.33 nm/s. (b) An edge-enhanced 50 nm x 50 nm STM topograph of the triangular pitting. A Roberts edge-enhancement procedure was used (see ref. (25)). Measurement parameters: sample bias = +0.05 V, feedback set = 1.00 nA, scan speed = 298.51 nm/s.

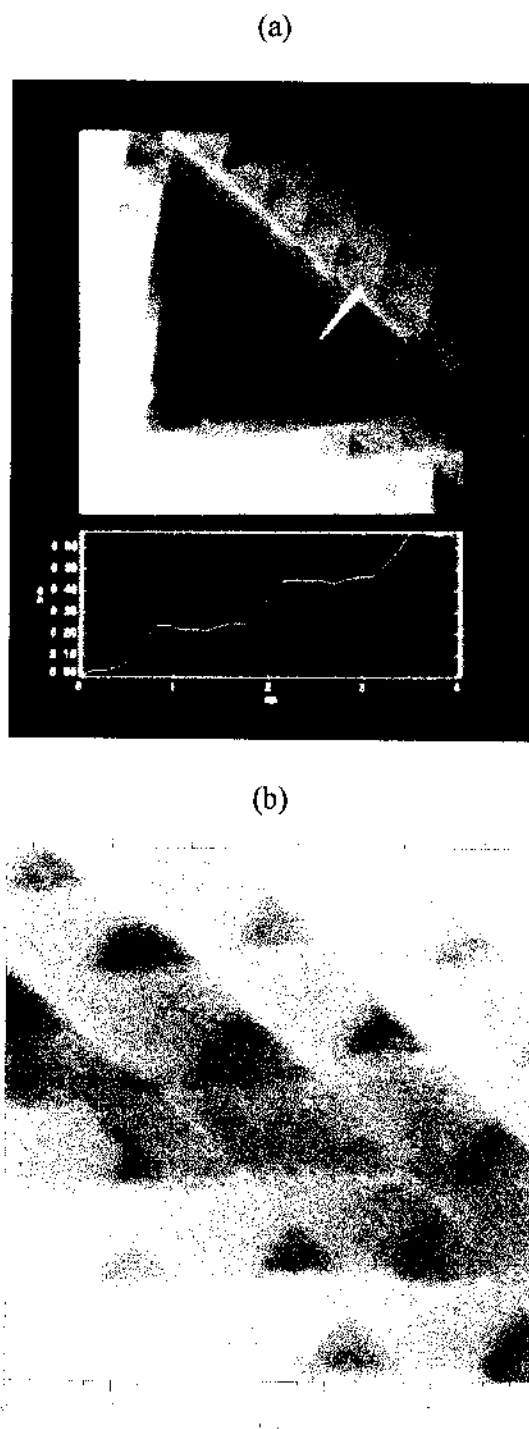


Figure 4.10. (a) A 25 nm x 25 nm STM topograph of the $(2\sqrt{3}\times 1)R30^0$ -S surface along with a line profile. The preferential formation of a 14 Å terrace width is observed. (b) A 10 nm x 10 nm scan area showing an atomically resolved image of "pits within a pit".

identical to that of the (1×1) -S phase. The terraces are therefore unreconstructed maintaining the (111) - (1×1) -S periodicity. The 14 Å terrace periodicity corresponds to a (111) terrace which is 5 atomic rows wide. Therefore, the new surface formed inside the pits correspond to the step-terrace notation $5(111)\times(100)$ (26). The slope of this new surface relative to the (111) plane is found to be approximately 12 degrees based on STM measurements. The image shown on Fig. 4.10b further reveal the presence of “pits within a pit”. These small pits which are one atom deep are regularly spaced from each other (Fig. 4.10a, b) indicating that a long range interaction is at work. Terrace widths of 28 Å (Fig. 4.10b), twice the usual terrace periodicity, were also observed.

While the terraces inside the pits of the $(2\sqrt{3}\times 1)R30^0$ -S surface are unreconstructed, atomic resolution STM images obtained from flat areas in between large pits revealed surface buckling (Fig. 4.11a and 4.12). It is pointed out that these surface buckling was observed only between large pits and that the $(2\sqrt{3}\times 1)R30^0$ -S surface was mainly populated by the triangular pits. Two packing arrangements of the surface buckling were observed. One of these packing arrangements is shown in Figures 4.11a with a superimposed unit cell of the new surface structure. The image consists of troughs and crests of atomic rows oriented along one of the $\langle 110 \rangle$ directions. The separation distance between similarly displaced atomic rows is 14 Å. This value is $2\sqrt{3}$ times the atomic distance of the Fe(111). The new unit cell is 30^0 rotated relative to the substrate unit cell (Fig. 4.11b), hence, the assignment of a $(2\sqrt{3}\times 1)R30^0$ -S notation for this phase. The image shown in Fig. 4.11a corresponds to one of the 3 equivalent

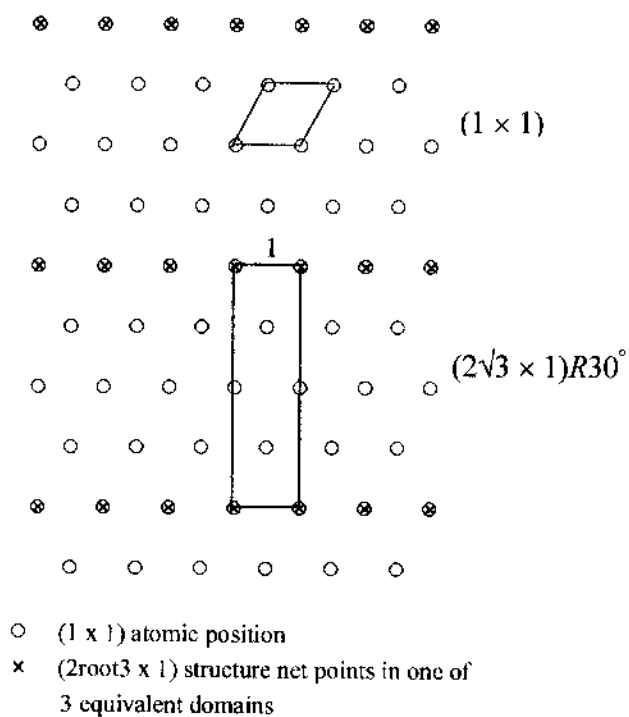
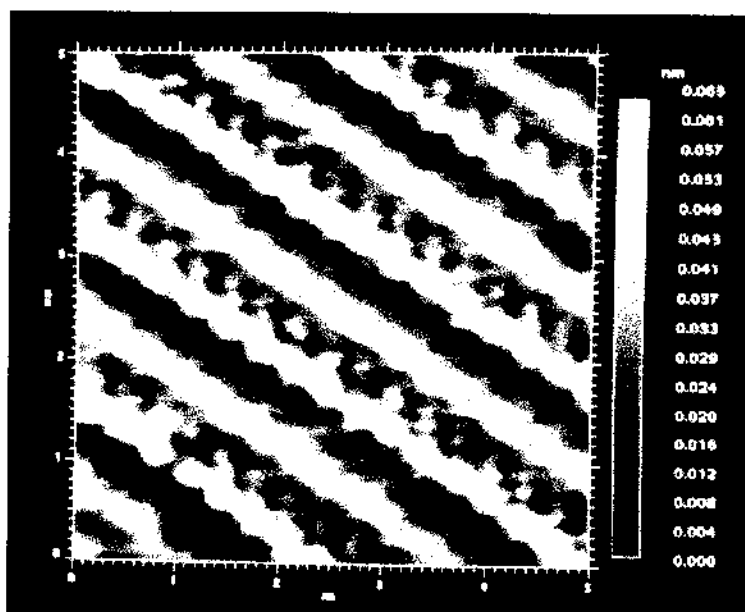


Figure 4.11. An atomically resolved (5 nm × 5 nm) surface buckling of the $(2\sqrt{3} \times 1)R30^\circ$ phase. Measurement parameters: sample bias = +0.01 V, feedback set = 5 nA, scan speed = 50 nm/s. Also shown is a schematic of the bcc(111) surface and the unit cells of the substrate (1 × 1) and the superstructure $(2\sqrt{3} \times 1)R30^\circ$.

domains accountable for the $(2\sqrt{3} \times 1) R30^0$ -S coincidence mesh. It can be seen that two adjacent atomic rows are atomically resolved, with one atomic row more elevated than the other. The atomic periodicity along each of these rows is measured to be 4 Å, identical to that of the (1×1) -S phase. The corrugation height along each atomically resolved row is 1.0 Å, also identical to that of the Fe(111)- (1×1) -S structure. Located in between the most elevated rows of atoms (Fig. 4.11a) is a slightly lower row of atoms. This row is not atomically resolved. Next to this unresolved atomic row is presumably another atomic row which is invisible to the STM. The fact that the separation distance between identical elevated rows of atoms is 14 Å implies that the (1×1) atomic periodicity is maintained on the surface even though vertical displacements of the atomic rows have occurred. Slight horizontal displacements may also have occurred but this level of detail could not be inferred from the STM data.

Fig. 4.12 shows a different packing arrangement of the surface buckling. In this image, elevated *groupings* of vertically displaced atomic rows are evident. Again, the separation distance between the highest points of the groupings is 14 Å, in accord with the $(2\sqrt{3} \times 1) R30^0$ unit cell. The distance between the highest point of the buckled rows relative to the lowest point of the surface is approximately 2 Å, twice as high as the height of the most elevated atomic rows in Fig. 4.11a. Both images presented in Figures 4.11a and 4.12, while different in their atomic packing arrangements, yield the same $(2\sqrt{3} \times 1) R30^0$ LEED pattern since they both have identical periodicity. STM observations of two different atomic packing arrangements associated with the same LEED pattern have been reported before (27).

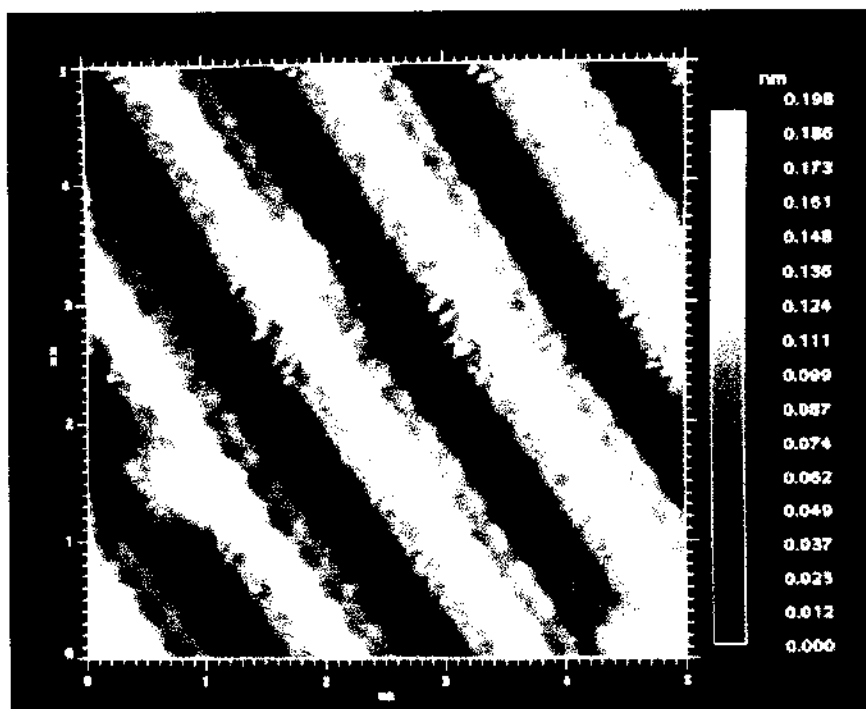


Figure 4.12. Surface buckling obtained from flat areas near the triangular pits. Measurement parameters: sample bias = +0.01 V, feedback set = 5 nA, scan speed = 50 nm/s. This is one of the two different packing arrangements of the atomically resolved images obtained between large pits of the $(2\sqrt{3}\times 1)R30^\circ$ -S surface.

Oxidation behavior of the S-modified Fe(111) surfaces

Fig. 4.13 displays the O_2 uptake curves of the Fe(111) with varying coverages of S. The partial pressures of O_2 during oxidation were varied between 10^{-8} Torr- 10^{-6} Torr. The oxidations were carried out at room temperature. As shown in the figure, the sticking coefficient of O_2 decreases as the S coverage increases. At exposures of 100 L of O_2 , the decrease in the oxygen coverage (measured as Auger O/Fe peak-to-peak intensity ratios) to the (1×1) -S surface compared to the clean Fe(111) is approximately 1 order of magnitude, consistent with the results of a previous study (3). For the high sulfur coverage phase,

$(2\sqrt{3} \times 1)R30^0$ -S surface, no significant adsorption of oxygen is observed at exposures of 1000 L of O_2 . Further oxidation experiments using 1600 L of O_2 did not result in any significant oxygen uptake. The sticking coefficient of O_2 on the $(2\sqrt{3} \times 1)R30^0$ surface was calculated to be $< 10^{-5}$, indicating a drastic decrease in the reactivity for this surface.

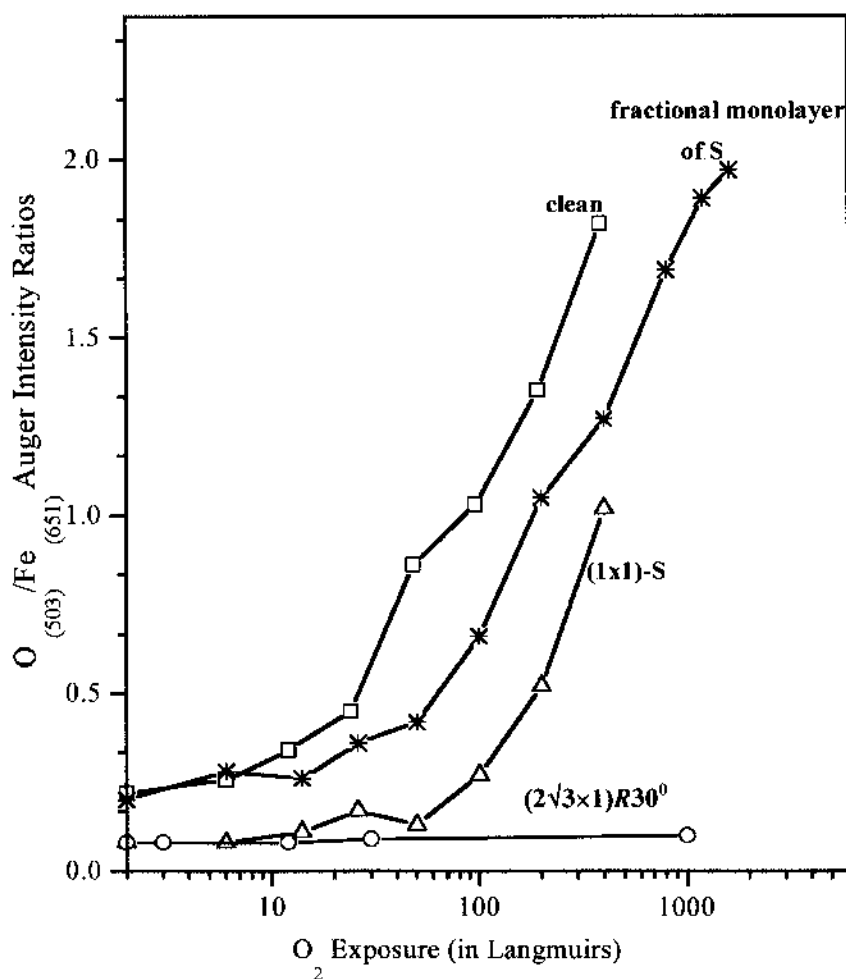


Figure 4.13. Auger peak-to-peak $O_{(503)}/Fe_{(651)}$ intensity ratios as a function of O_2 on the Fe(111) surface with varying precoverages of S. The oxygen uptake curves are measured at room temperature. “clean” Fe and Fe with submonolayer S have an initial trace impurity of oxygen (8 % atomic conc.). The partial pressure of O_2 used in obtaining these plots is 10^{-7} Torr.

Discussion

As presented above, the Fe(111) surface undergoes structural transformations (faceting-planar transitions) upon the segregation of varying coverages of S. At low coverages of S and other trace impurities, the Fe(111) surface facets forming triangular terraces separated by multi-height steps (Fig. 4.2, 4.3b). The LEED pattern for this surface consists of a “clock” pattern which interestingly, has not been reported by previous investigators (1). Previous LEED studies on clean Fe(111) reported only the (1×1) structure which indicates that no faceting of the Fe(111) surface occurred, in contrast to the results presented here. The variance of these data with the previous study (1) may be related to the presence of electronegative adsorbates (S, N and O) on the Fe(111) surface in the present study. In the literature, several investigators (28-31) have reported on the pronounced effects of trace impurities on the step morphology of Ag(110). STM measurements (28, 29) have revealed that impurities act as “step pinning sites” which means that clusters of impurities on the surface “pinned” the steps thus preventing step movement. Consequently, the surface cannot achieve a local equilibrium configuration (28, 29). In these previous reports (28, 29), STM images of the less-than-clean Ag(110) surface configuration showed poorly defined step edges along with the “pinning centers” consisting of clusters of impurity atoms and pinned steps. In contrast, the STM image shown on Fig. 4.3b revealed well-defined edges of steps. No “step pinning sites” seem to be present on the surface. It appears then that the surface configuration for the “clock” structure is a thermodynamic phase and cannot be ascribed

to a non-thermodynamic, “step pinning” morphological configuration. Since previous investigators (1) did not observe faceting on a clean Fe(111) structure, it is therefore entirely possible that the electronegative impurities present on the Fe(111) surface induced this faceting transformation.

In contrast to the faceted “clock” surface, the (1×1)-S surface exhibited a planar topography. The multi-height steps in the “clock” structure have broken up forming narrower terraces which are more or less evenly spaced at 100 Å, separated by monatomic steps (Fig. 4.5). The real space structure for Fe(111)-(1×1)-S has been previously proposed based on LEED and work function measurements (1). This model consists of S located at *on-top* 3-fold hollow sites (see Fig. 4.14). Since Fe(111) is an open surface (atomic periodicity = 4.06 Å (22)), its second and third atomic layers are exposed to the environment (Fig. 4.14a) (5). There are, therefore, 2 types of 3-fold hollow sites on the Fe(111): *on-top* and *subsurface* (Fig. 4.14a). This makes the definition of a monolayer of adsorbate ambiguous. To clarify this ambiguity, previous investigators (20, 32-35) have introduced the concept of a “geometric” monolayer which corresponds to the number of adsorbate atoms that cover one of the exposed atomic layers of the substrate surface (Fig. 4.14b). The model previously proposed (1) for the Fe(111)-(1×1)-S therefore consists of a “geometric” monolayer of S atoms residing at *on-top* 3-fold hollow sites of the Fe(111) surface (Fig. 4.14b). This is confirmed by the atomically resolved image shown in Fig. 4.5a which shows that the atomic periodicity of the (1×1)-S surface is Å, in excellent agreement with the lattice spacing of the Fe(111) surface (4.05 Å). As shown by the data,

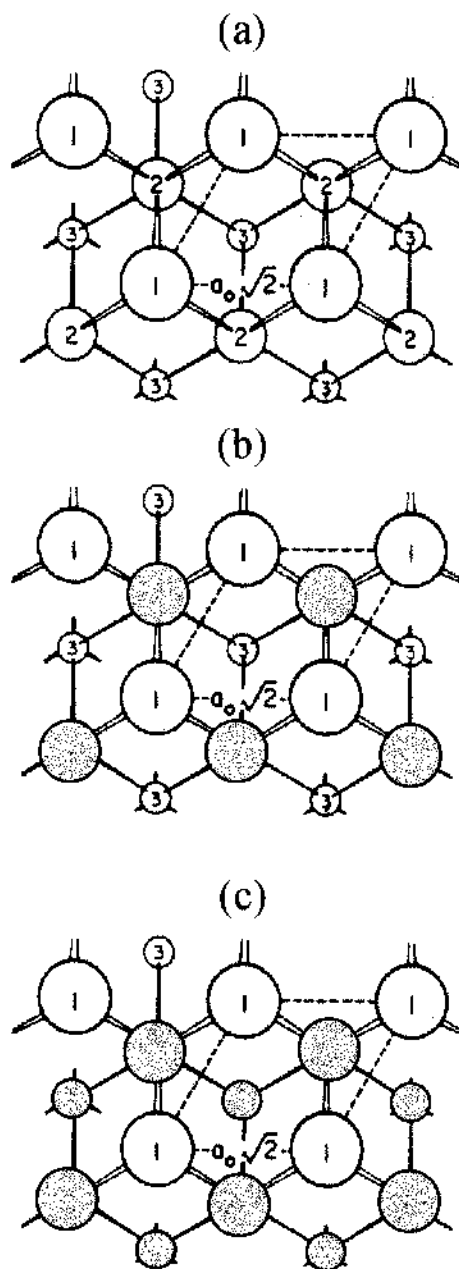


Figure 4.14. (a) Top view of the bcc(111) surface showing the first, second and third atomic layers marked 1, 2 and 3 respectively; *on-top* and *subsurface* 3-fold hollow sites correspond to positions located on top of substrate atoms 2 and 3 respectively; a_0 is the side of the unit cell. (reprinted with permission [35]). (b) A bcc(111) surface with overlayer atoms located at *on-top* 3-fold hollows covering the second atomic layer of the substrate. (c) A bcc(111) surface with overlayer atoms located at both *on-top* and *subsurface* 3-fold hollows covering the second and third atomic layers of the substrate.

the segregation of one “geometric” ML of S removes the faceting from the “clock” surface and in effect “heals” the surface, allowing it to adopt its bulk-terminated configuration (Fig. 4.5b).

The $(2\sqrt{3} \times 1)R30^\circ$ -S surface, associated with more than one “geometric” monolayer of S, exhibits a radically different morphology (Fig. 4.9a,b) consisting of triangular pits of varying sizes and depths. The nanoscopic triangular pits observed in the (1×1) -S surface is therefore attributed to the onset of a faceting transformation leading to the large-scale pitting in the $(2\sqrt{3} \times 1)R30^\circ$ -S phase. The STM measurements also revealed that the monatomic steps have coalesced and reformed the multi-height steps reminiscent of the “clock” surface. A similar effect of S on Mo(100) have been reported from previous LEED and STM studies (19). S was observed to change the morphology of the Mo(100) varying the surface’s step structure from multi-height steps, double steps and monatomic steps depending on S coverage.

In addition to the triangular pitting, the $(2\sqrt{3} \times 1)R30^\circ$ -S surface is also characterized by surface buckling with a periodicity of 14 Å, identical to the periodicity exhibited by the terraces found with large pits. It is noted, however, that the surface buckling is not typical, i.e., the $(2\sqrt{3} \times 1)R30^\circ$ -S phase is predominantly populated by the triangular pits. This implies that the surface buckling is a metastable state. This may eventually transform into a pitted morphology, presumably the surface of true-energy minimum.

The large scale triangular pitting on the Fe(111) surface was initiated only when the critical S coverage of one “geometric” monolayer S was exceeded. A similar adsorbate-coverage dependence for faceting has been observed for W(111) (20, 32-35) and Mo(111) (35, 36) surfaces deposited with overlayers of certain transition metals and non-metallic elements. W(111) and Mo(111), like Fe (111), are bcc metals. These previous LEED and STM studies have revealed the formation of triangular pyramids with $\{211\}$ facets, in contrast to the triangular pits observed in the present study. The pyramidal faceting occurs upon annealing of the W(111) and Mo(111) surfaces precovered with at least one “physical” monolayer of Pd, Pt, Au, Rh or Ir (35). S was also observed to cause faceting on the W(111) surface (20). However, details on the nature of these facets have not been reported.

What drives the faceting transformation from the planar (1×1) -S to the triangular faceting and surface buckling of the $(2\sqrt{3} \times 1)R30^\circ$ -S? From the thermodynamic perspective, of course the driving force for faceting is the minimization of the total surface free energy (14, 30, 31, 37). It has been known from early thermodynamic work (14, 37) on crystal surfaces that adsorption changes the surface free energy as well as the dependence of the surface free energy with the crystal orientation. This variation of surface free energy with orientation is referred to as the anisotropy of the surface free energy of a crystal surface (14, 30, 31, 37). The increase in the anisotropy of the surface free energy has been suggested as the driving force for the triangular pyramidal faceting observed for W(111) and Mo(111) surfaces (38). The triangular pit formation observed

for the high S-coverage phase on Fe(111) may also be driven by the same mechanism of adsorbate-induced anisotropy of the surface free energy. The $(2\sqrt{3}\times 1)R30^\circ$ transformation may also be dictated by the need for the Fe(111) surface to create more adsorption sites for S in order to accommodate the increase in S atom surface density. Formation of more step edges as S coverage increases is intuitively reasonable since step edges are favorable adsorption sites because of the preference of S to maximize its coordination number (5, 6, 39).

There is an alternative explanation for the faceting and surface buckling observed for the high S-coverage. This can be understood by considering the two different adsorption sites of S on the Fe(111) surface. It is speculated here that in the $(2\sqrt{3}\times 1)R30^\circ$ -S phase, the segregation of S to the *subsurface* 3-fold hollow sites has occurred, in addition to the S atoms already residing at the *on-top* 3-fold hollows (Fig. 4.14c). S occupancies at both hollow sites place S atoms in close proximity with each other thus creating repulsive interactions. This repulsive stress can then result in the morphological changes of the surface. The segregation of S to the *subsurface* 3-fold hollows at the $(2\sqrt{3}\times 1)R30^\circ$ -S phase is consistent with results from the oxidation studies (Fig. 4.13). On the Fe(111)-(1×1)-S surface containing one “geometric” monolayer of S (at *on-top* 3-fold sites), *subsurface* 3-fold hollow sites are still exposed and may act as sites for O₂ dissociation (Fig. 4.14b). This would explain the susceptibility of the (1×1)-S surface to oxidation. At the $(2\sqrt{3}\times 1)R30^\circ$ surface, assuming the hypothesis is correct, both *on-top* and *subsurface* 3-fold hollows are occupied (Fig. 4.14c). Therefore, O₂

dissociation cannot occur. It is noted that the 14 Å periodicity of the surface buckling and “staircase” pitting (Fig. 4.9) appears to be consistent with the segregation of S every $2\sqrt{3}$ *subsurface* 3-fold hollow site. If this is the case, not all of these *subsurface* sites are blocked with S and O₂ dissociation may still occur since some *subsurface* 3-fold hollows are still available. However, a certain site ensemble may be required in order for O₂ dissociation to take place. Such required site ensembles for O₂ dissociation have been previously observed for catalytic oxidization of CO on the Pt(110) surface (1). S was found to poison the Pt surface via a combination of electronic and geometric blocking effect of S on the dissociation of O₂. The passivity of the $(2\sqrt{3}\times 1)R30^\circ$ -S surface to O₂ attack may be due to a similar effect of S on the Fe(111) surface. Another possible explanation for the inertness of the $(2\sqrt{3}\times 1)R30^\circ$ -S phase to oxidation is the formation of a surface compound. However, the new surface $5(111)\times(100)$ within the pits (Fig. 4.9b) does not correspond to the dimensions of any of the Fe sulfide unit cells. It therefore appears that no surface compound formation has occurred in this case.

In these experiments, it has not been possible to separate the annealing step from the S segregation process (i.e. the high-S phase required annealing the crystal at more elevated temperatures). So the question now is: how is it known that these structural transformations on Fe(111) are indeed due to segregated S and not due simply to thermal effects? Fig. 4.15 shows evidence that these transformations are not effected by thermal annealing alone. It displays the relationship between annealing temperature and the surface structure observed. It turns out that repeated cycles of sputter-anneal gradually

depletes the amount of S in the bulk. Therefore, at a later time (after several sputter-anneal cycles), in order to obtain the same (1×1) -S coverage from the S-depleted Fe(111) crystal, annealing at higher temperatures was required, *the same temperatures that was used to achieve the high-S coverage phase originally* (Fig. 4.15). As long as the S coverage is within the coverage regime of S/Fe ratios between 0.90 to 1.2, only the (1×1) -S LEED pattern is observed and no large-scale pitting occurs, *regardless of the high annealing temperatures*. The same is true for the “clock” surface. Only the “clock” LEED pattern was observed even as the S-depleted crystal was annealed at higher

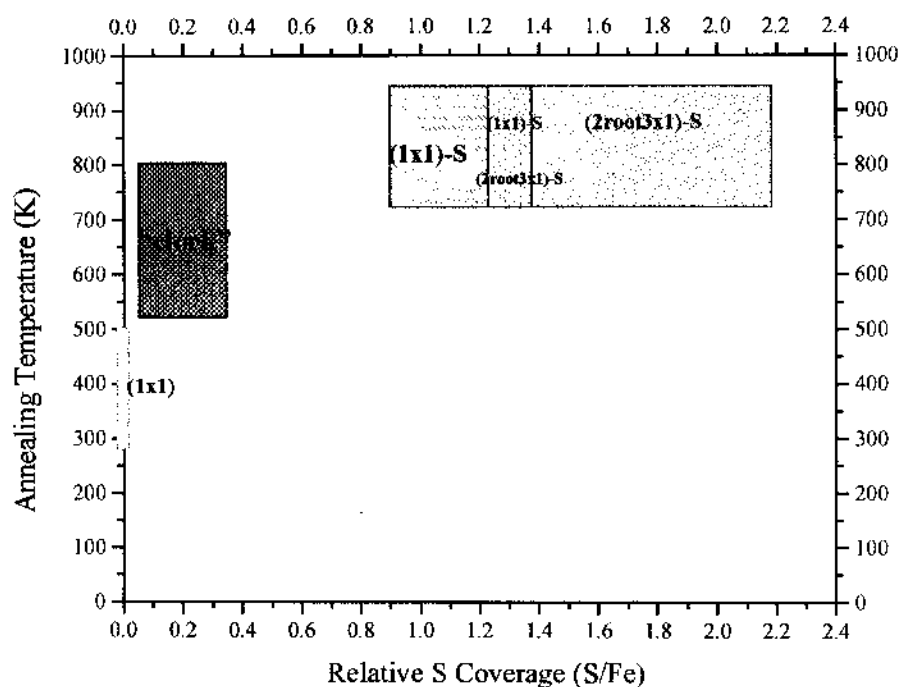


Figure 4.15. A plot showing the relationship between annealing temperature and the surface phase observed. The horizontal axis is the S/Fe Auger peak-to-peak intensity ratio. The vertical axis represents the annealing temperature (K) at which the corresponding LEED pattern was observed.

temperatures. The highest S/Fe ratio observed for the “clock” pattern is 0.35 while the N and O concentrations varies up to 20 atomic %. LEED measurements for the coverage regime in between the “clock” and the (1×1)-S phases have not been explored. It is concluded that the structural transformations observed on the Fe(111) surface is tied to the S coverage and cannot be ascribed solely to thermal effects.

Summary and Conclusions

The results presented showed clearly that S interacts very strongly with the steps of the Fe(111) surface resulting in the structural transformations (faceted-planar transitions) depending on S coverage. At low coverages of S and other trace impurities, a “clock” LEED structure was observed along with a faceted Fe(111) surface which appears to be a thermodynamic phase and not an impurity-driven (non-equilibrium) morphology. Upon further annealing, the segregation of S is induced resulting in the formation of a (1×1)-S surface. STM images of the (1×1)-S revealed a planar topography indicating that segregation of 1 “geometric” ML of S “heals” the surface allowing it to adopt a configuration identical to that of its bulk-terminated phase. Atomically resolved images of the (1×1)-S surface is consistent with the proposed model of S atoms occupying *on-top* 3-fold hollow sites of the Fe(111) surface. The presence of nanoscopic triangular pitting was observed on the (1×1)-S which is attributed to the onset of an unusual triangular faceting. This triangular faceting occurs only upon the segregation of additional S to the (1×1)-S surface coincident with the transformation to a $(2\sqrt{3}\times 1)R30^\circ$ structure. This surface phase corresponds to more than 1 “geometric” monolayer of S. Within large pits, a very

periodic “step staircase” topography was observed. Atomic resolution images within the pits reveal that the terraces are unreconstructed maintaining the (111) orientation. The new surface formed within large pits corresponds to the step notation $5(100)\times(111)$. Images obtained on flat areas in between large pits reveal surface buckling consisting of two different packing arrangements. The terraces within large pits and the surface buckling display identical periodicities of 14 Å. It is proposed here that the formation of $(2\sqrt{3}\times 1)R30^\circ$ phase involves the segregation of S to *subsurface* 3-fold hollow sites, in addition to the S atoms already residing at *on-top* 3-fold hollows of the (1×1) -S. This surface configuration can result in repulsive S-S interactions driving the surface to undergo the observed structural transformations. This hypothesis is supported by the results of the oxidation of these S-modified Fe(111) surfaces which indicate that the $(2\sqrt{3}\times 1)R30^\circ$ -S surface is extremely inert toward oxidation at room temperature. The structural instability of the Fe(111) surface with respect to the segregation of S may have practical implications to the problem of intergranular fracture which is associated with the segregation of S and other impurities to the grain boundaries of metallic materials.

Chapter References

- (1) Arabczyk, W.; Mussig, H. J.; Storbeck, F. *Physica Status Solidi. (a)* **1979**, *55*, 437.
- (2) Arabczyk, W.; Baumann, T.; Mussig, H.-J.; Storbeck, F. *Vacuum* **1990**, *41*, 79.
- (3) Arabczyk, W.; Narkiewicz, U.; Kalucki, K.; Freidenberg, E. *Applied Surface Science*. **1993**, *72*, 45.
- (4) Muller, O. G.; Katzel, W.; Storbeck, F. *Physica Status Solidi*. **1985**, *89*, 89.

- (5) Somorjai, G.A., *Introduction to Surface Chemistry and Catalysis*; John Wiley & Sons, Inc., New York, 1994; p. 49.
- (6) Titmus, S.; Wander, A.; King, D. A. *Chemical Reviews*. **1996**, *96*, 1291.
- (7) Sokolov, J.; Jona, F.; Marcus, P.M. *Physical Review B*. **1986**, *33*, 1397.
- (8) Shih, H.D.; Jona, F.; Jepsen, D.W.; Marcus, P.M. *Surface Science* **1981**, *104*, 39.
- (9) Legg, K. O.; Jona, J.; Jepsen, D. W.; Marcus, P. M. *Surface Science*. **1977**, *66*, 25.
- (10) Shih, H. D.; Jona, F.; Jepsen, D. W.; and Marcus, P. M. *Physical Review Letters*. **1981**, *46*, 731.
- (11) Kiskinova, M. *Chemical Reviews*. **1996**, *96*, 1431.
- (12) Shih, H. D.; Jona, F. *Physical Review Letters*. **1981**, *46*, 731.
- (13) Perdereau, M.; Oudar, J. *Surface Science*. **1970**, *20*, 80.
- (14) Woodruff, D. P. *Journal of Physics. Condensed Matter* **1994**, *6*, 6067.
- (15) Grossmann, A.; Erley, W.; Ibach, H. *Surface Science*. **1995**, *337*, 183.
- (16) Gardin, D. E.; Batteas, J. D.; Van Hove, M. A.; Somorjai, G. A. *Surface Science*. **1993**, *296*, 25.
- (17) Mullins, D. R.; Huntley, D. R.; Overbury, S. H. *Surface Science*. **1995**, *323*, L287.
- (18) Backer, R.; Horz, G. *Vacuum* **1995**, *46*, 1101.
- (19) Dunpy, J. C.; Knight, C.; Sautet, P.; Ogletree, D. F.; Somorjai, G. A.; Salmeron, M. B. *Surface Science*. **1993**, *280*, 313.
- (20) Guan, J.; Campbell, R. A.; Madey, T. E. *Surface Science*. **1995**, *341*, 311.
- (21) Electronic Space Products International (ESPI). 1050 Benson Way, Ashland, OR 97520. Sample lot number E3713.

- (22) MacLaren, J. M.; Pendry, J. B.; Rous, P. J.; Saldin, D. K.; Somorjai, G. A.; Van Hove, M.A.; Vvedensky, D. D. *Surface Crystallographic Information Service*; D. Reidel Publishing Company, Holland, 1988; p.86.
- (23) Ruan, L.; Stensgaard, I.; Besenbacher, F.; Laegsgaard, E. *Physical Review Letters*. **1993**, *71*, 2976.
- (24) Forbes, J. G.; Gellman, A. J.; Dunphy, J. C.; Salmeron, M. *Surface Science*. **1992**, *279*, 68.
- (25) Omicron SPM Software 2.0: Roberts Edge Enhancement is an optical computing edge detection scheme using a Roberts operator; see Cherri, A.K.; Karim, M.A. *Applied Optics* **1989**, *28*, 4644.
- (26) Ohtani, H.; Kao, C.-T.; Van Hove, M. A.; Somorjai, G. A., *Progress in Surface Science*. **1986**, *23(2/3)*, 155.
- (27) Schardt, B. C.; Yau, S.-L., Rinaldi, F. *Science* **1989**, *243*, 1050.
- (28) Held, G. A.; Goodstein, D. M.; Feenstra, R. M. *Physical Review B* **1993**, *48(11)*, 8458.
- (29) Ozcomert, J.S.; Pai, W.W.; Bartelt, N.C.; Reutt-Robey, J.E. *Physical Review Letters*. **1994**, *72(2)*, 258.
- (30) Williams, E. D.; Bartelt, N. C., *Handbook of Surface Science*; Vol 1; Chap. 2.
- (31) Williams, E. D.; Bartelt, N.C. *Science* **1991**, *251*, 393.
- (32) Song, K.-J.; Dong, C.-Z.; Madey, T. E. *Langmuir* **1991**, *7*, 3019.
- (33) Dong, C.-Z.; Zhang, L.; Diebold, U.; Madey, T. E. *Surface Science*. **1995**, *322*, 221.
- (34) Dong, C. Z.; Shivaprasad, S. M.; Song, K.-J.; Madey, T. E. *Journal of Chemical Phys.* **1993**, *99*, 9172.
- (35) Madey, T. E.; Guan, J.; Nien, C.-H.; Dong, C.-Z.; Tao, H.-S.; Campbell, R.A. *Surface Review Letters*. **1996**, *3*, 1315 (and references therein).
- (36) Song, K.-J.; Lin, J. C.; Lai, M. Y.; Wang, Y. L. *Surface Science*. **1995**, *327*, 17.

- (37) Herring, C. *Physical Review* **1951**, *82*, 87.
- (38) Chen, S.P. *Surface Science*. **1992**, *274*, L619.
- (39) Rousset, S.; Gauthier, S.; Siboulet, O.; Sacks, W.; Belin, M.; Klein, *Physical Review Letters*. **1989**, *63*, 1265.

CHAPTER 5

UHV-STM, LEED AND AES STUDIES: CrN OVERLAYER ON $\text{Fe}_{0.8}\text{Cr}_{0.2}(100)$

Introduction

This section deals with studies on the effects of N segregation on the composition, topography and oxidation of a $\text{Fe}_{0.8}\text{Cr}_{0.2}(100)$ surface. This work is part of the efforts to understand in detail the effects of impurity segregation on surface properties, particularly with respect to oxidation and adhesion of oxides to Fe and alloy substrates. Annealing of a $\text{Fe}_{0.8}\text{Cr}_{0.2}(100)$ crystal to elevated temperatures (~ 833 K) induces the co-segregation of Cr and N (impurity from the bulk) leading to the formation of a CrN surface phase overlayer on the $\text{Fe}_{0.8}\text{Cr}_{0.2}(100)$ substrate. Results of STM, LEED and Auger data are presented for a CrN-enriched surface as well as for a N-depleted $\text{Fe}_{0.8}\text{Cr}_{0.2}(100)$ surface (*vide infra*).

Experimental

The experiments were carried out on the UHV system described in the experimental section of Chapter 2. Briefly, it consists of a scanning tunneling microscope (STM), Auger electron spectroscopy (AES), low energy electron diffraction (LEED) and quadrupole mass spectrometer. Sample exposure to O_2 was carried out by backfilling the

chamber at pressures below 10^{-7} Torr, using a manual leak valve to control pressure. Gas exposures are reported here in terms of Langmuir (L) (1 Langmuir = 10^{-6} Torr-sec). Pressures were measured with a nude ion gauge calibrated for dinitrogen. Exposures have not been corrected for ion gauge sensitivity or flux to the sample.

The $\text{Fe}_{0.8}\text{Cr}_{0.2}(100)$ bcc crystal used in the experiments was obtained commercially (1) with a misalignment from the (100) orientation within $\pm 0.5^\circ$. The crystal has a diameter of 9 mm and a thickness of 1 mm. Bulk impurities detected by AES were N, S and C. Cleaning of the sample was accomplished by repeated cycles of a combination of Ar ion bombardment (10^{-6} Torr, 1000 eV, 15 min) and thermal annealing (833 K, 30 min). Auger measurements show that Cr and N segregated to the surface after annealing at 833 K. Neither C nor S segregation was observed at this temperature. Preparation of the N-depleted sample involved repeated cycles of "hot" sputtering - Ar ion bombardment near 833 K (10^{-6} Torr, 1000 eV, 30 min) and thermal annealing (833 K, 10 min). The N-depleted surface contains N coverage significantly less than the CrN surface.

For Auger peak-to-peak measurements, the Fe peak at 651 eV, the Cr peak at 489 eV and the O peak at 503 eV were used. To carry out STM measurements, the sample was transferred to the STM stage after cooling down to room temperature. The STM was operated in a constant current mode. The tip used was made from a polycrystalline W wire (0.01 inch diameter) which was electrochemically etched in KOH solution. Some of the STM measurements were carried out using a mechanically cut Pt tip. No significant difference was observed between images obtained using either a W or Pt tip. Most of the

STM images consisted of 250×250 pixels and were obtained with a tunneling current of 1nA. The gap voltage was varied between 0.1 V - 1 V. Tunneling current vs. gap voltage ($I-V$) measurements were performed, recorded simultaneously with topographical measurements. The tip-sample separation was constant during each spectroscopy measurement. Each step of the voltage ramp was 1/30 of the full voltage range (-1 V to +1 V). Measurement of spectroscopy curves were taken in the grid mode (5×5) corresponding to 50×50 pixels out of a 250×250 pixels topographic image.

Results

Clean CrN

The clean CrN overlayer was prepared by annealing the sputtered $\text{Fe}_{0.8}\text{Cr}_{0.2}(100)$ crystal to 833 K at varying annealing periods between 1 to 30 min. Fig. 5.1 displays the Auger spectrum showing the co-segregation of Cr and N to the surface upon annealing of the crystal. Fig. 5.2 shows the relative Auger peak-to-peak intensity of Cr and N to Fe as a function of annealing time at 833 K in UHV. The data indicate that N and Cr saturation coverages are achieved very quickly (< 5 min.). This is in contrast to previous results (2) on the co-segregation of Cr and N on a $\text{Fe}_{70.4}\text{Cr}_{17}\text{Ni}_{12.6}(100)$ substrate. The ternary alloy surface saturated with Cr and N after annealing for approximately one hour at 900 K (2). In the present study, it took 5 minutes for the $\text{Fe}_{0.8}\text{Cr}_{0.2}(100)$ surface to saturate. The large difference in the time period for saturation of CrN layer may be due to the presence of Ni in the ternary alloy. Whether this difference is due to Ni or to differences in bulk N concentration requires further investigation.

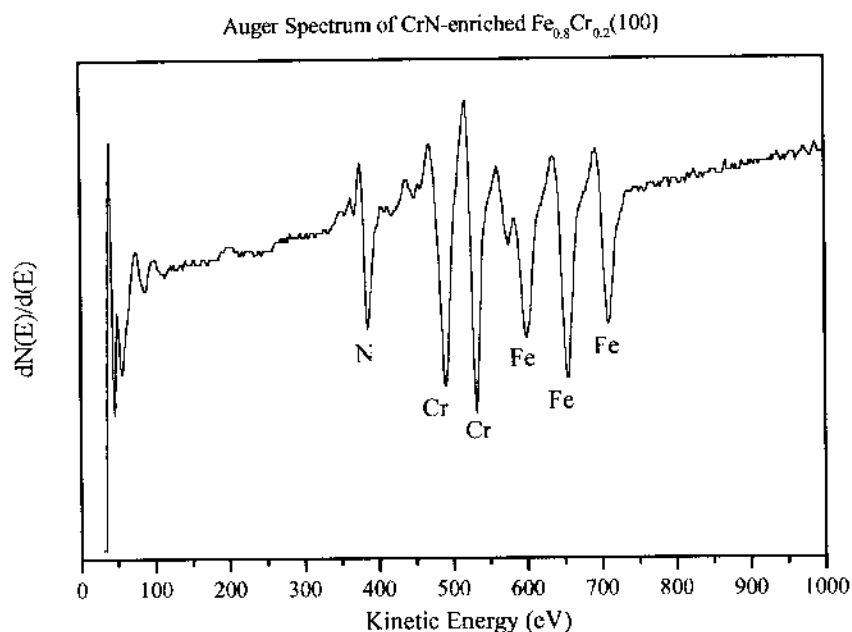


Figure 5.1. Auger spectrum of the $\text{Fe}_{0.8}\text{Cr}_{0.2}(100)$ crystal after a 30-minute anneal at 833 K in UHV. The spectrum shows a surface enriched with cosegregated Cr and N.

LEED measurements of the CrN-enriched $\text{Fe}_{0.8}\text{Cr}_{0.2}(100)$ surface revealed a sharp (1×1) pattern with low background. From the LEED geometry the surface unit mesh of the CrN layer was calculated to be $2.9 \pm 0.1 \text{ \AA}$, coincident with $\text{Fe}_{0.8}\text{Cr}_{0.2}(100)$ substrate indicating that the CrN overlayer is formed epitaxially on the $\text{Fe}_{0.8}\text{Cr}_{0.2}(100)$ substrate. This is consistent with results of a previous investigation (3) which proposed a model for the CrN phase grown on the $\text{Fe}_{0.8}\text{Cr}_{0.2}(100)$ substrate. The model consists of two epitaxed layers of Cr atoms and a N overlayer with N occupying the 4-fold hollow sites at the Cr(100) surface (3). LEED measurements on certain areas of the sample reveal some LEED spot-splitting doublets at a beam energy of 45 eV. The lattice constants of the CrN

overlayer and the $\text{Fe}_{0.8}\text{Cr}_{0.2}(100)$ are identical and can therefore be ruled out as the cause of the spot-splitting. The spot-splitting indicates the presence of steps on the surface.

Fig. 5.3 shows a representative STM image along with a line profile of the CrN surface grown on the $\text{Fe}_{0.8}\text{Cr}_{0.2}(100)$ surface. The CrN overlayer was produced by annealing the crystal at 833 K for 30 min. Although saturation can be achieved at shorter annealing times (Fig. 5.2), the annealing time of 30 min was necessary to effect a flat surface desirable for STM measurements. As shown in Fig. 5.3, the surface is largely

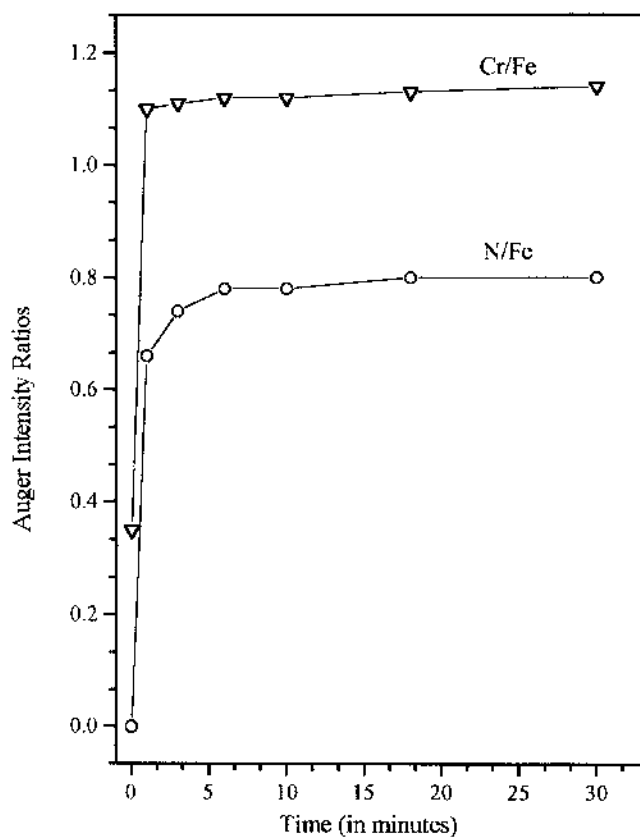


Figure 5.2. Variations in the $\text{Cr}_{(489)}/\text{Fe}_{(651)}$ and $\text{N}_{(379)}/\text{Fe}_{(651)}$ Auger peak-to-peak intensity ratios of the $\text{Fe}_{0.8}\text{Cr}_{0.2}(100)$ sample as a function of annealing time at 833 K in UHV. The data show that saturation coverages for Cr and N were achieved very quickly.

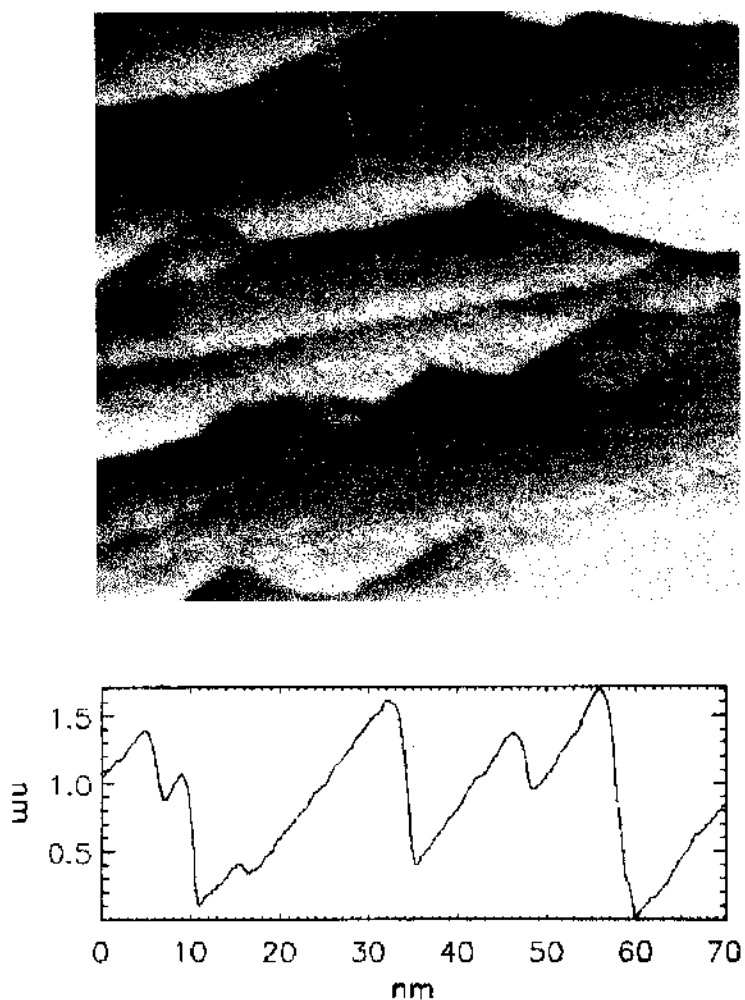


Figure 5.3. STM topographic data (50 nm \times 50 nm) and line profile of the clean CrN surface.

inhomogeneous consisting of wide terraces of varying widths. The terrace widths range from 5 to 65 nm and the step heights range from 0.2 to 3.5 nm. The steps are preferentially oriented in the $\langle 100 \rangle$ direction. Double steps and kinks were also observed. The step-terrace topography revealed is consistent with the observation of LEED spot-splitting on certain areas of the sample surface. A typical I - V curve of the CrN overlayer (between -1 V to +1 V) demonstrates an ohmic behavior (linear), consistent with band structure calculations (4).

Oxidized CrN

The oxidation of the CrN-enriched $\text{Fe}_{0.8}\text{Cr}_{0.2}(100)$ sample was carried out at room temperature. Fig. 5.4 shows variations in the low energy Auger spectra of the CrN-enriched $\text{Fe}_{0.8}\text{Cr}_{0.2}(100)$ as a function of O_2 exposure. For the clean CrN spectra (top trace, Fig. 5.4), the Cr(MVV) transition is observed at 36 eV while the Fe(MVV) transition is observed at 47 eV. Previous studies (3, 5) on CrN surfaces have reported the observation of a shoulder for the Cr(MVV) transition at 32 eV which has been assigned to an inter-atomic transition between Cr and N. The absence of such a feature in the Cr(MVV) Auger peak may be due to a poorer energy resolution in the computer-controlled CMA used in the present study. The rest of the data displayed in Fig. 5.4 show a shift in the Cr(MVV) transition to lower energy (36 to 31 eV) indicating the oxidation of Cr. In contrast, no shift in the peak energy or a change in peak shape was observed for Fe (47 eV).

The changes in the relative intensities of N, Cr and O Auger signals vs. O_2 exposures are presented in Fig. 5.5. The N to O Auger peak-to-peak ratio decreased as the O_2 exposure was increased to 10 L (Fig. 5.5b). This is accompanied by a corresponding decrease in the N to Cr ratio (Fig. 5.5a). There are two chemical events which are consistent with the decrease of the N Auger signal upon oxidation of the CrN surface. One is the migration of Cr atoms across the N layer to the surface and formation of chromium oxide over the surface N atoms resulting in the attenuation of N signal. A second possibility is a reaction between CrN and oxygen to form chromium oxide and

molecular N_2 , NO or N_2O which desorbs from the surface. The exchange reaction to form molecular N_2 involving CrN and oxygen has been suggested by a previous study (6). However, in that study the oxidation of the CrN surface was carried out at elevated temperatures.

LEED experiments revealed a gradual change from a sharp (1×1) to a more diffused pattern with increasing O_2 exposure. After 5 L O_2 exposure only very weak LEED spots were observed. No LEED spots were detectable after 10 L O_2 exposure.

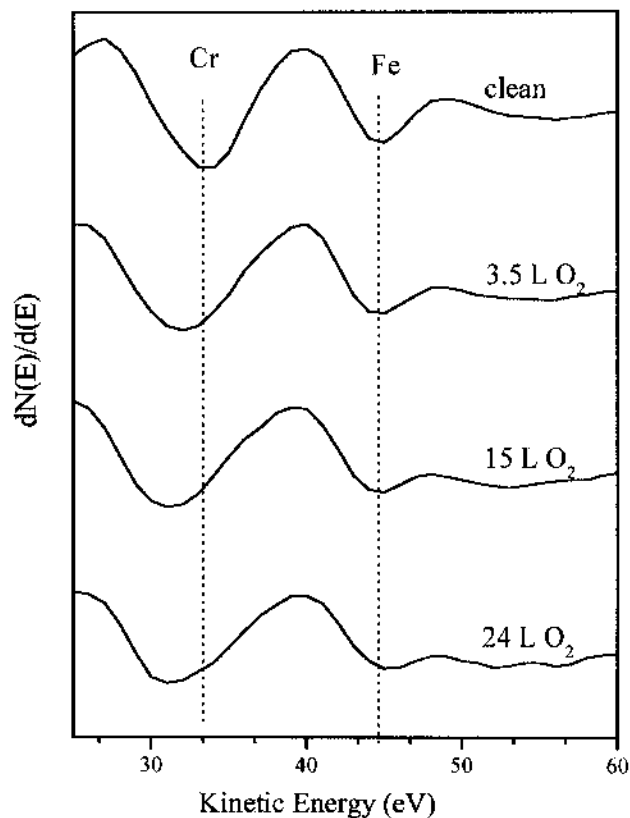


Figure 5.4 Variations in the low-energy Auger spectra of Fe and Cr for the CrN enriched- $Fe_{0.8}Cr_{0.2}(100)$ surface as a function of O_2 exposures at room temperature. The data indicate that at saturation oxygen coverage (15 L O_2), Cr is oxidized while Fe remains metallic.

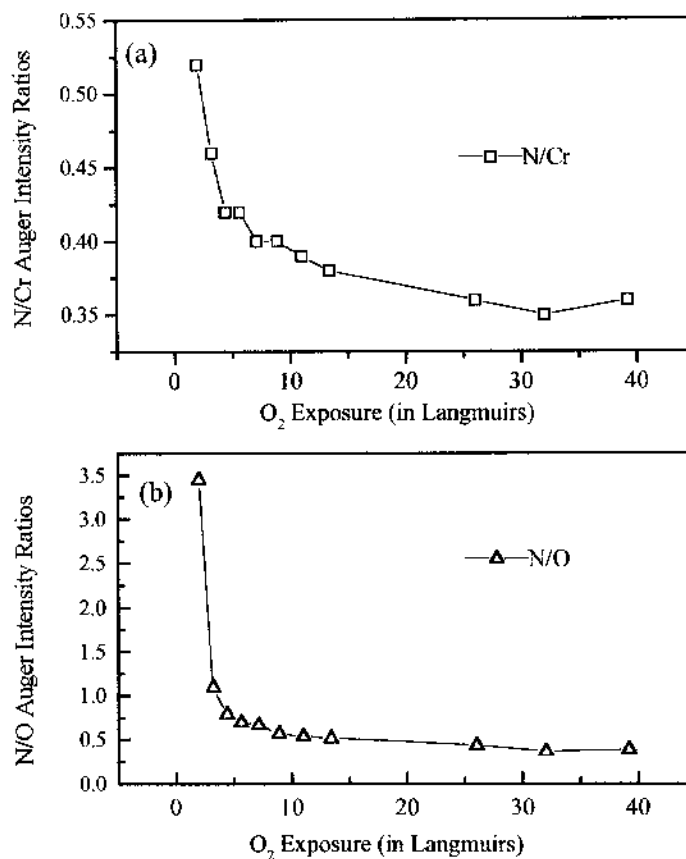


Figure 5.5 Changes in the Auger peak-to-peak intensity ratios of the CrN surface as a function of O₂ exposure: (a) N₍₃₇₉₎/Cr₍₄₈₉₎ and (b) N₍₃₇₉₎/O₍₅₀₃₎.

However, annealing the oxidized sample for a few seconds to 800 K resulted in the reappearance of a weak (1 × 1) diffraction pattern. Similar phenomena have been observed with O₂ adsorption on Cr(100) surface at room temperature (7). In addition to the reappearance of the (1 × 1) pattern, the Auger O/Cr ratio was observed to decrease upon annealing. It is not clear whether the loss of O is due to desorption of oxygen from the surface or diffusion of oxygen into the bulk.

The STM results showed no apparent changes in the topography at low O₂ exposures (< 0.5 L) in comparison to the clean CrN. However, after 15 L of O₂ exposure (saturation coverage) at 300 K, changes in the surface topography became discernible. Fig. 5.6 shows the STM images of the oxidized CrN surface. As can be seen from the image, there is an apparent roughening of the terrace surfaces. This roughness is due to the nucleation and growth of oxide islands on the surface. The diameter of these islands range from 1 to 3 nm. The distribution of the oxide on the surface are inhomogeneous. Variations in topography across the sample surface were observed (Fig. 5.6). This observation is corroborated by the varying *I-V* behavior obtained on different areas of the sample surface exposed to the same O₂ dose. As presented in Fig. 5.6, there are 3 different types of topographical features observed: (a) relatively small and evenly spaced terraces (~5 nm width, 0.2 - 0.3 nm height) with straight step edges, small two-dimensional "islands" visible. (b) large terraces (13 - 65 nm width, 0.6 - 3.5 nm height) with irregular step edges, also with small two-dimensional "islands" on the terraces (c) large three-dimensional islands, observed upon heavier O₂ dosing (for exposures = 18L). These large islands were observed only on certain areas of the sample. Previous studies of O₂ adsorption on transition metals (8, 9) revealed oxide island formation at room temperature at sub-monolayer coverages. The results presented here suggest that this process is also true for oxygen adsorption on the CrN surface.

Fig. 5.7 presents the variations in the *I-V* curve as a function of O₂ exposure. Each *I-V* curve displayed in Fig. 5.7 represents an average over an area as indicated in the

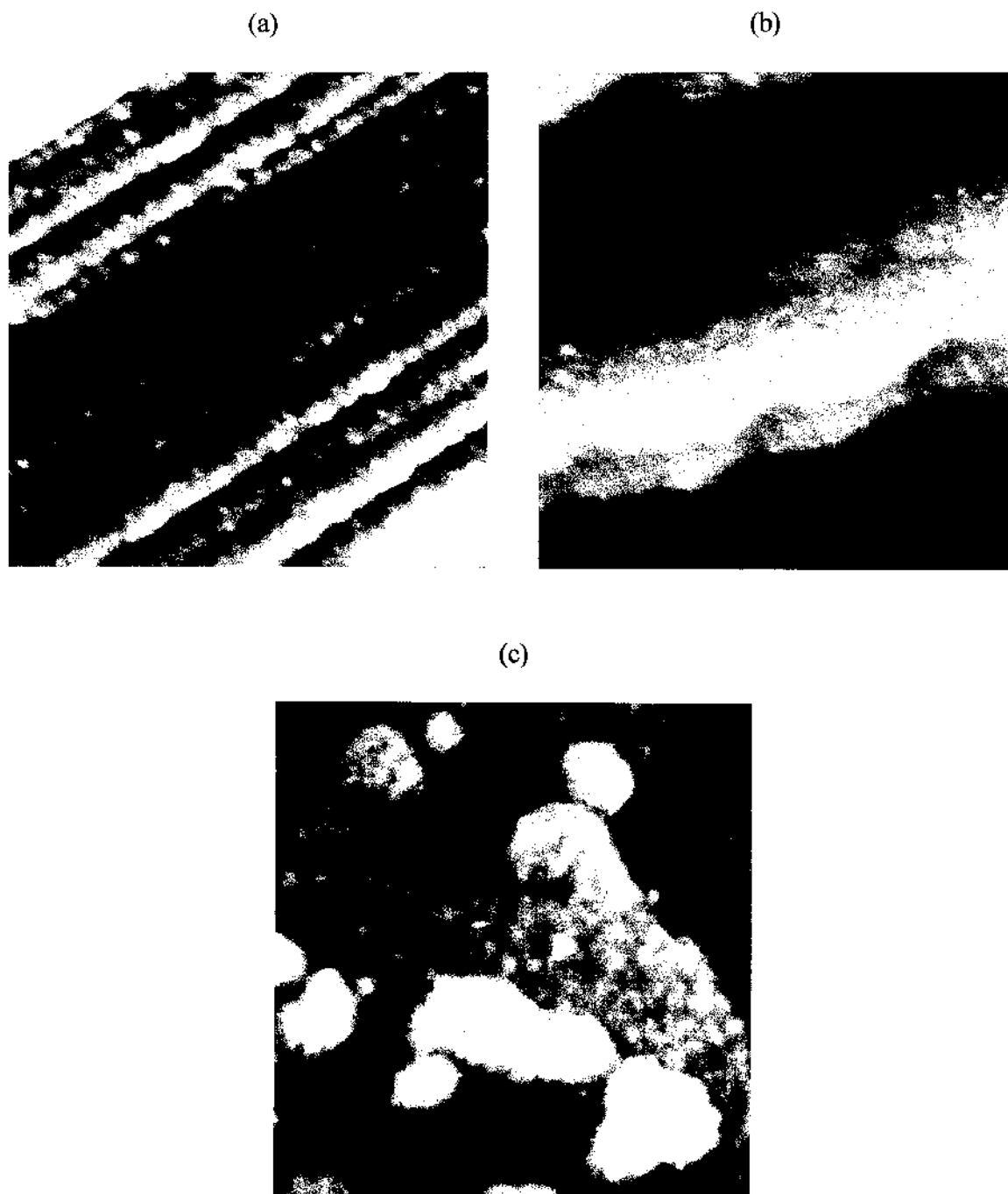


Figure 5.6. Variations in the topography across the CrN surface after exposure to 18 L of O_2 . Three types of topographical features were observed: (a) small terraces with 2-dimensional “islands” (b) large terraces with 2-dimensional “islands” (c) 3-dimensional islands. All images are taken from 100nm x 100 nm scan areas.

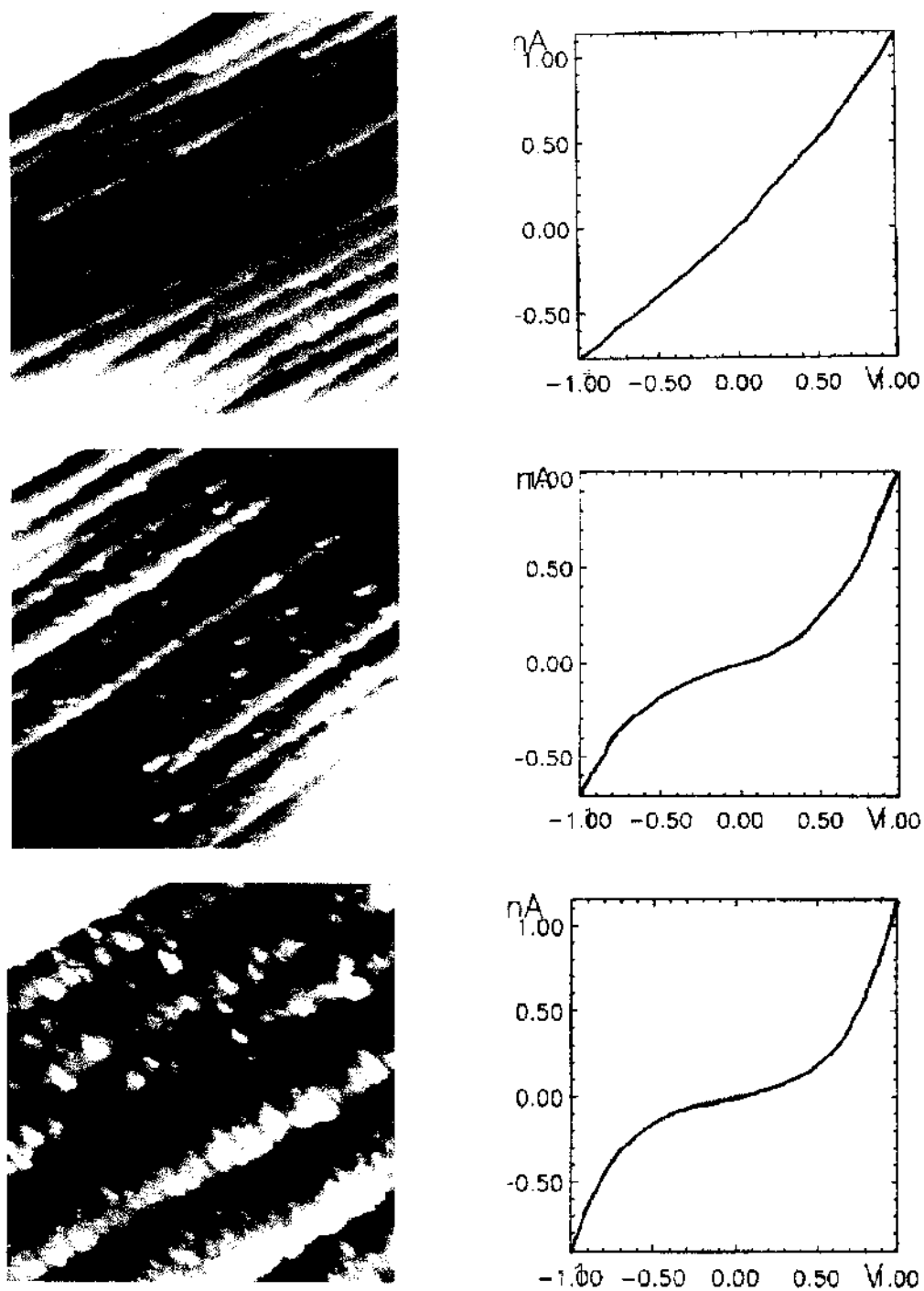


Figure 5.7. Changes in the characteristics of I - V curves as a function of O_2 exposure for the CrN surface. Also shown adjacent to the curves are the corresponding STM images which indicate the surface area where the I - V measurements were taken.

adjacent STM image. As shown in the figure, the I - V curve changes from metallic to insulating behavior as the oxygen coverage is increased. This indicates a change in the surface electronic density of states during the oxidation process. At saturation coverage, all the different topographical features (i.e., roughened surfaces, islands) exhibited similar I - V curves. This indicates that at saturation oxygen coverage, both islands and planar areas were sufficiently oxidized to display insulating behavior. The changes in the I - V curves observed at different O_2 exposures correlate well with the variations in the AES low energy peaks shown previously (Fig. 5.4).

N-depleted $Fe_{0.8}Cr_{0.2}(100)$

To investigate the effect of N on the oxidation of $Fe_{0.8}Cr_{0.2}(100)$, AES experiments were carried out on a $Fe_{0.8}Cr_{0.2}(100)$ crystal with a significantly less N segregation on the surface. This sample was prepared by repeated cycles of ion sputtering and annealing in UHV at 833 K until the bulk is almost depleted of N. Fig. 5.8 displays the Auger spectrum of the N-depleted $Fe_{0.8}Cr_{0.2}(100)$ sample after annealing at 833 K in UHV for 30 min. The spectrum indicates a smaller N segregation on the surface as compared to the CrN overlayer (Fig. 5.1). It is also evident from Fig. 5.8 that the Cr segregation has decreased considerably. This result is consistent with a previous study (2) which has shown that Cr segregation on an alloy surface occurs only upon its co-segregation with impurities such as N and S.

The oxidation of the sample was performed in a similar manner as the oxidation of the CrN overlayer. The O_2 partial pressure was limited to 10^{-8} Torr. Fig. 5.9 displays the

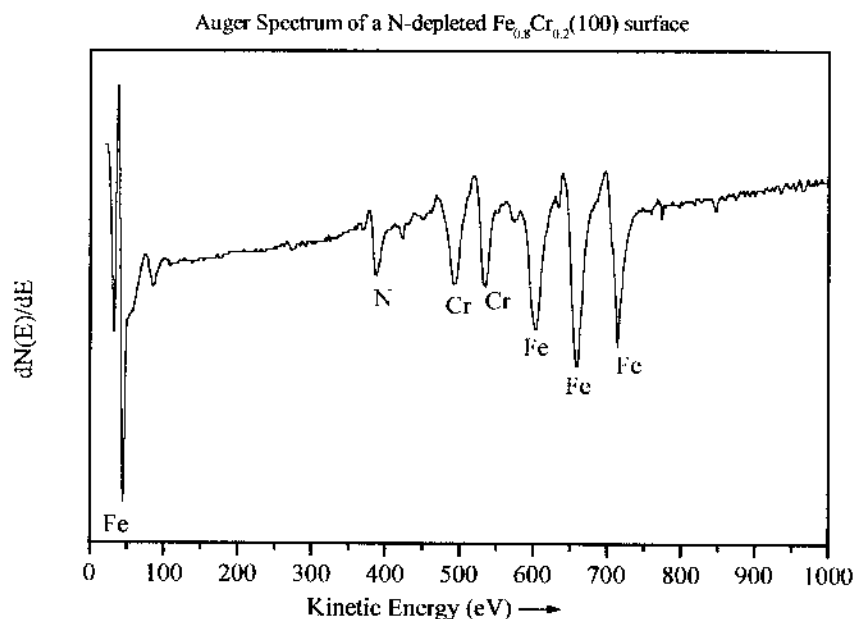


Figure 5.8. Auger spectrum of the N-depleted $\text{Fe}_{0.8}\text{Cr}_{0.2}(100)$ surface. The sample was annealed at 833 K for 30 min. Relatively smaller amounts of N and Cr are segregated to the surface.

variations in the Auger intensity ratios as a function of O_2 exposure on the N-depleted $\text{Fe}_{0.8}\text{Cr}_{0.2}(100)$. The data showed that initially, only Cr is oxidized, evident from the 36 eV peak shift to lower energy. At higher O_2 exposures, a bifurcated Fe peak at 46 eV is also apparent indicating the formation of both Fe and Cr oxides. A similar Fe(MVV) bifurcated peak has been observed in previous studies (5), indicative of the presence of oxidized Fe. The diminished Fe signal (bottom trace, Fig. 5.9) and the observation of an increase in the Cr to Fe ratio (not shown) indicate preferential oxidation and surface segregation of Cr. This oxidation behavior is generally true for stainless steels (10).

LEED measurements of the clean N-depleted $\text{Fe}_{0.8}\text{Cr}_{0.2}(100)$ surface show a sharp

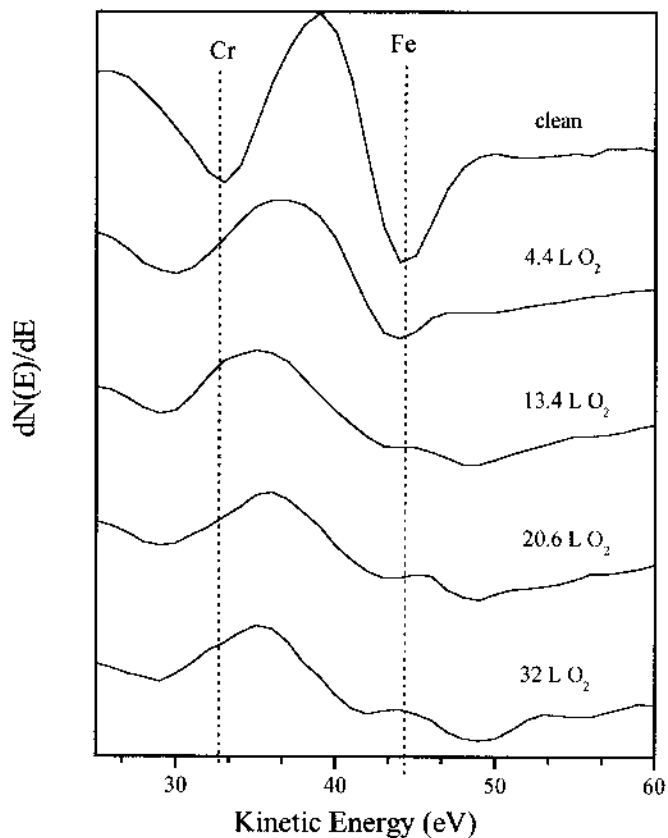


Figure 5.9. Variations in the Auger spectra of the N-depleted $\text{Fe}_{0.8}\text{Cr}_{0.2}(100)$ surface as a function of O_2 exposure. The spectra show that both Fe and Cr are oxidized upon exposure to O_2 .

(1×1) pattern. LEED doublets are still observed perpendicular to the step orientation.

Corresponding STM experiments on the clean N-depleted $\text{Fe}_{0.8}\text{Cr}_{0.2}(100)$ surface show a step distribution that is more homogeneous than what was observed for the CrN surface.

Upon adsorption of O_2 on the N-depleted $\text{Fe}_{0.8}\text{Cr}_{0.2}(100)$ surface, the LEED (1×1) pattern became diffuse. The STM data reveal that oxide islands are formed before oxygen saturation coverage was reached.

Discussion

Previous studies (11) of CrN overlayers thermally grown on Fe-15%Cr-N(100) surfaces revealed that either a CrN surface compound or a CrN three-dimensional surface precipitate may be formed depending on the bulk N concentration as well as on the N solubility limit at the annealing temperature. It was shown (11) that a CrN surface compound was formed at an annealing temperature near 950 K while a CrN surface precipitate was formed at a lower temperature as a result of N exceeding its solubility limit in the Fe-15%Cr-N alloy. The Auger data for the three-dimensional CrN precipitate shows that the Fe Auger signal is severely attenuated as a result of the formation of several layers of CrN precipitate (11). This result is significantly different from the Auger spectrum for the CrN overlayer (Fig. 5.1) in the present study which indicates that a considerable amount of Fe is still present within the sampling depth of the Auger analyzer. From the previous work (11), it was further shown that for the CrN compound formed near 950 K, an equilibrium surface state was achieved, evident from the constant relative surface concentrations of N, Cr and Fe as a function of time. This is consistent with the data presented in Fig. 5.2 which suggests that an equilibrium surface state was also achieved for the system studied here. It is therefore concluded that the CrN overlayer studied is a CrN surface compound and not a CrN surface precipitate.

The STM measurements showed that the CrN overlayer is rough and inhomogeneous, exhibiting many deviations from ideal regularity. The step-terrace topography (Fig. 5.3) is consistent with the observation of LEED spot-splitting on certain

areas of the sample surface. These results indicate a non-uniform step distribution which is not due to a simple miscut of the sample.

Oxidation of the surface results in disordering of the CrN layer (1×1) LEED pattern. STM measurements revealed oxide island formation at saturation coverage. Certain experimental problems were encountered while performing STM measurements on the oxidized CrN surface. After exposure to O_2 , the noise level of the STM image would often increase. In contrast, the noise level for a clean CrN surface was usually minimal or absent. A plausible explanation for this is contamination of the tip with oxygen during scanning on the oxidized surface. To remedy this problem, scanning using a high tunneling current (15 - 30 nA) was employed. In addition, a "shadowing effect" in the oxidation of the CrN surface was observed: if the tip is placed at the tunneling position (with or without scanning) during oxidation, there is little or no oxygen adsorbed on the vicinity surrounding the tip (250 nm x 250 nm). This is evident from the linear behavior (ohmic) of the $I-V$ data of the surrounding area where the tip was located. Moreover, no changes in topography of the CrN in the vicinity near the tip were detected, corroborating the ohmic behavior of the surface. Upon transfer of the tip to another area, the $I-V$ curve showed insulating behavior indicating the adsorption of oxygen on the surface. The cause of this phenomenon is not understood.

In the results section, it was shown that for the CrN surface, exposure to O_2 oxidizes Cr while the underlying Fe remains metallic. In contrast, O_2 exposure of the N-depleted surface results in the oxidation of both Cr and Fe. A comparison of the O_2

uptake curves between the N-depleted $\text{Fe}_{0.8}\text{Cr}_{0.2}(100)$ surface and the CrN surface is presented in Fig. 5.10. Changes in the absolute O(KLL) Auger peak-to-peak intensities as a function of O_2 exposure are presented. It is clear from the curves that the O saturation coverage is significantly higher for the N-depleted surface. A similar oxidation-retardation effect has been reported for TaN (12). The retardation in the oxidation of the CrN overlayer as compared to the N-depleted $\text{Fe}_{0.8}\text{Cr}_{0.2}(100)$ surface suggests that N is not removed from the CrN surface during oxidation. Removal of N during oxidation of the CrN-enriched surface would have resulted in a saturation coverage close to or approaching that of the oxygen saturation coverage for the N-depleted surface. The data presented in Fig. 5.10 shows that such is not the case. While the possibility of a reaction between CrN and oxygen to form Cr-oxide and N_2 , NO or N_2O cannot be completely ruled out, the data presented in Fig. 5.10 shows that there is a significant difference in the saturation oxygen coverage between the CrN-enriched surface and the N-depleted surface. It is therefore likely that the attenuation of the N Auger signal is due to the formation of chromium oxide on top of a buried N layer. A 60% decrease was observed in the N(KLL) Auger intensity at saturation oxygen coverage (15 L O_2) of the CrN-enriched surface. Assuming a N layer buried by an average thickness d of chromium oxide overlayer, a rough estimate (10) of d gives 2.55 Å, which is approximately one monolayer of chromium oxide. This result is consistent with previous studies on the adsorption of oxygen on Cr(100) (7) and Fe(100) (8) at similar exposure range at room temperature.

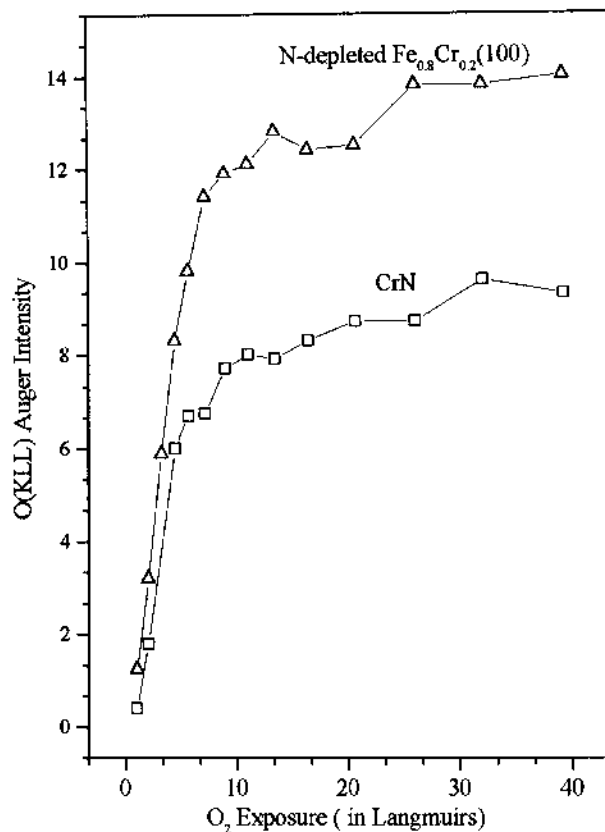


Figure 5.10. Changes in the absolute O(KLL) Auger peak-to-peak intensity as a function of O₂ exposure for CrN-enriched and N-depleted Fe_{0.8}Cr_{0.2}(100) surfaces.

Summary and Conclusions

The Fe_{0.8}Cr_{0.2}(100), with and without co-segregation of Cr and N, and its oxidation behavior was investigated by STM, AES and LEED. The results are summarized as follows:

STM: The clean CrN overlayer has a step-terrace topography which cannot be attributed to the miscut of the Fe_{0.8}Cr_{0.2}(100) surface. *I-V* measurements show that the CrN surface exhibits metallic behavior with band structure calculations (4). After

adsorption of a saturation coverage for oxygen (15 L O_2) on the CrN surface, oxide island formation was observed. The I - V curve of the oxidized CrN overlayer shows insulating behavior. The variations in the I - V curves during oxidation correlate well with the different stages of oxidation.

LEED: The clean CrN surface shows a sharp (1×1) pattern with very low background. Upon exposure to O_2 vapor, the (1×1) diffraction pattern gradually becomes diffuse and eventually disappears. A short heating treatment results in the reappearance of (1×1) pattern with some background.

AES: Adsorption of oxygen on the CrN-enriched $\text{Fe}_{0.8}\text{Cr}_{0.2}(100)$ surface results in the attenuation of the N Auger signal. The Auger data suggest that a chromium oxide forms on top of a buried N layer as oxygen saturation coverage decreases with increasing initial N content. However, the possibility of desorption of N_2 , N_2O or NO cannot be completely ruled out. The underlying Fe of the CrN-enriched surface is not oxidized during exposure to oxygen. In the N-depleted $\text{Fe}_{0.8}\text{Cr}_{0.2}(100)$, adsorption of oxygen results in the oxidation of both Cr and Fe. The saturation coverage for O_2 on the N-depleted surface is 50% higher than the CrN-enriched surface. The presence of N retards oxidation of the surface, in agreement with results reported for TaN (12). In that case, oxidation results in oxynitride formation, while in the case of $\text{Fe}_{0.8}\text{Cr}_{0.2}(100)$, Cr oxide layer overgrows the surface N atoms.

Chapter References

- (1) Aremco Products Inc., P.O. Box 429, 23 Snowden Ave., Ossining, NY 10562.

- (2) Elbiache, A.; Marcus, P. *Applied Surface Science*. **1990**, *45*, 49.
- (3) Uebing, C.; Scheuch, V.; Kiskinova, M.; Bonzel, H. P. *Surface Science*. **1994**, *321*, 89.
- (4) Papaconstantopoulos, D. A.; Pickett, W. E.; Klein, B. M.; Boyer, L. L. *Physical Review B* **1985**, *31*, 52.
- (5) Uebing, C., *Surface Science*. **1990**, *225*, 97.
- (6) Dennert, R.; Grabke, H. J.; Viefhaus, H. *Fresenius Journal of Analytical Chemistry* **1995**, *353*, 678.
- (7) Ekelund, S.; Leygraf, C. *Surface Science*. **1973**, *40*, 179.
- (8) Simmons, G. W.; Dwyer, D. J. *Surface Science*. **1975**, *48*, 373.
- (9) Liu, J. ; Lu, J. P.; Chu, P. W.; Blakely, J. M. *Journal of Vacuum and Science Technology. A* **1992**, *10(4)* 2355.
- (10) Briggs, D.; Seah, M. P., in *Practical Surface Analysis by Auger and X-ray Photoelectron Spectroscopy*, edited by D. Briggs and M. P. Seah; Wiley & Sons, New York, 1983; p.323.
- (11) Uebing, C.; Viefhaus, H.; Grabke, H. J. *Applied Surface Science* **1988**, *32*, 363.
- (12) Arranz, A.; Palacio, C. *Vacuum* **1994**, *40(10/11)*, 1091

REFERENCE LIST

- Arabczyk, W.; Baumann, T.; Mussig, H.-J.; Storbeck, F. *Vacuum* **1990**, *41*, 79.
- Arabczyk, W.; Mussig, H. J.; Storbeck, F. *Physica Status Solidi. (a)* **1979**, *55*, 437.
- Arabczyk, W.; Narkiewicz, U.; Kalucki, K.; Freidenberg, E. *Applied Surface Science*. **1993**, *72*, 45.
- Arranz, A.; Palacio, C. *Vacuum* **1994**, *40(10/11)*, 1091
- Backer, R.; Horz, G. *Vacuum* **1995**, *46*, 1101.
- Baxter, D. J.; Natesan, K. *Oxidation of Metals* **1989**, *31(3/4)*, 305.
- Briant, C. L. *MRS Bulletin*, October **1990**, 26.
- Briggs, D.; Seah, M. P., in *Practical Surface Analysis by Auger and X-ray Photoelectron Spectroscopy*, edited by D. Briggs and M. P. Seah; Wiley & Sons, New York, 1983; Chap. 6.
- Chase, M. W., et al., *JANAF Thermochemical Tables*; American Chemical Society, Washington DC, 1986.
- Chen, S. P. *Surface Science*. **1992**, *274*, L619.
- Cherri, A. K.; Karim, M. A. *Applied Optics* **1989**, *28*, 4644.
- Colson, J. C.; Larpin, J. P. *MRS Bulletin*. October **1994**, 23.
- Dennert, R.; Grabke, H. J.; Viehhaus, H. *Fresenius Journal of Analytical Chemistry* **1995**, *353*, 678.
- Dong, C.-Z.; Zhang, L.; Diebold, U.; Madey, T. E. *Surface Science*. **1995**, *322*, 221.
- Dong, C. Z.; Shivaprasad, S. M.; Song, K.-J.; Madey, T. E. *Journal of Chemical Physics*. **1993**, *99*, 9172.
- Dunpy, J. C.; Knight, C.; Sautet, P.; Ogletree, D. F.; Somorjai, G. A.; Salmeron, M. B.

- Surface Science*. **1993**, 280, 313.
- Ekelund, S.; Leygraf, C. *Surface Science*. **1973**, 40, 179.
- Elbiache, A.; Marcus, P. *Applied Surface Science*. **1990**, 45, 49.
- Ertl, G.; Koppers, J. *Low Energy Electrons and Surface Chemistry*. VCH Publishers, New York (1985).
- Feldman, L. C.; Mayer, J. W. *Fundamentals of Surface and Thin Film Analysis*; PTR Prentice Hall, Inc., New Jersey, 1986. Chap. 7.
- Feldman, L.C.; Mayer, J.W. *Fundamentals of Surface and Thin Film Analysis*; PTR Prentice Hall, New Jersey, 1986; p. 127.
- Forbes, J. G.; Gellman, A. J.; Dunphy, J. C.; Salmeron, M. *Surface Science*. **1992**, 279, 68.
- Forest, C.; Davidson, J. H. *Oxidation of Metals*. **1995**, 43(5/6), 479.
- Fox, P.; Lees, D. G.; Lorimer, G. W. *Oxidation of Metals*. **1991**, 36(5/6), 491.
- Gardin, D. E.; Batteas, J. D.; Van Hove, M. A.; Somorjai, G. A. *Surface Science*. **1993**, 296, 25.
- Gesmundo, F.; Young, D. J.; Roy, S. K. *High Temperature Material Processes*. **1989**, 8(3), 149.
- Grabke, H. J.; Wiemer, D.; Viehhaus, H. *Applied Surface Science*. **1991**, 47, 243.
- Grossmann, A.; Erley, W.; Ibach, H. *Surface Science*. **1995**, 337, 183.
- Guan, J.; Campbell, R. A.; Madey, T. E. *Surface Science*. **1995**, 341, 311.
- Hardegree, E. L.; Ho, P.; White, J. M. *Surface Science*. **1986**, 165, 488.
- Hedge, R.I.; White, J.M. *Journal of Physical Chemistry*. **1986**, 90, 296.
- Held, G. A.; Goodstein, D. M.; Feenstra, R. M. *Physical Review B* **1993**, 48(11), 8458.
- Herring, C. *Physical Review* **1951**, 82, 87.
- Holloway, P. H.; Hudson, J. B. *Surface Science*. **1972**, 33, 56.

- Hong, S. Y.; Anderson, A. B., *Physical Review B*. **1988**, *38(14)*, 9417.
- Hung, W.-H.; Schwartz, J.; Bernasek, S.L. *Surface Science*. **1993**, *294*, 21.
- Huntley, D. R. *Surface Science*. **1990**, *240*, 13.
- Jones, D. A. *Principles and Prevention of Corrosion*; Macmillan Publishing Company, New York, New York, 1992; Chap. 12. and references therein.
- Kiskinova, M. *Chemical Reviews*. **1996**, *96*, 1431.
- Koestner, R. J.; Salmeron, M.; Kollin, E. B.; Gland, J. L. *Surface Science*. **1986**, *172*, 668.
- Legg, K. O.; Jona, J.; Jepsen, D. W.; Marcus, P. M. *Surface Science*. **1977**, *66*, 25.
- Leygraf, C.; Hultquist, G.; Ekelund, S. *Surface Science*. **1974**, *46*, 157.
- Li, L. C.; Gesmundo, F.; Viani, F.; Toledo, G. P. *High Temperature Material Processes*. **1993**, *12(4)*, 199.
- Liu, J. ; Lu, J. P.; Chu, P. W.; Blakely, J. M. *Journal of Vacuum and Science Technology. A* **1992**, *10(4)* 2355.
- Lobnig, R. E.; Grabke, H. J. *Corrosion Science*. **1990**, *30(10)*, 1045.
- MacLaren, J. M.; Pendry, J. B.; Rous, P. J.; Saldin, D. K.; Somorjai, G. A.; Van Hove, M.A.; Vvedensky, D. D. *Surface Crystallographic Information Service*; D. Reidel Publishing Company, Holland, 1988; p.86.
- Madey, T. E.; Guan, J.; Nien, C.-H.; Dong, C.-Z.; Tao, H.-S.; Campbell, R.A. *Surface Review Letters*. **1996**, *3*, 1315 (and references therein).
- Meier, G. H. *Material Science Engineering*. **1989**, *A120*, 1.
- Muller, O. G.; Katzel, W.; Storbeck, F. *Physica Status Solidi*. **1985**, *89*, 89.
- Mullins, D. R.; Huntley, D. R.; Overbury, S. H. *Surface Science*. **1995**, *323*, L287.
- Murray, E.; Kelber, J.A. *Journal of Vacuum Science and Technology. A* **1995**, *13(5)*, 2558.
- Murray, E.; Prasad, J.; Cabibil, H.; Kelber, J. A. *Surface Science*. **1994**, *319*, 1.

NIST XPS Database.

Ohtani, H.; Kao, C.-T.; Van Hove, M. A.; G. A. Somorjai. *Progress in Surface Science*. **1986**, *23(2/3)*, 155.

Omicron SPM Software 2.0:

Oudar, J. *Material Science Engineering*. **1980**, *42*, 101.

Ozcomert, J.S.; Pai, W.W.; Bartelt, N.C.; Reutt-Robey, J.E. *Physical Review Letters*. **1994**, *72(2)*, 258.

Palacio, C.; Mathieu, J. J.; Stambouli, V.; Landolt, D. *Surface Science*. **1993**, *295*, 251.

Papaconstantopoulos, D. A.; Pickett, W. E.; Klein, B. M.; Boyer, L. L. *Physical Review B* **1985**, *31*, 52.

Perdereau, M.; Oudar, J. *Surface Science*. **1970**, *20*, 80.

Pieraggi, B.; Rapp, R. A. *Journal of Electrochemical Society*. **1993**, *140(10)*, 2844.

Prasad, J.; Murray, E.; Kelber, J. A. *Chemical Physics Letters*. **1992**, *190(3/4)*, 187.

Prasad, J.; Murray, E.; Kelber, J. A. *Surface Science*. **1993**, *289*, 10.

Puerta, J.; Martin, P. *Applied Optics*. **1991**, *20*, 3923.

Redhead, P. A. *Vacuum* **1962**, *12*, 203.

Rousset, S.; Gauthier, S.; Siboulet, O.; Sacks, W.; Belin, M.; Klein, *Physical Review Letters*. **1989**, *63*, 1265.

Ruan, L.; Stensgaard, I.; Besenbacher, F.; Laegsgaard, E. *Physical Review Letters*. **1993**, *71*, 2976.

Schardt, B. C.; Yau, S.-L., Rinaldi, F. *Science* **1989**, *243*, 1050.

Scully, J. C. *The Fundamentals of Corrosion*; Second Edition; Pergamun Press, New York, 1990; Chap. 1..

Seo, M.; Sato, M.; Lumsden, J. B.; Staehle, R. W. *Corrosion Science*. **1977**, *17*, 209.1.

- Shih, H. D.; Jona, F. *Physical Review Letters*. **1981**, *46*, 731.
- Shih, H. D.; Jona, F.; Jepsen, D. W.; Marcus, P. M. *Physical Review Letters*. **1981**, *46*, 731.
- Shih, H. D.; Jona, F.; Jepsen, D. W.; Marcus, P. M. *Surface Science* **1981**, *104*, 39.
- Shores, D. A. *The Electrochemical Society Interface*. Spring **1997**, *6(1)*, 42.
- Simmons, G. W.; Dwyer, D. J. *Surface Science*. **1975**, *48*, 373.
- Smialek, J. M.; Jayne, D. T.; Schaeffer, J. C.; Murphy, W. H. *Thin Solid Films* **1994**, *253*, 285.
- Sokolov, J.; Jona, F.; Marcus, P.M. *Physical Review B*. **1986**, *33*, 1397.
- Somorjai, G. A. *Introduction to Surface Chemistry and Catalysis*. (Wiley, New York, 1994). Chap. 2.
- Song, K.-J.; Dong, C.-Z.; Madey, T. E. *Langmuir* **1991**, *7*, 3019.
- Song, K.-J.; Lin, J. C.; Lai, M. Y.; Wang, Y. L. *Surface Science*. **1995**, *327*, 17.
- Stasik, M. C.; Pattit, F. S.; Meier, G. H. *Scripta Metallurgica et Materiala*. **1994**, *31(12)*, 1645.
- Stott, F. H. *Reports of Progress in Physics*. **1987**, *50*, 861.
- Stringer, J.; Hou, P. Y. *Oxidation of Metals*. **1992**, *38(5/6)*, 323.
- Tersoff, J.; Lang, N. D. in *Scanning Tunneling Microscopy*, Vol. 27. edited by Stroscio, J. A.; J. A.; Kaiser, W. J.; Academic Press, Inc., California, 1993; Chap. 1.
- Thiel, P. A.; Madey, T. E. *Surface Science Reports*. **1987**, *7*, 211.
- Titmus, S.; Wander, A.; King, D. A. *Chemical Reviews*. **1996**, *96*, 1291.
- Uebing, C., *Surface Science*. **1990**, *225*, 97.
- Uebing, C.; Scheuch, V.; Kiskinova, M.; Bonzel, H. P. *Surface Science*. **1994**, *321*, 89.
- Uebing, C.; Viehhaus, H.; Grabke, H. J. *Applied Surface Science* **1988**, *32*, 363.
- Wagner, C. D.; Riggs, W. M.; Davis, L. E.; Moulder, J. F.; Muilenberg, G. E. (eds.)

Handbook of X-ray Photoelectron Spectroscopy; Physical Electronics-Division of Perkin-Elmer Corp., Eden Prairie, MN, 1979.

Wiemer, D.; Grabke, H. J.; Viehhaus, H. *Fresenius Journal of Analytical Chemistry*. **1991**, *341*, 402.

Williams, E. D.; Bartelt, N. C., *Handbook of Surface Science*; Vol 1;Chap. 2.

Williams, E. D.; Bartelt, N.C. *Science* **1991**, *251*, 393.

Windawi, H.; Katzer, J. R. *Journal of Vacuum Science and Technology*. **1979**, *16(2)*, 497.

Woodruff, D. P. *Journal of Physics. Condensed Matter* **1994**, *6*, 6067.